CHARACTERIZATION AND APPLICATION OF ANODIZED ALUMINIUM FOR SELECTIVE SOLAR ABSORBER IN PARABOLIC TROUGH COLLECTOR (PTC)

TITIPORN CHORCHONG

A Thesis Submitted to the Graduate School of Naresuan University
In Partial Fulfillment of the Requirements
for the Doctor of Philosophy Degree in Renewable Energy
December 2015

Thesis entitled "Characterization And Application Of Anodized Aluminium For Selective Solar Absorbers In Parabolic Trough Collectors"

by Ms. Titiporn Chorchong

has been approved by the Graduate School as partial fulfillment of the requirements for the Doctor of Philosophy Degree in Renewable Energy of Naresuan University

Oral Defense Committee

Sirichai Thepa ..... Chair

(Associate Professor Sirichai Thepa, D.Sc.)

Tawat Suriwong ..... Advisor

(Tawat Suriwong, Ph.D.)

S. Sukchai ..... Co – Advisor

(Sukruedee Sukchai, Ph.D.)

..... Co – Advisor

(Thotsaphon Threrujirapapong, Ph.D.)

..... Internal Examiner

(Sakda Somkun, Ph.D.)

Approved

.....

(Panu Putthawong, Ph.D.)

Associate Dean for Administration and Planning

for Dean of the Graduate School

11 DEC 2015

ACKNOWLEDGEMENT

Contributions and support from many people helped me in the completion of this research. I would like to take this opportunity to express my appreciation to them.

First, I would like to express my deeply appreciate and gratitude to my adviser, Dr.Tawat Suriwong, for all the invaluable guidance, and beneficial advice given, even during the busy times and for his kindness throughout my study. I also acknowledge my co-advisers Dr.Sukruedee Sukchai and Dr.Thotsaphon Threrujirapapong whose continuous support and encouragement no doubt contributed to my studies.

My heart-felt thanks go to my dissertation examiners, for their helpful suggestions on gaining approval of my thesis.

I am grateful to School of Renewable Energy, Naresuan University, the National Research Council of Thailand (NRCT), and Naresuan University, Thailand for providing financial support (Grant no. R2557B042), including the Graduate School of Naresuan University, Thailand for general funding. Many thanks to Mr. Roy Morien of the Naresuan University Language Centre for his editing assistance and advice on English expression in this. Many thanks go to my classmates for their information and encouragement.

Titiporn Chorchong

Title	CHARACTERIZATION AND APPLICATION OF ANODIZED ALUMINIUM FOR SELECTIVE SOLAR ABSORBER IN PARABOLIC TROUGH COLLECTORS (PTC)
Author	Titiporn Chorchong
Advisor	Tawat Suriwong, Ph.D.
Co - Advisor	Sukruedee Sukchai, Ph.D. Thotsaphon Threrujirapapong, Ph.D.
Academic Paper	Thesis Ph.D. in Renewable Energy, Naresuan University, 2015
Keywords	Anodized Aluminium, Parabolic Trough Collectors, Thermal Efficiency, Solar Receiver, Selective Absorber

ABSTRACT

This study focused on the characterization of the specific properties of the Tin-pigmented alumina (Sn-Al_2O_3) for using as a solar absorber material on parabolic trough collector (PTC). Sn-Al_2O_3 films were prepared with three different thicknesses (14.2, 15.2 and 18.9 μm) on aluminium tube grade 6063 substrate by an anodizing process. According to the results, the Sn-Al_2O_3 samples exhibited dark black surface color which enhanced the effectieness of the material as a solar collector. The solar absorptance (α) of each thickness were 0.94 for 14.2 μm, 0.94 for 15.2 μm and 0.93 for 18.9 μm over the wavelength range of 300-2,500 nm., corresponding to the theoretical properties of the solar absorber. The thermal efficiency measurements of the prototype PTC using the Sn-Al_2O_3 as the absorber were increase with increasing the thickness of Sn-Al_2O_3 films. The 18.9 μm thick film was the highest thermally efficiency. An economic analysis identified the Life Cycle Cost (LCC) for each thickness as 61,989.84 Baht (14.2 μm), 61,994.90 Baht (15.2 μm) and 61,994.90 Baht (18.9 μm), and the Levelized Cost of Energy (LCOE) for each thickness as 4.67 Baht (14.2 μm), 3.79 Baht (15.2 μm) and 3.47 Baht (18.9 μm). Based on technical and economic analysis, it can be concluded that the Sn-Al_2O_3 films on aluminium tube can be applied as a solar absorber in PTC due to the high α, which is similar to commercial solar absorber, and able to produce at aluminium factory in Thailand.

LIST OF CONTENTS

LIST OF CONTENTS (CONT.)

LIST OF CONTENTS (CONT.)

LIST OF TABLES

LIST OF TABLES (CONT.)

LIST OF FIGURES

LIST OF FIGURES (CONT.)

LIST OF FIGURES (CONT.)

CHAPTER I

INTRODUCTION

Rationale for the study and statement of the problem

In the first quarter of 2015, over 33 million tons of crude oil equivalent was consumed for the production of electrical power in Thailand. This was a 4.3% increase when compared with the same period in the previous year. This cost nearly 447 billion Baht. Costs are continually increasing because of economic growth. Refined oil accounted for the greatest amount of oil (48.3%), followed by electricity (18.7%), traditional renewable energy (11.5%), renewable energy (7.9%), natural gas (7.7%) and coal (5.9%) [1].

Historically, fossil energy has been the primary resource used for power production, which has been attended by a dramatic decline in the readily available and easily accessible sources of this energy source. The geographic distribution of the currently known and available sources around the world, and the potential sources, has created a situation of instability in prices and supply, primarily due to political problems and conflict. Of major significance today is the problem of environmental pollution causing perceivable climate change and global warming as a result of the burning of fossil fuels releasing carbon dioxide into the atmosphere. This is becoming a matter of global importance, and, in some nations viz. Pacific Island nations, the Maldives and Bangladesh, the impact of rising oceans is becoming catastrophic. All countries, including Thailand, must be aware of this serious problem and implement policies and processes to deal with it.

Attempts to replace fossil fuels as an energy source by using alternative, renewable energy are being implemented in many countries. Renewable energy resources including solar, wind, biomass, hydro, wave and tidal energies, which are almost infinitely available and are pollution free (not counting the possible visual pollution of large wind turbines which has inspired a political debate at the highest levels in Australia).

Currently solar energy is of significant interest as a viable and potentially competitively priced form of renewable energy, and is being considered and developed as an alternative energy resource in Thailand. Thailand has major solar assets, being located in a tropical region and receiving substantial solar radiation throughout the whole year in most parts of the country. The country receives approximately 18.2 MJ/m^2-day of solar energy. The ratio of diffuse and total radiation is 0.42 and the remaining proportion is beam radiation, giving solar energy use a relatively high efficiency. Being clean, non-polluting and plentiful makes solar energy technology development almost an imperative. Nowadays, most solar energy research is being developed and generally applied in two major areas: 1) heat energy directly used in water heating, solar energy food baking stove, mostly however in domestic usage, and 2) electricity production from solar energy in a variety of ways, including solar cell, solar collectors, radiation intensifying using hyperbolic collectors, with oil or molten salt heat storage, among other applications of solar energy for power production.

The radiation on the earth's surface is not highly intensive. The various solar energy technologies currently in use or in development are necessary for collecting or receiving this solar energy and transforming it into heat energy. Such technology can be classified into two types: 1) non-focusing solar collectors e. g. a flat plate solar collectors and 2) focusing solar concentrators e.g. a central solar concentrator, parabolic dish solar concentrator and a parabolic trough collector [2, 3, 4, 5]. Commercial solar cells are also extensively used and they are stable and inexpensive.

According to previous research studies, electricity production by a parabolic trough system costs less than photovoltaic production and will be able to compete with other types of energy production systems in the future [6]. The main part of parabolic trough technology is the solar absorber. If the absorber is highly effective, there is a major solar gain. However, solar absorbers are not produced in Thailand and are imported from other countries making them very expensive.

The use of anodized aluminum covered with aluminum oxide (Ni- Al_2O_3) on the film layer makes an effective solar absorber. This system is suitable for medium temperatures in the range 300 °C - 500 °C [7, 8, 9]. Alternatively, Kennedy [9] suggested that a solar absorber for concentrating solar power (CSP) in temperatures higher than 500 °C, using coatings of Co-Al_2O_3, Mo-Al_2O_3, W-Al_2O_3, Pt- Al_2O_3, and

Al_2O_3-Pt- Al_2O_3, could be prepared using the RF Sputtering technique and chemical vapor deposition (CVD), but are expensive and difficult to prepare. One element that has received little or no research interest for the purpose of coating on the aluminum oxide film layer is Sn.

For the purpose of the current research, the application of tin has been studied. Using Sn on the aluminum oxide film layer by anodizing to make it a selective solar absorber in parabolic trough collector was considered to be a worthwhile topic of research for a variety of reasons. In Thailand Sn mining and processing is an established industry, therefore using Sn would not require importation of the metal. This would reduce solar technology production costs as well as developing the technology within the country, thereby providing the country with its own technology and innovative development of an industry which could compete in world trade. As well, in order to reduce the cost for this technology and because of future commercial benefits, this research focused on anodized aluminum which is commonly found in Thailand, and therefore easily produced for use in high quality solar absorbers in parabolic trough collectors. Anodized aluminium is useable in the lower temperature ranges of 300 ^{o}C -500 ^{o}C and so the research focused on the production of hot water systems as the testing technology.

Purpose of the study

1. To identify and understand the characteristics of anodized aluminium tubing in order to apply it as a solar receiver in parabolic trough collectors.

2. To design and fabricate a parabolic trough collector prototype using an anodized aluminium tube as the solar receiver.

3. To evaluate the thermal efficiency of the parabolic trough collector system.

4. Perform an economic assessment of the use of a tube solar receiver surfaced with anodized aluminium.

Scope of the study

1. Sn-pigmented aluminium oxide film (Sn-Al_2O_3) was used as the selective coating material.

Anodizing normally uses colors created from organic and inorganic substances, usually Sn and nickel, which have the properties needed for a solar receiver, such as durability. They also work better than dyes at high temperatures. However, no research into the addition of Sn into an aluminum oxide film has been previously undertaken and published. Therefore, given the various factors of the availability and cost of this substance in Thailand, this is an interesting substance for research into its use as a parabolic trough receiver.

2. Aluminium tube grade 6063 was used as a receiver for the parabolic trough collector because it is generally used, easy to find, able to be anodized with a beautiful coating layer (aesthetics), is durable and able to work at a high water temperature.

3. The parameters of the parabolic trough collector design are as follows:

3.1 A rim angle of 90°, which is the angle which produces the highest intensity of solar radiation on to the focal point of the receiver.

3.2 A 1.8 m aperture of the parabola, a suitable size reducing the aluminium bending during the installation of the parabolic trough prototype.

3.3 The dimensions of the aluminium tube are 2.54×10^{-2} and 2 m for the outer diameter, and length, which is commercial market size, widely used, cheap and unable to be bent during the test.

The thickness of the anodized aluminum was classified into 3 levels: 14.2 μm, 15.2 μm and 18.9 μm. These were prepared using a commercial anodizing process.

4. Thermal efficiency testing was performed by field tests following the ASHRAE 93-1986 standard.

Benefits of the study

This research demonstrated the beneficial effects of applying a tin based film on the surface of an anodized aluminium tube for use in a Parabolic Trough Collector. This process, not previously used in industry, was shown to produce a significantly more efficient solar absorber, which can thereby increase the efficiency of, particularly, solar hot water generating systems.

The experimental testing of Sn-Al_2O_3 therefore is in fact the discovery of a new industrial anodizing material.

As this new industrial anodizing material is readily available in Thailand the further benefit of this study is that Thai industry can now be informed of the effectiveness of this material and, as it is a locally produced, low cost material can be used to produce competitively priced parabolic trough receivers of greater efficiency and effectiveness than those currently, commercially available, but usually imported.

CHAPTER II

REVIEW OF RELATED LITERATURE AND RESEARCH

Solar Collectors

Solar energy collectors are special kinds of heat exchangers that transform solar radiation energy into internal energy of the transport medium. The main component of any solar system is the solar collector. This is a device that absorbs the incoming solar radiation, converts it into heat, and transfers the heat to a fluid (usually air, water or oil) flowing through the collector. The solar energy collected is carried from the circulating fluid either directly to a hot water system or circulated through space conditioning equipment or to a thermal energy storage tank, from which it can be subsequently drawn for use at night or on cloudy days. There are basically two types of solar collectors; non-concentrating or stationary and concentrating. A non-concentrating collector has the same flat area for intercepting and absorbing solar radiation, whereas a sun-tracking concentrating solar collector usually has concave reflecting surfaces to intercept and focus the sun's beam radiation to a smaller receiving area, thereby increasing the radiation flux. Concentrating collectors are suitable for high-temperature applications. Solar collectors can also be distinguished by the type of heat transfer liquid used (water, non-freezing liquid, air or heat transfer oil) and whether they are covered or uncovered. A large number of solar collectors are available on the market. A comprehensive list is shown in Table 1.

Solar energy collectors are typically distinguished by their motion, being either stationary, single-axis tracking or two-axis tracking. They are also distinguished by their operating temperature. First, stationary solar collectors are described. These collectors are permanently fixed in position and do not track the sun. Three main types of stationary collectors are:

1. Flat-plate collectors (FPC).
2 Stationary compound parabolic collectors (CPC).
3. Evacuated tube collectors (ETC).

Table 1 Solar Energy collectors [10]

Motion	Collector type	Absorber type	Concentration ratio, C	Indicative temperature range (°C)
Stationary	Flat-plate collector (FPC)	Flat	1	30-80
	Evacuated tube collector (ETC)	Flat	1	50-200
Single-axis tracking	Compound parabolic collector (CPC)	Tubular	1-5	60-240
			5-15	60-300
	Linear Fresnel reflector (LFR)	Tubular	10-40	60-250
	Cylindrical trough collector (CTC)	Tubular	15-50	60-300
	Parabolic trough collector (PTC)	Tubular	10-85	60-400
Two-axis tracking	Parabolic dish reflector (PDR)	Point	600-2000	100-1500
	Heliostat field collector (HFC)	Point	300-1500	150-2000

Note: Concentration ratio is defined as the aperture area divided by the receiver/ absorber area of the collector.

Parabolic Trough Collectors (PTC)

Parabolic Trough Collectors or PTCs are one type of compound parabolic collectors able to deliver high temperatures with good efficiency. Systems using PTCs can be light structures built with low-cost technology for heat processing applications up to 400 °C. PTCs can effectively produce heat at temperatures between 50 °C and 400 °C. They are made by bending a sheet of reflective material into a parabolic shape. A black metal tube, covered with a glass tube to reduce heat loss, is placed along the focal line of the receiver. When the parabola is pointed toward the sun, parallel rays incident on the reflector are reflected onto the receiver tube. The concentrated radiation reaching the receiver tube heats the fluid that circulates through it, thus transforming the solar radiation into useful heat. It is sufficient to use a single-axis

tracking of the sun; therefore, long collector modules are produced. The collector can be oriented in an east-west direction, tracking the sun from north to south, or in a north-south direction, tracking the sun from east to west. The advantages of the east-west tracking mode is that it requires very little collector adjustment which must be done during the day. The full aperture always faces the sun at noon. However the collector performance during the early and late hours of the day is greatly reduced, due to large incidence angles (cosine loss). North-south oriented troughs have their highest cosine loss at noon and the lowest in the mornings and evenings, when the sun is due east or due west. No comparisons were made of the relative efficiency of these models, as this was beyond the scope of the current study, and therefore not of interest to us.

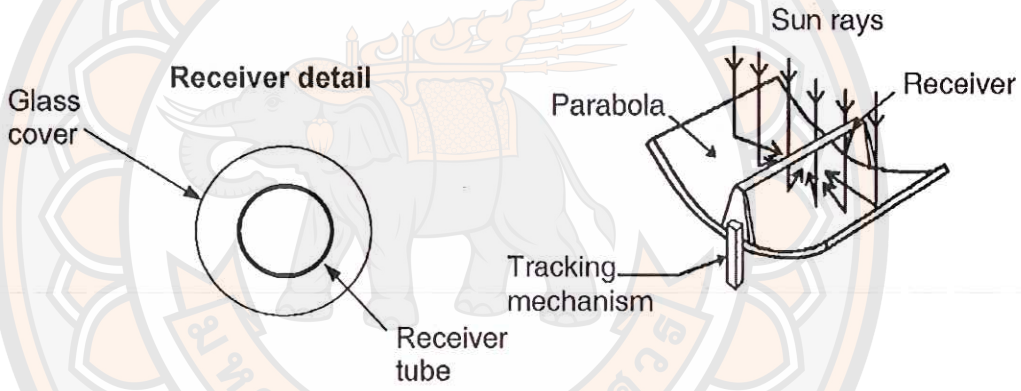

Figure 1 The structure of parabolic trough collectors (PTC) [10, 11]

The structure of the PTC consists of 3 parts: reflector, receiver tube and glass cover. The reflector is parabolic, reflecting the sun rays onto the focus point (see Figure 1), which is the receiver tube covered by the solar selective material. Generally, the receiver is dark or opaque and it is able to absorb the sun rays. The third part, glass cover, surrounds the tube and contains a vacuum. The vacuum reduces heat loss by convection and heat conduction, while allowing the solar radiation to reach the absorber coating. Thermal emission from the absorber coating is minimal and further reduced by the surrounding vacuum [10, 11, 12, 13, 14].

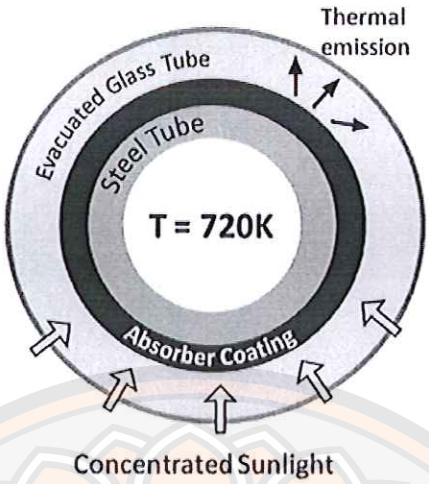

Figure 2 The cross section of the receiver tube covered by solar absorber [15]

Selective Solar absorber

The absorber coating is an important material because its surface is highly reflective, which is needed to increase the solar absorption efficiency (to increase the coefficient of solar absorption). The black coating material for the tube which has previously been developed in initial solar technology research projects lacks any ray selection ability. Subsequently, it has been improved to be "the selective absorber". This improvement is important because the coefficient of emittance (ε) reduces the heat conduction resulting in heat loss reduction.

In order for the solar absorber to be effective, the absorption should be high while the emission should be low. The wave length coefficients of these are different, as shown in Figure 3, which shows the difference between the solar absorber on the tube working at 200 °C. This shows that it is impossible to design a solar absorber to be effective using a coating material that can work well at less than 2.5 μm. wavelength (absorbing coefficient $\alpha = 0.95$). While the heat loss by thermal emission is reduced at the receiver tube at 2.5 μm. wave length (thermal emission coefficient $\varepsilon = 0.05$ to $\varepsilon = 0.20$), the 2 types of coating material with solar absorption properties and low thermal emissions are called selective solar absorbers [13].

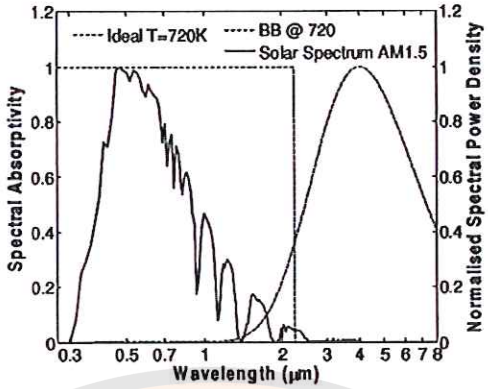

Figure 3 The spectrum of the solar absorption and the thermal emission [15]

Previous solar absorber coatings include: [13]

1. Solar paint: no selective absorbing property
2. Nickel-pigmented aluminium oxide on aluminium: selective absorbing property
3. Black chrome directly on copper: selective absorbing property
4. Cobalt sulphide/oxide on steel sheet: selective absorbing property.
5. Selective acting enamel on steel

The recent solar absorbing materials

1. Black Nickel: In the process of coating, the copper tube is dipped into a basin of cleansing agents as a solvent. It is then subjected to an electrolyte process for coating nickel and/or chrome onto the copper tube. This process is a well-understood and practical process and produces a durable coated material for long-term serviceability. It is, however, harmful to health if the operators do not take appropriate preventative and safety measures.

2. Black Crystal: After cleaning the copper plate or tube, the black crystal coating process uses nickel as the coating film, following which the plate or tube is coated with liquid glass in an electroplating process. The coating area includes alcohol solutions which create an alcohol vapor in the operational area. Safety measures should therefore be taken by the operators in the area.

3. Physical Vapor Deposition (PVD): This is a coating technique done under vacuum conditions. The process involves shooting electron beam into a crucible

containing the receiver tube coating materials. The materials, such as copper, drop onto the tube in the crucible. Low pressure oxygen and nitrogen gas is released into the vacuum system as well.

4. Sputtering: Sputtering is a process where a target of one chemical composition (e.g. elemental Si) reacts in the presence of a gas or a mixture of gasses (e.g. Ar + O_2) to form a coating of a different chemical composition (e.g. compound SiO_2). Argon is in most cases the main gas and the amount of a reactive gas introduced into a process chamber is controlled to either achieve a certain amount of doping or to produce a fully reacted compound.

5. PECVD process: Plasma Enhanced Chemical Vapor Deposition (PECVD) is a process by which thin films of various materials can be deposited on substrates at lower temperature than that of standard Chemical Vapor Deposition (CVD). In PECVD processes, deposition is achieved by introducing reactant gases between parallel electrodes; a grounded electrode and an RF-energized electrode. The capacitive coupling between the electrodes excites the reactant gases into plasma, which induces a chemical reaction and results in the reaction product being deposited on the substrate. The substrate, which is placed on the grounded electrode, is typically heated to 250 °C to 350 °C, depending on the specific film requirements.

The absorbing coefficient of the selective receiver solar absorbing material, recently commercially available, is ≥0.95 within the solar spectrum. Solar paint, a coating material that is not a solar selective receiver, has an absorbing coefficient between 0.9-0.95. The individual absorption rates of absorbing layers currently sold in the marketplace are shown in Table 2.

Table 2 Specifics properties of solar selective coating currently sold [14]

Firm	Product	Solar Absorptance α	Emittance ε	Coating	Process	Absorber	Available
Tekno Term	Sun Strip	0.95±0.02	0.15±0.02	Ni on oxidized Aluminium	electro-chemical	Aluminium	yes
MTI	Black Chrome	0.95±0.02	0.12±0.02	Black Chrome on Nickel	Coil process	Copper	yes
Batec	Batec	0.95±0.02	0.12±0.02	Black Nickel	Coil process	Copper	yes
Tinox	Tinox	0.95	0.05	Tinox	PVD	Copper	yes
Interpane	Suns-select	0.95	0.05	Material mixture	Sputter	Copper	yes
Ikarus Solar	Absorber 2000	0.95	0.1	a-c:H/metal	PECVD	Copper	vague

A particular aluminium film for flat plate collectors is sold by Tekno Term Energi in Sweden and Showa in Japan. The Al_2O_3-Ni solar absorber on the aluminium film is described by the manufacturers to have the solar absorptance (α) to emissivity (ε) coefficient between 300 °C – 500 °C of 0.85-0.97/0.08-0.21 (100 °C). Apart from nickel (Ni), other metals such as vanadium (V), chromium (Cr), cobalt (Co), copper (Cu), Molybdenum (Mo), silver (Ag), silicon (Si) and tungsten (W) can also be the selective receiver. [9]

In Thailand, each of these absorbing materials must be imported and the price is very expensive. Each absorber works properly at different ranges of temperature, so material selection for coating the receiver tube should be suitable for each range of temperature. In addition, appropriate selection can help increase efficiency of the receiver tube and extend the working period of the system.

Table 3 Mid-Temperature Selective Surfaces [9]

Rank	Material	Substrate	Fabrication	Absorptance α	Emittance ε (100 °C)	Stabilily (°C) Vacuum	Air
2	TSSS[1]	Al	Paint	0.92	<0.015	-	<135
2	PbS	Al	Evaporation Pyrolysis	0.93-0.99	0.21-0.10	-	200
2	$NiCrO_x$	SS[2]	Sputtering	0.8	0.14	-	<200
		Cu/Polyamide		0.92-0.93	0.06	-	<200
2	Colored SS	SS	Chemical conversion	0.62-0.93	0.1	-	<200
2	Black nickel NiS-ZnS	Steel Ni coated steel	Electro deposition	0.88-0.96	0.03-0.10	-	<200
3	Ni-Sn	Cu	Electro Deposition/Sol-gel	0.92-0.98	0.08-0.25	-	300
3	Ag dielectric	Al	Biomimetic Sol-gel	-	-	-	300
3	Black copper BlCu-Cu_2O:Cu	Cu	Electro deposition	0.97-0.98	0.02	370	250
3	Black chrome	Ni-Cu	Electro deposition	0.97	0.09	400	350
3	Cr-Cr_2O_3 Mo/ Cr_2O_3	Cu steel		0.95	<0.30	-	425
3	Ni-NiO_x	Al	reactive sputtering	0.96	0.10	-	300
	Ni pigmentedAl_2O_3	Al	Anodization	0.85-0.97	0.08-0.21	-	300-400

Rank = Indicates if the material should be investigated for CSP applications 1 = Yes, 2 = No, 3 = Maybe

TSSS[1] = Thickness-sensitive spectrally selective

SS[2] = Stainless steel

Table 3 shows a summary of coating materials available for receiver tubes together with their suitable concentrating collectors in the 100 °C – 400 °C, middle - temperature, range.

Table 4 High-Temperature Selective Surfaces [9]

Rank	Material	Substrate	Fabrication	Absorptance α	Emittance ε (100 °C)	Stability (°C)	
						Vacuum	Air
2	$Ni\text{-}Al_2O_3$	Mo-Ni-	RF sputtering	0.94	0.07		350-400
2	SiO_2AR	SS		0.94	0.04	500	-
3	$Co\text{-}Al_2O_3$	Ni or Al	RF sputtering	0.96	0.16(350)	350-500	-
1	$Mo\text{-}Al_2O_3$	Steel	RF sputtering	0.97-0.98	0.1-0.07(400)	-	-
	$W\text{-}Al_2O_3$		CVD	0.85	0.04	500	
	$W\text{-}Al_2O_3$				-		
1	$Pt\text{-}Al_2O_3$	Cu	RF sputtering	-	0.08	-	600
1	Al_2O_3- $Pt\text{-}Al_2O_3$			0.90-0.98	-		
	Double					500	
1	$Mo\text{-}Al_2O_3$	Cu	DC sputtering	0.96	0.06(350)	350-500	
2	SS-AlN			0.95	0.10(350)	500	
3	Mo-AlN			0.92-0.94	0.08-0.10(350)	500	
1	W-AlN						
1	$Ni:SiO_2$	Al, Cu	DC reactive	0.90-0.96	0.03-0.14	-	400-800
	Cr:SiO		sputtering				(Ar)
3	TiN	Cu, Al	DC reactive		0.14-0.40	-	500
1	$Ti_{1-x}Al_xN$		sputtering	0.80			750-900
3	M_bO_c+$M'Fe_2O_4$	Ni-Mo alloy	Painting	>0.90	>0.45	-	700
			Arc plasma				1060
3	VB_2, NbB_2, TaB_2, iB_2,	Glass	DC reactive	0.99	0.95-0.97	2300-3040	
	ZrB_2, LaB_6, WSi_2, iSi_2		Sputtering			(MP)	
1	$Si_3N_4AR\text{-}ZrB_2$	ZrB_2	CVD	0.88-0.93	0.08 to 0.10		500

To design and apply a solar absorber to work appropriately and to be suitable for concentration collectors, the most important factor is the concentration ratio (C). This factor is the ratio of the aperture area reflection (A_a) to the receiver-absorber area (A_r) as shown in Equation 1:

$$C = \frac{A_a}{A_r} \qquad (1)$$

To determine the best concentration ratio (C), the variables that must be considered are: the distance from the center of the sun (R), radius of the sun (r) and the collector half acceptance angle (θ_m) as shown in Figure 4.

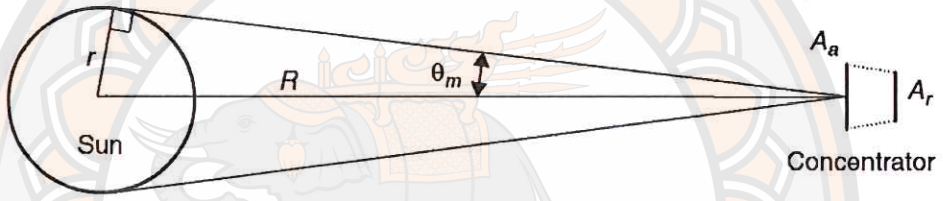

Figure 4 The schematic of the relation between the sun and the concentration collectors [10, 11, 12, 13, 14, 15, 16]

The highest range of C for the circular concentrations or full tracking system can be calculated by the equation:

$$C_{max} = \frac{1}{sin^2(\theta_m)} \qquad (2)$$

The equation $\sin(\theta_m) = r/R$ gives the highest range of C in a linear concentrator system. C can also be calculated by the equation:

$$C_{max} = \frac{1}{sin^2(\theta_m)} \qquad (3)$$

According to the relation between the sun and the earth, the range of the $2\theta_m$ = 0.53 degrees of angle or 32 minutes of arc. That range is taken in Equations 2 and 3. The calculated value for the highest range of C for the circular concentrators system is 46, 747 and the highest range of C for the linear concentrators system is 216 [10-16]. The collector efficiency (η) shows the relationship between the heat

produced by the solar collector and the solar radiation number on the collector, at the same time. The η is non-dimensional or dimensionless which means that it will be a percentage (%). To calculate η many parameters are necessary, as shown in Equation. 4 and Table 5 [13].

$$\eta = \eta_o - \frac{a_1(\nu_m - \nu_L)}{E_e} - \frac{a_2(\nu_m - \nu_L)^2}{E_e} \quad (4)$$

Table 5 The meaning of each parameter and symbol that is used in the solar collectors efficiency (η) calculation [14]

Abbreviation	Unit	Description	Value
η	[-];[%]	Collector efficiency	-
η_0	[-];[%]	Zero loss collector efficiency Φ =0° optical efficiency = $\alpha\tau F'$	-
a_1	W/(m^2·K)	Linear heat transfer coefficient	1.2-4
a_2	W/(m^2·K^2)	Quadratic heat transfer coefficient	0.005-0.015
ν_e	°C	Heat transfer fluid inlet temperature into collector	-
ν_a	°C	Heat transfer fluid outlet temperature from collector	-
ν_m (or T_{col})	°C	Mean temperature of heat transfer fluid in absorber	-
ν_L (or T_a)	°C	Ambient air temperature	-
E_e (or E_g)	W/m^2	Solar irradiance	1,000
F'	-;%	Absorber efficiency factor	0.92-0.97
τ	-;%	Transmission factor of cover	0.88-0.91
α	-;%	Absorption factor of absorber	0.90-0.96

Table 5 (cont.)

Abbreviation	Unit	Description	Value
Additional values: $K(\Phi)$	-; %	Incident angle modifier dependent on incident angle	-
$a_{eff} = a_1 + a_2 \cdot \Delta\nu$	-	Effective, temperature independent heat transfer coefficient	-
c	kJ/(m^2 ·K)	Thermal capacity of collector	-

Parabolic Trough Collectors System Design

The parabolic trough collectors diagram in Figure 5 shows that there are many factors that are important such a system.

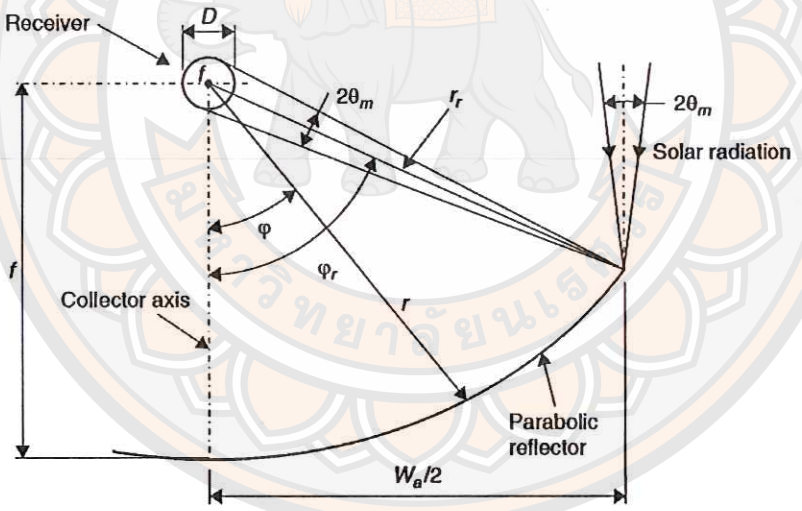

Figure 5 The cross section of a parabolic trough collectors [10]

The diameter D of the receiver tube can be calculated by Equation 5.

$$D = 2r_r \sin(\theta_m) \qquad (5)$$

where r_r is the rim radius and θ_m is the angle between the receiver tube and the half acceptance angle of the parabolic reflector. r can be calculated by Equation 6.

$$r = \frac{2f}{1+\cos(\varphi)} \qquad (6)$$

where f is the length of the parabola focal distance (m) and φ is the angle between the collector axis and the reflected beam at the focus point. φ is from 0 to φ_r (rim angle). r increases from f to r_r. According to the theory, the size of the focused image is bigger from $2fsin(\theta_m)$ to $2r_r sin(\theta_m)/cos(\varphi_r+\theta_m)$. So, this is the image enlargement from the normal plane to the parabolic axis by calculating rim angle φ_r from the equation:

$$r_r = \frac{2f}{1+cos(\varphi_r)} \tag{7}$$

The aperture of the parabola (W_a) can be calculated by the equation:

$$W_a = 2r_r sin(\varphi_r) \tag{8}$$

Equation 7 is replaced in Equation 8 then reformed to be Equation 9.

$$W_a = \frac{4fsin(\varphi_r)}{1+cos(\varphi_r)} \tag{9}$$

Equation 9 is compressed into:

$$W_a = 4ftan\left(\frac{\varphi_r}{2}\right) \tag{10}$$

According to Equation 1, we can make the concentration ratio for the tube as:

$$C = \frac{W_a}{\pi D} \tag{11}$$

D and W_a is replaced by the range from Equation 5 and 9 into Equation 11. C can be calculated by Equation 12.

$$C = \frac{sin(\varphi_r)}{\pi sin(\theta_m)} \tag{12}$$

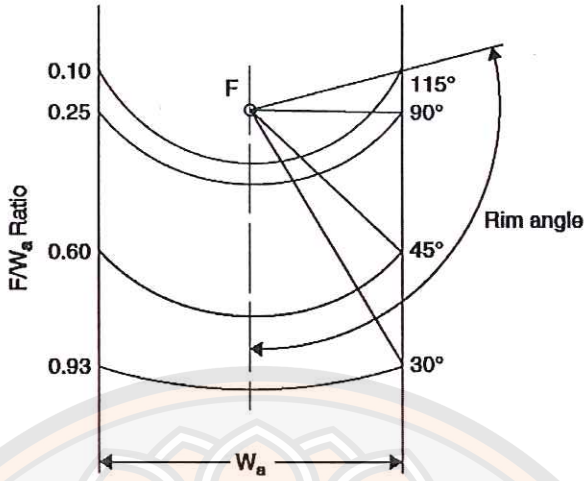

Figure 6 The relation between parabola focal length and rim angle [10]

Figure 6 shows the different appearances of the rim angle (W_a is constant) and shows the percentage of the focus range for the aperture. It also shows that the ratio F / W_a at 0.25 is equal to the rim angle (90°).

The length of the parabolic surface (S) can be calculated by Equation 13.

$$S = \frac{H_p}{2}\left\{sec\left(\frac{\varphi_r}{2}\right)tan\left(\frac{\varphi_r}{2}\right)+\left[sec\left(\frac{\varphi_r}{2}\right)+tan\left(\frac{\varphi_r}{2}\right)\right]\right\} \quad (13)$$

W_a is the aperture of the parabola (m). Normally, H_p is equal to W_a. Figure 7 shows the different range of the rim angle. (W_a is stable)

Thermal Analysis of Parabolic Trough Collectors

The generalized thermal analysis of a concentrating solar collector is similar to that of a flat-plate collector. It is necessary to derive appropriate expressions for the collector efficiency factor F', the overall heat transfer coefficient U_L and the collector heat removal factor F_R. For the loss coefficient, the heat transfer relations of glazed tubes can be used. Thermal losses from the receiver must be estimated, usually in terms of the overall heat transfer coefficient, U_L, which is based on the area of the receiver. The method for calculating thermal losses from the concentrating thermal

losses from the concentrating collector receivers, cannot be as easily summarized as for flat-plate receivers, because many designs and configurations are available.

For a bare tube receiver, assuming no temperature gradients along the receiver, the loss coefficient, considering convection and radiation from the surface and conduction through the support structure, is given by

$$U_L = h_w + h_r + h_c \tag{14}$$

The linearized radiation coefficient can be estimated from

$$h_r = 4\sigma\varepsilon T_r^3 \tag{15}$$

If a single value of h_r is not acceptable due to large temperature variations along the flow direction, the collector can be divided into small segments, each with a constant h_r.

For the wind loss coefficient, the Nusselt number can be used.

For $0.1 < \text{Re} < 1000$,

$$Nu = 0.4 + 0.54(Re)^{0.52} \tag{16.1}$$

For $1000 < \text{Re} < 50,000$,

$$Nu = 0.3 + (Re)^{0.6} \tag{16.2}$$

Estimation of the conduction losses requires knowledge of the construction of the collector, i.e. the way the receiver is supported.

Usually, to reduce the heat losses, a concentric glass tube is employed around the receiver. The space between the receiver and the glass is usually evacuated, in which case the convection losses are negligible. In this case, U_L, based on the receiver area A_r, is given by

$$U_L = \left[\frac{A_r}{(h_w + h_{r,c-a})A_c} + \frac{1}{h_{r,r-c}} \right]^{-1} \tag{17}$$

Where $h_{r,c-a}$ = The linearized radiation coefficient from cover to ambient estimated by Equation 15

A_c = The external area of glass cover (m^2)

$h_{r,r-c}$ = The linearizer radiation coefficient from the receiver to the cover, given by

$$h_{r,r-c} = \frac{\sigma\left(T_r^2 + T_c^2\right)(T_r + T_c)}{\frac{1}{\varepsilon_r} + \frac{A_r}{A_c}\left(\frac{1}{\varepsilon_c} - 1\right)} \quad (18)$$

In the preceding equations, to estimate the properties of the glass cover, the temperature of the glass cover, T_c, is required. This temperature is closer to the ambient temperature than the receiver temperature. Therefore, by ignoring the radiation absorbed by the cover, T_c may be obtained from an energy balance:

$$A_c(h_{r,r-a} + h_w)(T_c - T_a) = A_r h_{r,r-c}(T_r - T_c) \quad (19)$$

Solving Equation 19 for T_c gives

$$T_c = \frac{A_r h_{r,r-c} T_r + A_c(h_{r,c-a} + h_w) T_a}{A_r h_{r,r-c} + A_c(h_{r,c-a} + h_w)} \quad (20)$$

The procedure finds T_c by iteration, i.e. estimate U_L from Equation 17 by considering a random T_c (close to T_a). Then, if T_c obtained from Equation 20 differs from the original value, iterate. Usually, no more than two iterations are required.

If radiation is absorbed by the cover, this needs to be considered. In this case the appropriate term must be added to the right-hand side of Equation 17. The principles are the same as those developed earlier for the flat-plate collectors.

Next, the overall heat transfer coefficient U_o needs to be estimated. This should include the tube wall because the heat flux in a concentrating collector is high. Based on the outside tube diameter, this is given by

$$U_o = \left[\frac{1}{U_L} + \frac{D_o}{h_{fi} D_i} + \frac{D_o \ln(D_o / D_i)}{2k}\right] \quad (21)$$

Where D_o = the receiver outside tube diameter (m).

D_i = the receiver inside tube diameter (m).

h_{fi} = the convective heat transfer coefficient inside the receiver tube ($W/m^2 \cdot K$).

The convective heat transfer coefficient h_{fi}, can be obtained from the standard pipe flow equation:

$$Nu = 0.023(Re)^{0.8} + (Pr)^{0.4} \qquad (22)$$

Where Re = Reynolds number = $\rho V D_i / \mu$

Pr = Prandtl number = $C_p \mu / k_f$

μ = Fluid viscosity ($kg / m \cdot s$)

k_f = Thermal conductivity of fluid (W/m · K)

It should be noted that Equation22 is for turbulent flow ($Re > 2300$). For laminar flow, $Nu = 4, 364$ = constant.

The instantaneous efficiency of a concentrating collector may be calculated from an energy balance of its receiver. The useful energy delivered from a concentrator is

$$Q_u = G_B \eta_0 A_a - A_r U_L (T_r - T_a) \qquad (23)$$

Notice that, because concentrating collectors can utilize only beam radiation, G_B is used in Equation 23 instead of the total radiation, G_t.

The useful energy gain per unit of collector length can be expressed in terms of the local receiver temperature, T_r, as

$$q'_u = \frac{Q_u}{L} = \frac{A_a \eta_o G_B}{L} - \frac{A_r U_L}{L}\left(T_r - T_a\right) \qquad (24)$$

In terms of the energy transfer to the fluid at the local fluid temperature, T_f

$$q'_u = \frac{\left(\frac{A_r}{L}\right)(T_r - T_f)}{\frac{D_o}{h_{fi} D_i} + \left(\frac{D_o}{2k} ln \frac{D_o}{D_i}\right)} \qquad (25)$$

If T_r is eliminated from Equation 24 and 25, we have

$$q'_u = F' \frac{A_a}{L} \eta_o G_B - \frac{U_L}{C}\left(T_f - T_a\right) \qquad (26)$$

Where F' is the collector efficiency factor, given by

$$F' = \frac{1/U_L}{\frac{1}{U_L} + \frac{D_o}{h_{fi}D_i} + \left(\frac{D_o}{2k} ln \frac{D_o}{D_i}\right)} = \frac{U_o}{U_L} \quad (27)$$

As for the flat-plate collector, T_r in Equations 23 can be replaced by T_i through the use of the heat removal factor, and Equation 23 can be written as

$$Q_u = F_R[G_B\eta_0 A_a - A_r U_L(T_i - T_a)] \quad (28)$$

Where F_R can be written as

$$F_R = \frac{m^{\cdot} C_p}{A_r U_L}\left[1 - exp\left[-\frac{U_L F' A_r}{m^{\cdot} C_p}\right]\right] \quad (29)$$

From Equation 28 the collector efficiency is obtained by dividing Q_u by $(G_B A_a)$ as

$$\eta = F_R\left[\eta_o - U_L\left(\frac{T_i - T_a}{G_B C}\right)\right] \quad (30)$$

Where C = concentration, $C = A_a / A_r$.

F_R is used by replacing A_c with A_r and using F' as given by Equation27, which does not include the fin and bond conductance terms used in flat-plate collectors.

In reality, the heat loss coefficient, U_L, is not constant but is a function of the collector inlet and ambient temperatures. Therefore,

$$F_R U_L = c_1 + c_2(T_i - T_a) \quad (31)$$

Where c_1 and c_2 = Linear (1st order) and Quadratic (2nd order) heat loss coefficients, respectively.

Substituting Equation 31 in Equation 28, can be written as

$$Q_u = F_R G_B \eta_0 A_a - A_r c_1(T_i - T_a) - A_r c_2(T_i - T_a)^2 \quad (32)$$

From Equation 32 the collector efficiency is determined by dividing Q_u by $(G_B A_a)$ as

$$\eta = F_R\eta_o - \frac{c_1(T_i - T_a)}{CG_B} - \frac{c_2(T_i - T_a)^2}{CG_B} \qquad (33)$$

Where $A_r / A_a = 1/C$

From Equation 33 if denote that $k_0 = F_R\eta_o$, $k_1 = c_1 / C$, $k_2 = c_2 / C$, and $y = ((T_i - T_a) / G_B)$, then

$$\eta = k_0 - k_1 y - k_2 G_B y^2 \qquad (34)$$

Anodized Aluminium

Aluminium is one of the elements symbolized as Al and has atomic number 13. This element is in the 3A family which is shiny and flexible. The ore of aluminium is bauxite and its special property is its ability to prevent oxidation (according to passivation). It is strong but still light. Aluminium is widely used in many industries where a light-weight but strong and durable metal material is required, such as for airplanes. Aluminium, apart from its light weight, strength and durability, is non-toxic, non-magnetic, is malleable and can be bent, lathed and melts at a low temperature. It is a good conductor of electricity. In an anodized form, anodized aluminium, it is highly corrosion resistant due to its layers of oxide protecting the aluminium surface. Its coefficient of thermal and electrical conductivity is high. The tensile strength of pure aluminium is 13,000 psi which can be increased by a cooling process or by adding a mixture of elements to aluminium which is treated by the right heat-treatment, which can increase its tensile strength up to 100,000 psi. Aluminium is most commonly alloyed with copper, zinc, magnesium, silicon, manganese and lithium. Small additions of chromium, titanium, zirconium, lead, bismuth or nickel are also made and iron is invariably present in small quantities. There are many grades of aluminium. Each grade has particular physical and mechanical properties. For the purpose of this research, the grade designated as grade 6063, which is commonly referred to as the architectural alloy, was selected. These are an extruded alloy with relatively high tensile properties, excellent finishing characteristics and a high degree of resistance to corrosion. This alloy is most often found in various interior and exterior architectural applications, such as windows, doors, store fronts and assorted trim items. It is the alloy best suited for anodizing applications - either plain or in a variety of colors. The

physical and mechanical properties of 6063 grade are shown in Tables 6 and 7, which indicate that it is appropriate as a solar absorber material. It is inexpensive and readily available in outlets throughout Thailand.

Table 6 Physical properties of 6063 aluminium grade [17]

Physical properties	Value
Melting range (°C)	600
Thermal expansion (K)	23.5×10^{-6}
Thermal conductivity (W/m·K)	200
Specific heat (J/kg·°C)	0.9
Electrical Resistivity (Ω/m)	0.035×10^{-6}

Table 7 Mechanical properties of 6063 aluminium grade [17]

Mechanical properties	Value
Yield strength (MPa)	89.6
Tensile strength (MPa)	152
Elongation (%)	20
Hardness (HB)	42
Young's modulus (GPa)	68.9

Aluminium anodizing is the process of applying aluminium oxide (Al_2O_3) to a surface, in a thin film. The film is thin because when the aluminium surface is full of aluminium oxide, it cannot react with oxygen in the atmosphere or in water. Therefore, the aluminium oxide film is highly resistant to corrosion. This process is similar to electroplating but the difference is that the aluminium substrate is the anode and a higher voltage is applied. There are no other elements that can absorb another element or can dye the aluminium film after anodizing. Generally, the color that is used is from either organic dyes or inorganic dyes such as tin (Sn) and nickel (Ni). These 2 elements have selective properties. They are strong and can work better than other dyes in high-temperature conditions. The chemical reaction of aluminium oxide film in sulfuric acid solution (H_2SO_4) as represented in the following:

$$4Al + 3H_2SO_4 + 3H_2O \xrightarrow{Energy} Al_2(SO_4)_3 + Al_2O_3\,(films) + 6H_2 \quad (35)$$

The feature of aluminium film according to the above equation, and illustrated in Figure 7, is that there are pores on the film surface. After the reaction, the film is sealed by hydrated Al_2O_3 ($Al_2O_3 \cdot (H_2O)_n$) in 93 °C hot water. This aluminium is called "clear anodizing". Inorganic elements can be added into the pore to color the film. This can be any color. This can be done not only to resist erosion, but also to make the tool more beautiful. Inorganic adding or electroplating is the process after the first aluminium oxide film is applied, by plating again. The process is shown in Figure 8. After plating, the pore sealing is the last process for making the film in any color by whatever element is added into the pores. If selective material or solar absorber material is added into the film pores, the effect is that the aluminium film is able to absorb solar energy as well as being solar selective. As a result, it is suitable for use as a solar absorber in a parabolic trough collector. The anodized aluminium process is shown in Figure 7.

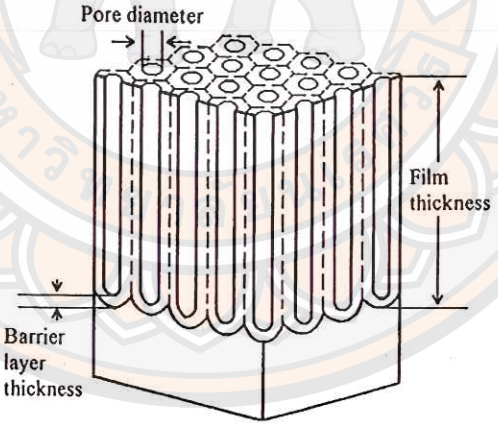

Figure 7 Aluminium Oxide film appearance after the anodizing process [18]

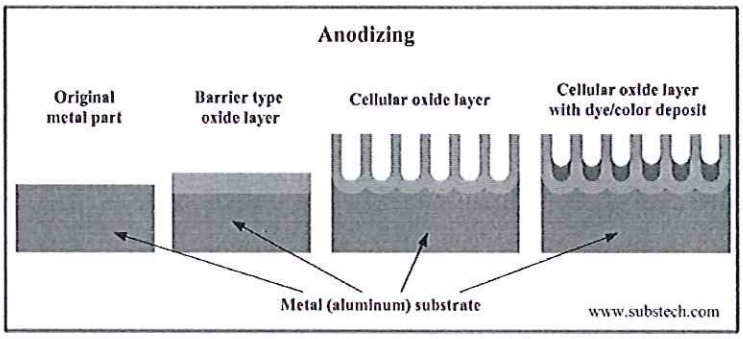

Figure 8 The aluminium oxide film electroplating process [19]

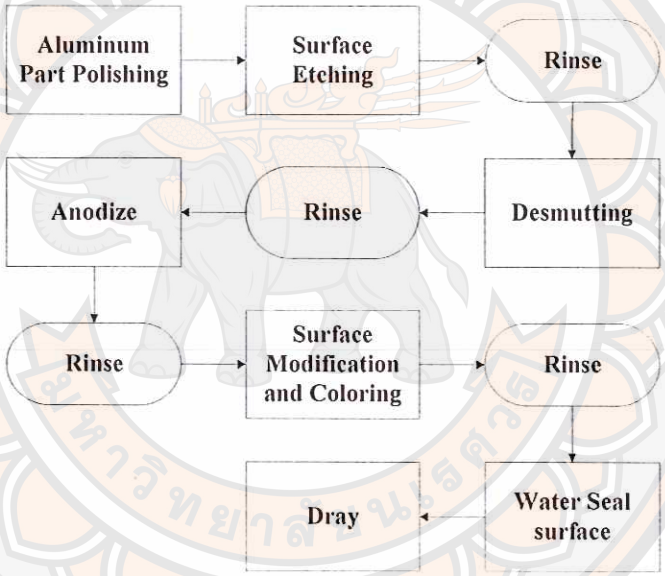

Figure 9 The aluminium anodizing process [20]

Life Cycle Cost

Life Cycle Cost Analysis (LCC) is an economic method for evaluating assets that takes into consideration all costs arising from owning, operating, maintaining, and disposing of the asset [21]. It is the total discounted cost of acquiring, operating and maintaining, and disposing of an asset over a fixed period of time [22]. LCC is a useful aid for comparing the lifetime cost of mutually exclusive assets to determine which asset provides the best value per dollars spent [22, 23, 24] and it should be performed early in the design process. Ashworth, however, does not believe that early LCC calculations have produced reliable forecasts. He noted that estimated values

might be quite different from actual values and that attempting to estimate far in the future could lead to forecasting errors. El Haram& Horner (2002) indicated that due to unreliable data it is difficult to define exact costs for each expense category - acquisition, facility management, and disposal [25]. Barringer and Weber (1996) noted that LCC is not an exact science; outputs are only estimates, and estimates are not accurate [26]. Nonetheless, given robust and realistic assumptions, LCC is an important tool for ranking cost of ownership between mutually exclusive alternatives. Realistic assumptions can be obtained from evaluating the performance, over time, of similar assets, conducting literature reviews, obtaining information from manufacturers, vendors, contractors, and using average support and maintenance costs [23]. Contractually, vendors and contractors usually identify the physical requirements for support of new assets or systems before the owners approve the acquisition [27]. The time period (useful life) associated with LCC must be well established and historically accurate. Additionally, the associated discount rate should be used with care, since there are differences between real and nominal discount rates. The former excludes inflation and the latter includes inflation. Thus, when comparing alternatives in a given period, the same discount rate must be used. Furthermore, the discount rate is likely to change from period to period, and there are many discount rates. When using the real discount rate in present value (PV) calculations, cost should be expressed in constant dollars [22]. Taxes and depreciation allowances should be accounted for in LCC calculations, as well as any local value effect. The local value effect refers to the market differential response to one alternate versus another, such as the rental for buildings with carpeted flooring are higher than for vinyl flooring. Depreciation is calculated either by the straight-line method, where a fixed percentage of the original cost is written-off each year, or the reducing balance method whereby the depreciation amount in any year is a percentage of the remaining balance brought forward from the previous year, and the depreciation amount reduces the remaining balance carried forward to the next year. Both are simple to use, and the choice of depreciation method is often based on taxation considerations. The straight-line method, however, is usually favored, being based on the principle that each period of the asset life should depreciate equally.

The Structure of Life Cycle Cost

Construction life cycle costing needs to include every expense of the equipment life cycle starting from the purchase and setup stage through to the disposal of the equipment. This is called the Costing Analysis Structure. The purpose of the analysis is to ensure all appropriate costs are included in the analysis. Table 8 shows the general structure of life cycle costing as an example of the range of costs to be considered. In practice, all costs should be included and calculated for the specific project.

Table 8 The Structure of Life Cycle Costing System [28]

LCC	Purchasing Costs	Development Costs	Expenses for development Expenses for trade survey Expenses for experiment Expenses for constructional experiment Expenses for supplies in experiment Expenses for energy in experiment	Technical data costs Office costs Expenses for documents
		Design Costs	Expenses for design Expenses for rights	
		Construction and Setup Costs	Expenses for construction Expenses for product packaging Expenses for setting Expenses for making safety manual Expenses for the driver's training	
		Motor Driving Experimental Costs	Expenses for motor driving experiment	
	Maintenance Costs	Machine Driving Costs	Expenses for the drivers' wages Expenses for the fuel Expenses for water Expenses for supplies Expenses for materials and spares maintenance	Transportation costs Survey costs Any expenses in the office Expenses of documentary costs
		Safety Costs	Expenses for fixing Expenses for fixing energy Expenses for the safety driver's training	

Table 8 (cont.)

	Work Support Costs	Expenses Warehousing & Storage
		Expenses for safety materials
		Expenses for maintenance contracts
		Expenses for damage insurance
		Expenses for sales' wages
		Expenses for selling
		Expenses for quality assurance
	Depreciation	Disposing price
		Disposing costs

Life Cycle Costing Calculation

Life Cycle Costing is usually used to compare different system and equipment configurations. Some systems and equipment configurations have a high initial cost of purchase and setup, with low continuing running costs, while other such systems may be cheap to purchase and construct, but have high on-going costs. Therefore, these various expense and cost streams need to be reconciled to enable an economic analysis to be made.

Cost Profile Development and Evaluation [28]

This is the combination of economic knowledge and engineering knowledge being applied to the analysis and statements of all the expenses incurred within the system period such as capital cost, labor and installation costs, maintenance costs, running costs and replacement costs. The cost calculation can be achieved by applying Equation 36:

$$LCC = C_C + C_O + C_M + C_F - S \qquad (36)$$

Where C_C = Fixed costs (Baht)

C_O = Operating costs (Baht)

C_M = Maintenance costs (Baht)

C_F = Fuel or energy costs (Baht)

S = Disposal (Baht)

The System Costs (C)

The costs over time can be calculated in today's terms by applying a Net Present Value (NPV) formula. The net present value (NPV) is one methodology used to determine LCC; it is also used for capital budgeting where projects with the highest NPV exhaust the firm's fixed investment funding (Branson, 1979). NPV is the present value of an investment future cash flow (CF) minus the initial investment (I). For many LCCA, however, cash flows are often negative (outflows). Therefore, the smallest negative, which is the highest NPV, should be selected. The following formula is used to calculate NPV:

$$C = P\left[\frac{i(1+i)^n}{(1+i)^n - 1}\right] \qquad (37)$$

Where P = Recent costs or beginning costs (Baht)

i = Discount rate (%) per year

n = System working period (year)

When the per year cost is discounted back to present cost equivalent, it can be calculated by:

$$PW = F_n x \frac{(1+e)^n}{(1+i)^n} \qquad (38)$$

When $F_n x$ = Future costs or final costs (Baht)

e = Escalation of the expenses

Costs of the Decommissioning and Disposal

Ultimately the equipment will need to be decommissioned and disposed of. This activity may incur few costs, and the salvage value may even exceed the cost. On the other hand decommissioning and disposal may be a difficult task fraught with dangers, such as possible environmental pollution, demolition dangers and even site remediation. Therefore the costs of decommissioning and disposal are an essential inclusion in the Life Cycle Cost analysis. The now obsolete equipment may even have a salvage value and may be able to be sold, thus offsetting these last stage costs.

In the current research the net value or cost of disposal including salvage value was calculated 10% of the system setup costs (Purchasing Costs, as in Table 8), as suggested by [29].

The Insurance Costs for Hot Water Producing System

A survey of insurance costs for hot water systems of the type constructed in the current research project revealed that these are usually calculated as a percentage of the system setup costs (Purchasing Costs, as in Table 8). Most insurance quotes seemed to range up to 10%of the system setup costs, with insurance periods of between 1 and 5 years [29]. The Terms and Conditions of each insurance quote varied between companies.

In this research system insurance cost of 1% of the system setup costs.

Operating Cost

Each type of hot water producing system incurred varying running and maintenance costs over its life time. In the main these costs were for system cleaning and checking for material degeneration over time which would cause lower efficiency in hot water production and higher production cost. An important aspect of lowering efficiency is related to water quality and mineralization caused by 'hard' water with a high mineral content. This situation will vary from one geographical location to another. Therefore, overall, material degeneration needs to be checked at least once a year and rectified if necessary. The expenses included in this research for system maintenance in each type of system and equipment was ascertained in the surveys undertaken of organizations that manufacture and install each type of system.

Levelized Cost of Energy [30]

Levelized Cost of Energy (LCOE) is a stream of equal payments, normalized over the expected annual energy production over a predetermined financial life of the installation, that would allow a project owner to recover all costs, including financing and an assumed return on investment. LCOE has three basic cost components:

1. Fixed costs, such as initial investment
2. Variable costs, such as operations and maintenance (O&M) and fuel

3. Financing costs, such as cost of debt and cost of capital

The Levelized Cost of Energy (LCOE) allows alternative technologies to be compared when different scales of operation, different investment and operating time periods, or both, exist. For example, the LCOE could be used to compare the cost of energy generated by a renewable resource with that of a standard fossil fueled generating unit.

The LCOE is that cost that, if assigned to every unit of energy produced (or saved) by the system over the analysis period, will equal the LCC when discounted back to the base year. LCOE is recommended for use when ranking alternatives given a limited budget simply because the measure will provide a proper ordering of the alternatives, which may then be selected until the budget is expended. LCOE is not recommended when selecting among mutually exclusive alternatives because differing investment sizes are not considered (i.e. an investor will choose to invest more in an alternative with more favorable returns). This shortcoming may be corrected by applying LCOE to the incremental costs of the alternatives. The LCOE can be calculated using the following formula:

$$\sum_{n=1}^{N} \frac{Q_n \times LCOE}{(1+d)^n} = LCC \qquad (39)$$

Or

$$LCOE = \frac{LCC}{\sum_{n=1}^{N} \frac{Q_n}{(1+d)^n}} \qquad (40)$$

Where $LCOE$ = Levelized cost of energy

LCC = Life-cycle cost

Q_n = Energy output or saved in year n

d = Discount rate

N = Analysis period

n = Life time

Thus, the treatment of taxes in the LCC calculation will carry over to the LCOE. For example, the LCOE can be calculated for the same example as was provided in the Total Life-Cycle Cost subsection for the private investor seeking their after-tax cost.

Once the LCC is calculated, the LCOE can be figured in either current or constant dollars, regardless of the discount rates used to derive the LCC. The form of the LCOE will be determined by the form of the discount rate used in the denominator of the equation.

$$\sum_{n=1}^{N} \frac{Q_n}{(1+d)^n} \qquad (41)$$

It is important to note that if the system output (Q) or savings remain constant over time, the equation for LCOE can be reduced as follows:

$$LCOE = (\frac{LCC}{Q})(UCRF) \qquad (42)$$

Where LCC = Total life-cycle cost

Q = Annual energy output or saved

$UCRF$ = The uniform capital recovery factor, which is equal to

$$\frac{d(1+d)^N}{(1+d)^N - 1}$$

The shortcut methodology for estimating the before-tax-revenues-required LCOE requires the assumptions that the project not only will have constant output, but also constant O&M and no financing. If these assumptions can be made, the shortcut can be used with the application of the following formula:

$$LCOE = (\frac{1 \times FCR}{Q}) + (\frac{O\&M}{Q}) \qquad (43)$$

Where $LCOE$ = Levelized cost of energy

I = Initial investment

FCR = Fixed charge rate, in this case the before-tax revenues required FCR

Q = Annual output

$O\&M$ = Annual $O\&M$ and fuel costs for the plant.

In this research LCOE was calculated from Equation [39].

Literature Review

Kalogirou, S. [11] suggested that the present commercial solar absorber produced by electroplating, anodizing and by applying solar selective paints demonstrates the need for a commercial solar collector produced using the vacuum technique which is a production method with an outstandingly low price and is entirely harmless to the environment.

Abbas, A. [31] reported that there are 2 types of solar absorbing coatings; one coating with solar selective properties and the other without. Examples of coatings with solar selective properties are Black chrome, Black nickel, Black Copper and Black anodize. Black anodize is a type of aluminium oxide filled with pigment on the surface of the coating with solar absorptance value of 0.94 and thermal conduction value of 0.07. It is suggested that a good solar selective material must have certain properties: high solar absorptance (>0.90), low radiation (<0.20), large angle of acceptance, long life working under both normal environment temperatures and high temperatures, stability under adverse conditions and stability in humid conditions with durability and a long working lifespan as a solar collector, easily maintainable, and with a competitive price.

Antonaia, A., et al. [32] reported on the use of W-Al_2O_3 cermet to coat the receiver tube for working in high-temperature condition. This was tested in an annealing process at 580°C lasting for 2-30 days. It was found that the α was 93.70% and the ε was 9.30% (400 °C) and 13.20% (550 °C).

Wacklegard, E., et al. [33] repurified the annealing process of general solar absorbers and specially created absorbers in a laboratory at 350 °C and $5x10^{-3}$ Pa vacuum pressure. It was found that for the general absorbers, Tin_xO_y (Thermomax)and CrO_x-CrN_y (Sunselect), were stable in the process but for the created absorbers, Ni-NiO_x (Suntrip) and Al-AlN, were not stable in this process.

Al Shamilen, E. [34] used NiAl as the absorbing material for a solar water heating system (SWHS). This is a black coating material compound with NiAl 6% mass by mass. It has a higher resistance to natural corrosion and heats the water to a higher temperature than other water heating systems.

Culha, O., et al. [35] reported on NiAl coated onto 316L stainless material with High-Velocity Oxygen Fuel Process (HVOF). They studied the coating structure with X-ray diffraction (XRD) and Optical Microscopy (OM). It showed that the surface quality was high, with a high density with less oxidation and sponginess.

Sampath, S., et al. [36] analyzed the usage of NiAl with Ni-5 wt. %Al which is the percentage used in industry. Air Plasma Spraying (APS), Twin Wire-arc Spraying (TWA) and High-Velocity oxy-fuel (HVOF) methods were used. They observed that the surface tension from APS is higher than HVOF and TWA. Subsequently, Deshpande S., et al. [37] showed that HVOF required less oxidation and achieved better thermal conductivity on a similar test.

Tharamani, C. and Mayanna, S. [38] reported on Cu-Ni alloy coatings as solar selective material applied by electrode position on Cu foil, used on what was called a Hull Cell. Their results were that the solar absorptance of the Cu-Ni alloy is a high 0.94 with a low thermal conductivity value of 0.08. This is considered to be appropriate for use in domestic water heaters.

Katumba, G., et al. [39] the application of a solar selective material coating of nano-carbon mixed with SiO_2, ZnO and NiO in the matrix way by the Sol-gel technique, applied on aluminium film. For each element of the mix, radiation was measured as SO_2 - 30%, SiO_2 - 15% and NiO - 10%. The solar absorptance values were SiO_2 - 90, ZnO - 89 and 93% for NiO. The solar absorptance coating type NiO is therefore the best material for use as a solar receiver.

Ding, D., et al. [40] were successful in preparing new selective solar absorber materials which were Cu-$CuAl_2O_4$ hybrids in anodic aluminium oxide film (AAO) prepared by an electrochemical process. The solar absorptance (α) of the film is 0.923 and heat conduction (ε) is 0.06. The experiment, done under a high temperature of 200 ^{o}C with high humidity and condensation, over a period of 24 hours, indicated low solar absorptance. The spectral selectivity is 0.87/0.04. There is a suggestion that the condensation is a causal factor of the lower absorptance.

Wu, L., et al. [41] have reported about the preparation of selective solar selective material type CrN_kO/SiO_2 on Cu surface by DC reactive magnetron sputtering. The result of the study was found that the value of absorptance is 0.947, heat conduction is 0.05 at 80 °C, spectral selective α:ε, the stability is 0.930:0.073

after baking at 278 °C for 300 hours. However, the spectral selective $\alpha:\varepsilon$ is lower at 0.904:0.135 after baking at 278 °C for 600 hours.

Tesfamichael, T. and Wackelgard, E. [42, 43] also suggested that the solar absorptance of absorbers for thermal solar collectors is usually characterized at near normal angle of incidence. The solar absorptance is however a function of the angle of the incident light on the absorbers. The angular solar absorptance of commercial nickel pigmented aluminum oxide and sputtered nickel/nickel oxide solar selective absorbers were compared. The solar absorptance was calculated from experimental total reflectance spectra in the wavelength range 300–2500 nm for angles of incidence between 5 and 80°. It was found that the solar absorptance at higher angles of incidence is lower for the sputtered nickel/nickel oxide than for the nickel pigmented aluminum oxide coating. This is explained with theoretical calculations based on microstructure models of the two types of coatings. The nickel pigmented aluminum oxide with a double-layer structure of its coating has an enhanced higher angle of solar absorptance due to thin film interference effects which cannot be achieved from a graded-index thin film coatings as is the case for the sputtered nickel/nickel oxide absorber. When the absorbers were covered by glass, as is common for most solar collectors, a negligible difference in optical performance at the higher angles of incidence was obtained. These results were consistent with a theoretical calculation by use of an incident angle modifier model.

Tesfamichael, T. and Wackelgard, E. [43] reported on the optical characterization of solar absorbers for thermal solar collectors performed by measuring the spectral reflectance at near-normal angles of incidence and using those measurements of reflectance to calculate the solar absorptance of the thermal solar collectors. The solar absorptance is a function of the angle of incidence of the light impinging on the absorber. The total reflectance of two types of commercial solar-selective absorbers; nickel-pigmented anodized aluminum, and sputtered nickel/nickel oxide coated aluminum, were measured at angles of incidence from 5° to 80° in the wavelength range 300–2500 nm by use of an integrating sphere. From these measurements the angular integrated solar absorptance is determined. Their experimental data was compared with theoretical calculations, and it was found that

optical thin-film interference effects can explain the significant difference in solar absorptance at higher angles for the two types of absorbers.

Wazwaz, A., et al. [44] studied the diffused reflectance measurements and Kubelka–Munk values of alumina layers and nickel content. The effects of the alumina layer and the nickel content on the optical properties of the selective absorber were discussed. For the aluminium alloy substrate, the diffused reflectance decreased by 85.25 – 91.42% (±0.01%). The emissivity increased by a factor of 252.50 – 624.50 (±0.01). The average absorptivity increased by a factor of 4.99 – 5.35 (±0.01). The average thermal efficiency increased by a factor of 4.51 – 4.80 (±0.01). A sample with nickel content 60 $\mu g/cm^2$ was found to have optimum optical properties as a good selective absorber. It has the highest solar selectivity by the two measurements. The range of hemispherical solar selectivity is 4.22 – 8.36 (±0.01); while for average solar selectivity is 7.410 – 17.456 (±0.001). The thermal efficiency is increased by increasing the nickel content to a certain limit (60 $\mu g/cm^2$), however it then decreased after this limit due to the increase in the emissivity. Also, the total hemispherical optical properties are in accordance with the averaged optical properties obtained from diffused reflectance measurements over the solar range. The nickel-pigmented aluminium oxide is one of the best selective absorbers for the photo thermal conversion and it is of high durability.

Granam, L. Morrison [45] studied the status of the international solar energy hot water market and the problem of prices in the solar energy hot water machine trade. He collected the factors that are concerned with the solar energy hot water producing market from data used for trade planning and new product development in Australia and also to be used for discussion by the International Energy Organization Project.

Michael, G., et al. [46] reported that EuroTrough parabolic trough collector models ET100 and ET150, with the ratio of reflective area to concentration ratio of 82:1, can achieve temperatures greater than 500 °C. The ET100 and ET150 structure geometries include a wind channel and use finite element method validation. They are compatible with the standard receiver tubes and mirror panels generally available in the market. The collector modules were fully qualified, in 2000-2002, with a synthetic heat transfer fluid for 395 °C operation. This was performed at the Plataforma Solar de

Almería (PSA) center for the exploration of solar energy, situated in the Province of Almería, Spain, with independent performance test certificates from independent research laboratories. Solar field cost reduction in the order of 14% is anticipated due to weight reduction and collector extension to 150 meters. A 50 MW solar power plant with 549,000 m^2 of EuroTrough collectors and 9h-thermal storage is projected to be constructed in southern Spain.

Valan, A.A. and Sornakumar, T. [47] constructed and tested the strengthening the parabolic trough with fiberglass. In the design process, the rim angle that was used was 90° and the thickness of the tube was 7 mm. There was an effective test by ASHRAE Standard 93 and it was found that there was 0.0066 rad deviation from the standard. As a result, parabolic trough construction by fiberglass can be considered practicable. As well, the cost of materials is cheaper than alternatives [23]

Kumar, K.R. and Reddy, K.S. [48] analyzed the characteristics of heat conduction of the porous discs in the receiver tube by 3-D numerical analysis. The test results indicated that the porous discs encouraged heat conduction. However, an increase in the rate of pressure drop occurred. This means that the heat transfer in a receiver tube will be increased when there is an increase in the area of heat transfer, the range of the thermal conduction of the tube and in the turbulence flow of the fluid. The highest coefficient of heat transfer around the top of the tube containing the porous disc occurred with the parameter values $H = 0.5d_i$, $w = d_i$, and rim angle of 30°. The Nusselt number increased by 64.2 % when compared with normal rays at Reynolds number 31,845, and a pressure drop of 475 Pa.

In their 2003 study of the economic feasibility of an investment in hot water production from an integrated solar energy system, Krit, K. and Thanwa, J. [49], they concluded that the project was economically highly feasible. The study was conducted at Klang Hospital in Rayong Province, indicating a substantial project. The purpose of the project was to save cost as well as be of environmental benefit in terms of decreasing air pollution. An economic feasibility study of the project was conducted employing data collected from the monthly operations of the solar heating system and projecting these over a 16 year project life, with an 8% a discount rate. The findings were that the project was highly feasible with Net Present Value (NPV) of just over 1,070,000 Baht, a Benefit-Cost Ratio (BCR) of 2.34 and an Internal Rate of Return

(IRR) of 31.15%. Sensitivity analysis of the various benefit and cost items also confirmed the feasibility.

The extent of previous published research indicates a wide variety of solar absorber materials used, and many types of single type and multi-type solar collectors necessary to meet the requirements of operating in a wide range of temperatures. There have been many different designs of solar collectors developed to reduce the cost of heating water in a range of uses, and to minimize heat loss and improve the efficiency of the solar collector. Many techniques for coating the solar coating material on substrate film have been utilized to improve solar and thermal efficiency. These techniques, however, are often sophisticated and based on complex technologies with a high cost. Some of these coating materials are harmful to the environment, both in the production of the material and the on-going use of the material; a problem given more recognition and consideration in recent times.

This, therefore, is the motivation and driving intention of the current research; to identify, characterize and apply a low cost, easy to use and environmentally friendly solar selective material, particularly appropriate for water heating in both domestic situations and larger industrial situations. The material selected for this research is an adaptation of anodized aluminium to be used as a solar selective film on an aluminium parabolic trough collectors.

CHAPTER III

RESEARCH METHODOLOGY

The objectives of this experimental research were to study the specific characteristics of and adaptability of anodized aluminum used as a solar absorber in a parabolic trough collector. There are 5 main steps of the dissertation methodology (Figure 10) as follows;

1. Preparation of Sn-Al2O3 film on the aluminium tube grade 6063 by an anodizing method.
2. Identification of the characteristics of anodized aluminium tubing.
3. Design and fabrication of a parabolic trough collector prototype.
4. Evaluate the thermal efficiency of the parabolic trough collector system.
5. Conduct an economic assessment of the use of anodized aluminium tubing as a solar receiver.

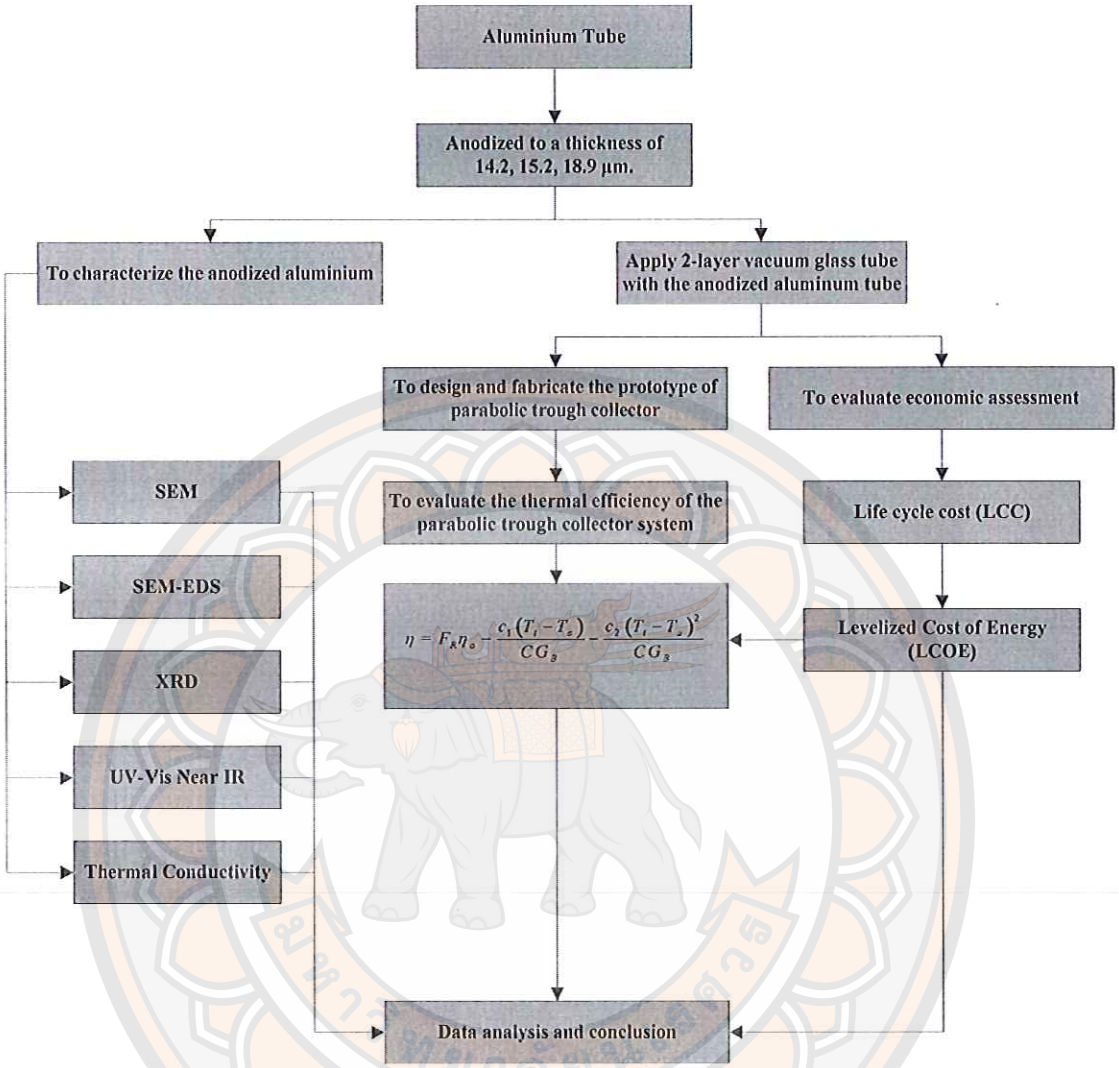

Figure 10 Flow chart of dissertation methodology

Preparation of Sn-Al_2O_3 by Anodizing method

Aluminium is an efficient conductor of heat and has a high heat transfer rate. As such, it is an appropriate material to investigate in this research. Aluminium alloy 6063 is a medium strength alloy commonly referred as an architectural alloy. It is generally used in intricate extrusions. It has a good surface finish, and has a high resistance to corrosion, making it well suited to being welded. As well, it can be easily anodized. Its melting point is 600°C with a Modulus of Elasticity equal to 69.5 Gpa and, being an aluminium alloy, has a Thermal Conductivity value of 200 W/m.K. The Parabolic Trough Collector constructed and used for the tests in this research was

constructed with an aluminum alloy 6063 tube of diameter 2.54×10^{-2} m. and 2 m. long considered sufficiently strong with pressure resistance capability so as not to deform under high temperature or pressure. When the aluminum tube is anodized, coating it with a film of Aluminium Oxide (Al_2O_3), which has a porous surface, reducing its effectiveness as a solar absorber. Further anodizing of the surface of the film of Aluminium Oxide (Al_2O_3) with Sn-Al_20_3 fills the pores with tin creating a film surface that is an efficient solar absorber. This was the additional processing activity undertaken and tested in this research.

Anodization is a popular technology, which is cheap and is a usual industrial process in Thailand. The usual processes of anodization, which were followed in this research, are: The Al substrates are degreased by commercial solution, rinsed in deionized (DI) water and then etched by NaOH solution. The Al substrates are then immersed in a sulfuric acid solution to achieve a chemical neutral surface. All these steps can be carried out under ambient temperatures, thereby requiring no special environmental conditions. In the anodization process, the fabrication of the Aluminium Oxide (Al_2O_3) film on the aluminium substrate is achieved by anodic oxidation in a sulfuric acid solution (165 g/L) applying a direct current with 1,000 A electrical density and a constant potential ranged from 15 to 17 V at 20±1 °C. The anodization time is determined by the thickness of the Al_2O_3 film required. In this process the aluminium substrate is the anode (+) electrode, and a lead plate immersed in the sulfuric acid solution is the cathode (-) electrode. Under suitable conditions the Al_2O_3 film is formed as a translucent coating on the surface of Al substrate. Then, in the process being carried out in our research, the sample tubing was rinsed in DI water for 10 s.

In the experimental process in this research, the anodized tubing, with the Al_2O_3 surface film, was then further treated with Sn pigmented aluminium (Sn-Al_2O_3) by electrochemical deposition in a coloring tank containing a commercial tin sulfide (SnS) solution and buffered to a less acidic state in DI water at 20±1 °C. The pigmented Sn content laid down on the porous surface of the Al_2O_3 film filled, resulting in a shiny, smooth, non-porous surface. After about 30 minutes in the tin sulfide (SnS) solution, the sample was removed and rinsed in hot water in the hot water tank at 50 – 60 °C for a further 30 minutes. This sealed the porous Al_2O_3 film.

As a final step, the sample was cooled and dried at room temperature. These anodization and Sn pigmentation processes were carried out at Bangpoo Coating Co., Ltd., Samutprakarn, Thailand.

Figure 11 Anodized Aluminium tube Characteristics of anodized aluminium

The Sn-Al_2O_3 sample was characterized by different methods. The phase, morphology and reflectance (R) of the sample were determined by X-ray diffraction (XRD) using Philips X'Pert PANalytical X-ray diffractometer with Cu-K_α radiation in the 2θ range of 10 - 100°, Scanning Electron Microscope (SEM, JSM-5910 JEOL) operating at 12 kV equipped with energy dispersive X-ray (EDS) analyzer and Ultraviolet-visible-near infrared spectrophotometer (Shimadzu UV-3101PC) in the wavelength of 300-2500 nm. Details are as follows.

X-ray diffraction Analysis

X-rays are the electromagnetic radiation which the typical photon energies are in the range of 100 eV - 100 keV. For the diffraction applications, there are only short wavelength x-rays in the range of a few angstroms to 0.1 angstrom (1 - 120 keV) used. They are ideally appropriate for probing the structural arrangement of the atoms and molecules within a wide range of the materials because the x-rays' wavelength is comparable to the size of atoms. The energetic x-rays are able infiltrate deeply into the materials and also able to provide the information of the bulk structure. The X-rays generally are created by either synchrotron radiation or x-ray tubes. In the tube, the primary x-ray source used in laboratory x-ray instruments, x-rays are created when a

focused electron beam across a high voltage field attacks a stationary. As electrons are in with the atoms in the target and slow down, a continuous spectrum of x-rays, therefore, are emitted. These are termed Bremsstrahlung radiation. Also, high-energy electrons eject the core electrons in the atoms through the process of ionization. An x-ray photon with energy characteristic of the target material will be emitted when the electron from higher energy orbital fills the shell. Common targets in x-ray tubes are Cu and Mo which emits 8 keV and 14 keV x-rays with corresponding wavelengths at 1.54 Å and 0.8 Å, respectively [50].

X-rays interact with electrons in atoms originally when collide and some photons from the incident beam are diverge from the original. If the wavelength the scattered x-rays is not changed, the process called elastic scattering where only the momentum transfer will replace. These scattered X-rays are measured in order to find out the information about the material due to the fact that they have the information about the electron distribution in materials. Diverged waves from the different atoms are able to be concerned with each other and the derivable intensity distribution will be strongly modulated. If the atoms are ordered in a periodic fashion, the diverged waves will include sharp interference maxima with the same symmetry as in the distribution of atoms. So, measuring the diffraction pattern will be allowed to estimate the distribution of the atoms in a material. When the certain geometric essentials are found, the X-rays diverged from a crystalline solid will constructively interfere producing a diffracted beam. In 1912, W. L. Bragg suggested the relation which elucidates the condition for constructive interference.

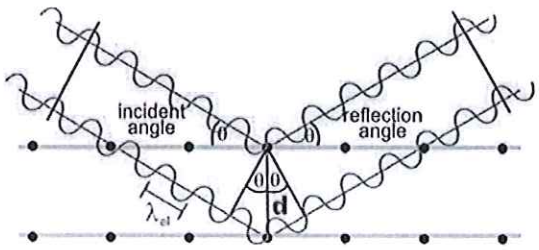

Figure 12 Illustration of Bragg's law [51]

From Figure 12, it gets obvious why the angle between incident beam and diffracted beam is 2θ.

$$n\lambda = 2d\sin\theta \qquad (43)$$

Equation 43 is 'Bragg equation', where n is the order of diffraction, λ is the wavelength, d is the inter-planar spacing; and θ is the scattering angle. The distance between similar atomic flies in a crystal that is d spacing and measured in angstroms. The diffraction angle is called θ angle and measured in degrees. For practical reasons, the diffractometer measures an angle twice of the θ angle [52].

In this study, XRD are used in order to find the phase. The XRD data introduced here are carried out on a Philips X'Pert PANalytical X-ray diffractometer with Cu-K_α radiation in the 2θ range of 10 - 100°.

Scanning electron microscope (SEM)

Scanning electron microscope is one of the useful tools for the study of the sample's surface because of its better resolution than the optical microscope. It applies electrons that emitted from tungsten or Lanthanum hexaboride (LaB6) thermionic emitters in order to visualize the sample's surface. The filament is resistively heated by a current for achieving the temperature to be between 2000-2700 K. As a result, an emission of thermionic electrons from the tip over an area is about 100 μm x 150 μm. The electron gun generates electrons and accelerates them to energy in the range 0.1-30 keV as in the sample [53]. The lenses focus the electron beam on to the sample where it attaches with the sample to a depth of approximately 1 μm. Figure 13 shows the components of a scanning electron microscope [54].

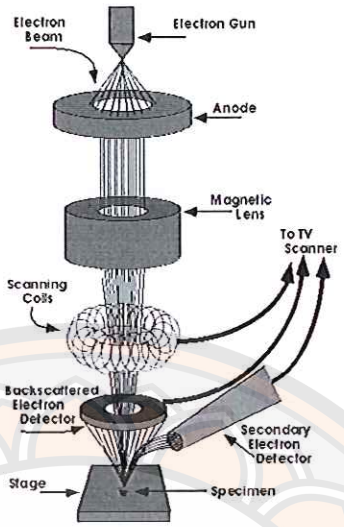

Figure 13 The components of a scanning electron microscope

When the electron beam hits on the specimen, many types of signals are generated and the signals are able to be displayed as an image. Secondary electrons (SE) and backscattered electrons (BSE) are the two signals that are most frequently used to generate SEM images. Most of the electrons are scattered around the large angles (from 0^{o} to 180^{o}) when the electrons interact with the positively charged nucleus. The scattered electrons which are generally called 'backscattered electrons or BSE are used in order to image the SEM. Some electrons are scattered in-elastically because of the loss in kinetic energy within the interaction with orbital shell electrons. The incident electrons will knock off the loosely bound conduction electrons out of the sample. These are secondary electrons (SE) with backscattered electrons which are generally used in order to image topographical SEM. Both signals will be collected when a positive voltage is applied to the collector screen in front of detector. When a negative voltage is applied on the collector screen, there is only BSE signal captured since the low energy SE is repelled. After that, electrons captured by the scintillator/photomultiplier are increased and used to image the SEM.

When the electron beam knocks off the inner shell electron, the electron from higher energy levels will move to lower energy levels resulting in the emission of Auger electrons. These electrons are applied to draw information of the chemical

composition of the sample. This technique is called "Auger electron spectroscopy or AES". The emission can also be in the form of photons or X-ray photons with its high energy. The photons are used for the compositional analysis of the sample. This technique is recognized as an energy dispersive analysis (EDS) and also used to study about the elemental composition of the sample. Figure 14 show the SEM that use for this research.

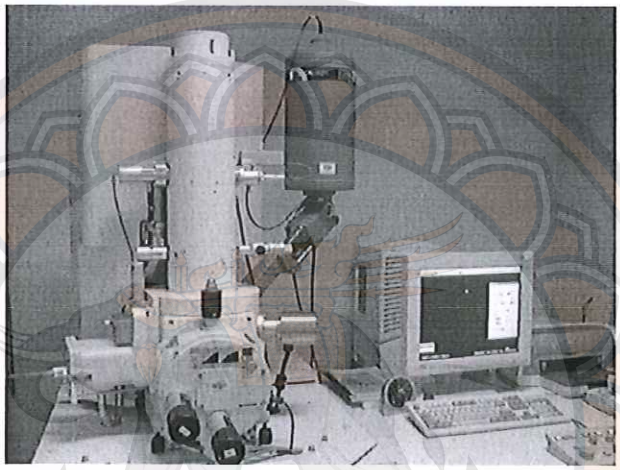

Figure 14 Scanning Electron Microscope (SEM, JSM-5910 JEOL) equipped with energy dispersive spectrometry (EDS) analyzer

Ultraviolet-visible-near infrared spectrophotometer

Absorption spectroscopy in the different regions of electromagnetic spectrum has been an important tool to the analyst since a long time [55]. Any molecular system possesses three types of energy namely electronic (E_{ele}), vibration (E_{vib}) and rotational (E_{rot}) with decreasing magnitude in same order for a system. Absorption of energy leads to transition of electron from ground state to excited state. The absorption peak thus obtained is broad, smooth and never very sharp due to the fact that the electronic absorption is accompanied with a corresponding change in the vibration and rotational energies as well. The relationship between the energy absorbed in an electronic transition and the frequency, ν, wavelength, λ and wavelength number, $-\nu$ of the radiation producing the transition is

$$\Delta E = h\nu = \frac{hc}{\lambda} = h \cdot -\nu \cdot c \qquad (44)$$

where, h is Planck's constant, c is the velocity of light and ΔE is the energy absorbed in an electronic transition in a mole h cure from a low-energy state (ground state) to a high energy state (excited state). The position of absorption maxima for a molecule depends on the difference in the energy of the ground state level to that of excited state; larger the difference between the energies, higher is the frequency of absorption and thus smaller will be the wavelength. Absorption band shows two important characteristic; position of the band which depends on the energy difference between electronic level and intensity which depends on the interaction between the radiation and electronic system as well as on the energy difference between the ground and excited state. A convenient expression, which relates the absorbance with the path length that the radiation travels within the system and the concentration of the species, can be derived from the Lambert-Beer law and is given as,

$$A = a \cdot b \cdot c \qquad (45)$$

where A is measured absorbance, a is the absorptivity, b is the path length and c is the analysis concentration.

In the presented work, the near-normal spectral reflectance of the samples was measured in the 300-2,500 nm. wavelength range with UV-vis-NIR spectrophotometer. The solar absorptance (α) of the Sn-Al_2O_3 surface is defined as a fraction of radiation incident on the surface of the material that is absorbed. It is a function of both the incident spectrum, $I_s(\lambda)$ and the reflection function of the material, $R(\lambda)$, and is given by [56, 57]

$$\alpha = \frac{\int_{0.3\mu m}^{2.5\mu m} I_s(\lambda)(1 - R(\lambda))d\lambda}{\int_{0.3\mu m}^{2.5\mu m} I_s(\lambda)d\lambda} \qquad (46)$$

Where $R(\lambda)$ is the measured spectral reflectance of the coating at a specific wavelength of 300-2,500 nm, and $I_s(\lambda)$ is the solar spectral irradiance at air mass AM 1.5. These measurements were done on Shimadzu UV-3101PC show in Figure 15.

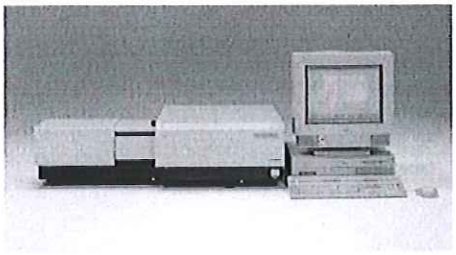

Figure 15 Ultraviolet-visible-near infrared spectrophotometer (Shimadzu UV-3101PC)

Sourch: http://www.speciation.net/Database/Instruments/Shimadzu-Europe/UV3101PC-;i1302.

Thermal Conductivity

Measuring heat conductivity the back side of a flat in a laser flash experiment, the solid sample is heated with a short laser pulse. This heat energy input is spread all over the sample body. It is also leading to a temperature increase on the front side of the sample. This temperature rising is monitored as a function of time with an infrared detector (InSb-detector, liquid nitrogen cooled). The mathematical modeling of this temperature rise leads to the determination of the temperature diffusivity (α [mm^2/s]). The specific heat capacity (C_p [J/g.K]) is now able to be determined by comparing the final temperature rise of the sample under the investigation with a standard sample which is measured under the same conditions. The thermal diffusivity (α) of a medium is the thermophysical property that defines the speed of heat propagation from conduction during temperature's changes with time. It can be said that the higher the thermal diffusivity, the faster the heat propagation. The thermal diffusivity is the thermal conductivity divided by density and specific heat capacity at constant pressure [58]. It measures the ability of a material to conduct thermal energy relative to its ability to store thermal energy. Thermal diffusivity is usually denoted by the thermal conductivity (λ), specific heat (C_p), density (ρ) and as follow :

$$\alpha = \frac{\lambda}{\rho C_p} \qquad (47)$$

The thermal diffusivity affects any conductive transient heat transfer process within the medium according to all above reasons. There is the dimension length^2/time and the expression in the unit m^2/s.

It is found that the flash method is the most popular method for measuring thermal diffusivity due to its speed while providing the values with excellent accuracy and reproducibility. After stabilizing the sample at a desired temperature T_0, a nearly instantaneous pulse of energy (usually laser or other discharge source) is deposited on its front face, and the temperature rise on the back face of the sample is recorded as a function of time (Figure 16). Later, the thermal diffusivity is defined from this thermogram. Parker [59] has originally suggested the method that assumes an isotropic and adiabatic sample (no heat loss). The thermal diffusivity is defined from the thickness (L) of the sample and the time ($t_{1/2}$). The thermogram takes to reach half of the maximal temperature rise:

$$\alpha = 0.1338\frac{L^2}{t_{1/2}} \qquad (48)$$

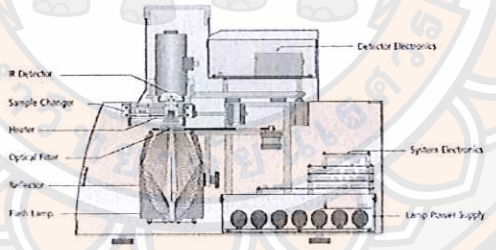

Figure 16 Diagram of laser flash analyzer model LFA 447 NanoFlash-A

Sourch: http://carleton.columbia.edu/netzsch-nanoflash-thermal-diffusivity-analyzer

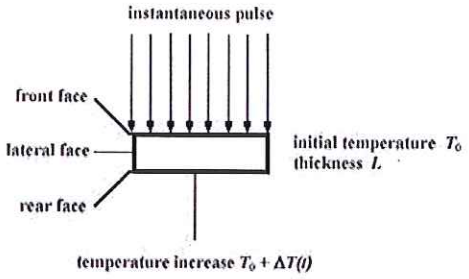

Figure 17 Diagram of laser flash analyzer model LFA 447 NanoFlash-B

Sourch: http://www.azom.com/article.aspx?ArticleID=5613

As this method assumes the ideal conditions of adiabatic sample and the instantaneous pulse heating, it is rather limited in applicability. In order to make it more suitable for the experimental conditions, other methods have been presented over the years which explain about the heat losses, finite pulse duration, non-uniform pulse heating, and composite (non-homogeneous) structures.

Sample preparation method for analytical process phase, morphology

1. X-Ray Diffraction (XRD)

2. Prepare a sample of 1 x 1 square centimeters as shown in Figure 17 (a) Tested at Department of Physics, Faculty of Science, Chiang Mai University.

3. Scanning Electron Microscope (SEM)

4. Prepare a sample formed by Bakelite and polish its sectional surface as shown in Figure 17 (b) Test the sample at Science and Technology Service Center, Faculty of Science, Chiang Mai University (STSC-CMU).

5. Scanning Electron Microscope and Energy Dispersive Spectroscopy (SEM-EDS)

6. Prepare a sample formed by Bakelite and polish its sectional surface as shown in Figure 17 (b) Test the sample at Science and Technology Service Center, Faculty of Science, Chiang Mai University (STSC-CMU).

7. Ultraviolet-Visible-Near Infrared Spectrometer

8. Send the sample of 1 x 1 square centimeter, as shown in Figure 17 (a) to be tested at Department of Chemistry, Faculty of Science, Khonkaen University.

9. Thermal conductivity

10. Send the sample of 1.2 x 1.2 square centimeter, as shown in Figure 17 (c) to be tested at Department of Science Service, Ministry of Science and Technology of Thailand.

Figure 18 The sample preparation for analytical process phase, morphology, the sample size 1 x 1 square centimeter

Figure 19 The sample preparation for analytical process phase, morphology, the sample formed by Bakelite

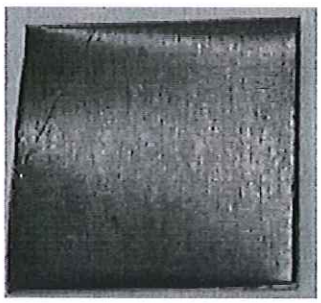

Figure 20 The sample preparation for analytical process phase, morphology, the sample size 1.2 x 1.2 square centimeter

Designing and creating processes of Parabolic through solar collector

Details are as follows:

Parabolic trough collector design and fabrication

There are several parameters for design the parabolic trough receiver. In this research, some parameters are fixed as shown in Table 9. The rim angle is chosen 90°, due to highest intensity of solar radiation on parabolic trough collector. In case of aperture range of parabolic trough collector, it is 1.8 m, due to the suitable size and reducing aluminium bend during install in parabolic trough prototype. The dimensions of the aluminium tube are 2.54×10^{-2} m. outer diameters, which is commercial size in the market, light weight, widely used and cheap. The tube length is 2 m, which is unable to be bended during the test.

Table 9 The specified parameters for calculation and design a prototype PCT

Parameter	value
Collector dimensions	2 m x 1.8 m
Rim angle	90^o
Absorber diameter, D	0.0254 m
Aperture of the parabola, W_a	1.8 m

According to the set parameters, the concentration ratio (C) can be calculated by Equation 11:

$$C = \frac{W_a}{\pi D}$$

Therefore, the C is 22.784. The focus point can be found by the Equation 10:

$$W_a = 4ftan\left(\frac{\varphi_r}{2}\right)$$

Therefore, focus point (f) is 0.45 meter. Then, the f is used to find r_r by the Equation:

$$r_r = \frac{2f}{1+\cos(\varphi_r)}$$

As a result, r_r is 0.9 meter. It can be concluded in Figure 18, according to the above calculations,

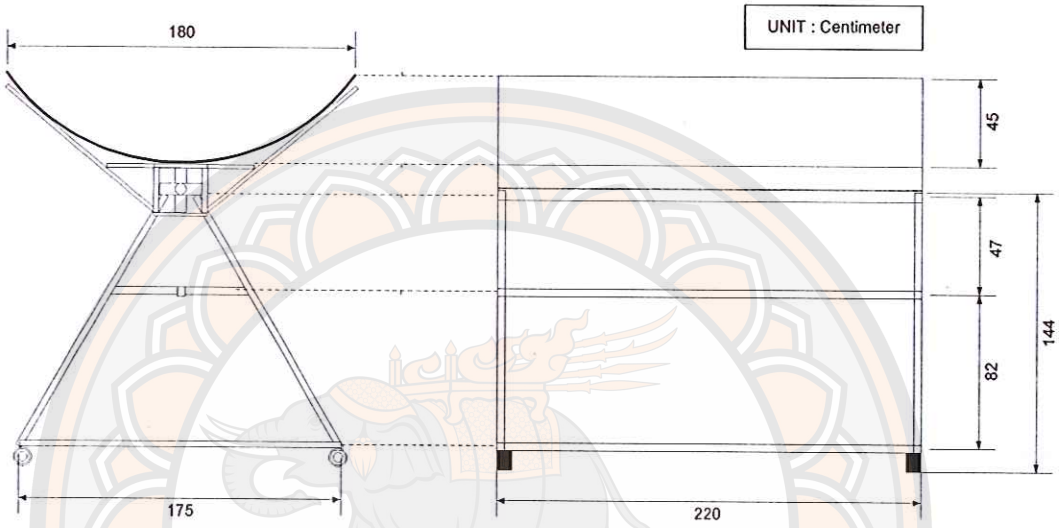

Figure 21 Cross section of the prototype of PTC after calculatingly design

Creating processes of parabolic trough solar collector

Details are as follows:

1. Build parabolic structure from steel as same as in the design.

2. Install sun monitoring set with monitoring system which is based on the Sun movement while the sun angle is at 180 degree in horizontal level. Furthermore, using sunset and sunrise data from the Thai Astronomical Society to find the duration of the sun on the sky so that we will know its locations during times and create movement control system of parabolic troughs by motor gear as the controller and the monitor through Micro controller. These help increase efficiency and accuracy of the system.

3. Attach reflectors made from Polyethylene terephthalate (PET) with 92% of reflection capacity on the solar reflection areas. The attachment must perfectly flat on the floor so that the solar will mostly be reflected to the focus of the receiver.

4. Install parabolic troughs solar collector at the open area without cast shadow as North-South Horizontal axis.

Evaluate the thermal efficiency of the parabolic trough collector system.

The formalization of collector test procedures is a recent development. Many new designs appeared in the commercial marketplace. Standard tests were required to provide operating data, especially with respect to energy absorption, heat loss, effects of incidence angle and heat capacity. In the U. S. the National Bureau of Standards devised a test procedure that was modified by the American Society of Heating, Refrigerating and Air-conditioning Engineers (ASHRAE). This eventually became the ASHRAE Standard 93-1986. In this research, the diagram of thermal efficiency test shown in Figure 19. Water inlet temperature in solar collector was control as during the test, temperature of the water both inlet temperature, outlet temperature, and ambient temperature was taken, the direct solar radiation was measured by Pyrheliometer, and wind speed was measured by Anemometer.

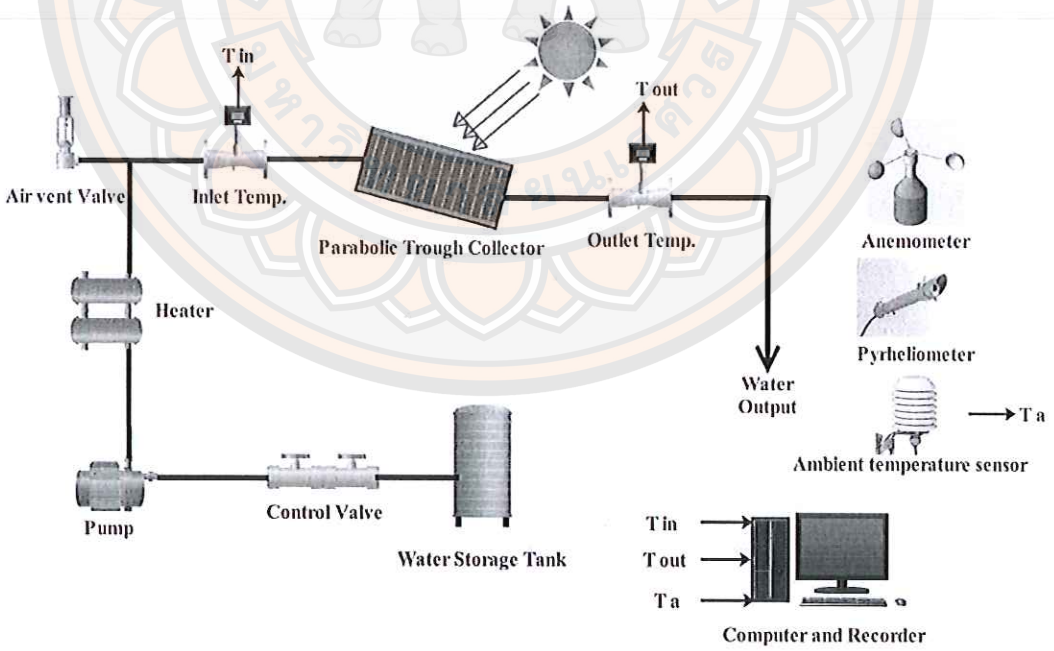

Figure 22 The diagram of thermal efficiency test

Procedures of Thermal efficiency testing of solar collector, as following details.

1. Choose a test in accordance to the standard of opened water system, therefore, storage tank was needed.

2. Turn water pump on in order to control the flow rate and to ventilate all tubes and joints in the system. The outlet water must not have air bubble with it, otherwise, the executor must ventilate the system until there's no air in it.

3. The mass flow rate is to be set according to collector area, which equals $0.02 kg/s.m^2$.

4. Turn on pump and control the mass flow rate in accordance to collector area.

5. Turn on the heater to stabilize temperature of the water throughout the test. The temperature will be set from 40 °C to 70 °C. The temperature increase rate is 10 °C a time.

6. When the temperature and flow rate are stable, executor can begin the test. During the parabolic test, it's necessary that the parabolic faces the sun and to do so throughout the test in order for the sun light to be at the focus at all times.

7. To collect data for analyzing, start at 40 °C. During the test, data regarding temperature of the water both inlet temperature, outlet temperature, solar radiation, and ambient temperature should have been collected for at least for 15 minutes. Then increase the temperature for 10 °C until the inlet temperature becomes 70 °C.

8. Retest the test until 3 sets of data are collected.

9. Analysis the 3 sets of data and terminate errors. Create a relation graph between $(T_i - T_a)/G_B$ and η for parabolic trough collector.

Perform an economic assessment of the use of anodized aluminium

An economic assessment of the use of anodized aluminium using the Life Cycle Cost (LCC) and the Levelized Cost of Energy (LCOE) calculations, were evaluated.

The Cost and Benefit data are shown in Tables 10 and 11

As extensively discussed elsewhere, the cost of a project has 2 parts: Initial investment and setup costs and operating and maintenance costs.

The cost analysis included the three system configurations which were constructed with 14.1, 15.2 and 18.9 μm.

Initial investment and setup costs

1. Cost of the glass vacuum tube
2. Cost of the anodized coating material
3. Cost of the aluminium tube
4. Cost of supporting structure of the parabolic trough collector
5. Cost of control system

The initial investment costs of the project (Year 0) were 61,260 Baht (14.1 μm), 61,265 Baht (15.2 μm) and 61,265 Baht (18.9 μm). This data is shown in Tables 10 and 11.

Operating and maintenance cost (0.5% of initial investment cost)

The operating and maintenance costs for the 16 years of expected operating life were 2,562 Baht each for all three configurations. These costs included the projected annual electricity cost, maintenance cost, replacement parts cost and miscellaneous operating costs.

For Years 1-15 the projected costs were discounted back to present value by a NPV calculation formula with a discount rate of 8.37% and expected inflation rate of 3.7%.

Estimates of Benefits from the project included the salvage value (10% of investment cost) were 1,832.36 Baht (14.1 μm), 1,832.52 Baht (15.2 μm) and 1,832.52 Baht (18.9 μm). The savings in the cost of energy inputs were calculated by estimating the electricity cost for an electric hot water system of similar hot water production capacity. The annual heat production of the various systems were estimated at 3,181.91 MJ (14.2 μm), 3,926.19 MJ (15.2 μm) and 4,111.01 MJ (18.9 μm). Electric hot water systems of comparative annual heat production consumed 833.09 kWh., 1,090.60 kWh. and 1,141.94 kWh. of electricity, respectively. If costed at 3.93 Baht per unit of electricity consumed, the annual electricity costs saved were therefore 3,470.54 Baht, 4,286.06 Baht and 4,487.82 Baht, for the three solar configurations respectively.

Table 10 Investment cost and benefit of project

Details	Value
Investment costs	
Cost of glass vacuum tube	15,000 Baht
Cost of control system	22,790 Baht
Cost of aluminium tube	200 Baht
Cost of structure of the parabolic trough collector	19,250 Baht
Cost of anodized coat	
14.2 μm	1,060 Baht
15.2 μm	1,075 Baht
18.9 μm	1,075 Baht
Operating and Maintenance cost	
14.2 μm	2,562 Baht
15.2 μm	2,562 Baht
18.9 μm	2,562 Baht
Benefits	
Energy produce	
14.2 μm	13,257.97 MJ
15.2 μm	16,359.13 MJ
18.9 μm	17,129.21 MJ
Savage value	
14.2 μm	1,832.36 Baht
15.2 μm	1,832.52 Baht
18.9 μm	1,832.52 Baht

Table 11 The parameter of calculation

Parameter	Symbol	Thickness (μm)			Unit
		14.2	15.1	18.9	Baht
Investment and setup costs	C_C	61,260	61,265	61,265	Baht
Operating and maintenance cost	C_n	2,562	2,562	2,562	Baht
Salvage value	SV	1,832.36	1,832.52	1,832.52	Baht
The annual heat production	E_n	883.86	1,090.60	1,141.94	kWh/Year
Discount rate	i		8.37		%
Life time	n		16		Year
Number of Years	N		15		Year

Table 12 The parameter of annual energy calculation

Parameter	Symbol	Value	Unit
Beam radiation	G_B	350	W/m^2
Ambient temperature	T_a	30	°C
Water inlet temperature	T_i	40	°C
Water outlet temperature	T_o	70	°C
Average Solar beam radiation in Thailand	E	1,349	$kWh/m^2 \cdot Year$

Table 12 shows the parameters and parameter values used to calculate the annual energy output of the experimental parabolic trough collector with an anodized aluminium tube with thickness of 18.9 μm as the solar absorber. These parameters and values are used in the following equation:

The thermal efficiency equation

$$\eta = 0.25 - 0.42\left(\frac{(T_i - T_a)}{G_B}\right) - 0.01\left(\frac{(T_i - T_a)}{G_B}\right)^2$$

Calculation with parameters from Table 12

$$\eta = 0.25 - 0.42\left(\frac{40-30}{350}\right) - 0.01\left(\frac{40-30}{350}\right)^2$$

Calculated thermal efficiency η = 0.23

Annual energy calculations = 0.23×E kWh/m^2·Year

= 0.23×1,349 kWh/m^2·Year

= 317.20 kWh/m^2·Year

Table 13 summarizes the annual energy output for each thickness of the parabolic trough collector used in the experimental tests.

Table 13 The annual energy of the parabolic trough collector of three thicknesses

Levels of thickness (μm)	Annual Energy Yield (kWh/m^2)	Annual Energy Yield (kWh)	Annual Energy Yield (MJ)
14.2	245.51	883.86	3,181.91
15.2	302.94	1,090.60	3,926.19
18.9	317.20	1,141.94	4,111.01

CHAPTER IV

RESULTS AND DISCUSSION

There are five sections in this chapter. The first section discusses the application of a film of Sn-Al2O3 over the Al2O3 film, using the anodizing process. The second section shows the characteristics of Sn-Al2O3 anodized aluminium. The third section shows the design and fabrication of the parabolic trough collector prototype. The fourth section the thermal efficiency of the parabolic trough collector system is evaluated, and lastly, an economic assessment of the use of Sn-Al2O3 anodized aluminium is presented.

Surface Characteristics

Figure 20 shows the surface of the anodized aluminium tube coated with the Sn-Al2O3 film. The surface is a dark black color and has a matt surface. The tests showed that this surface is able to better absorb solar energy when used as the solar absorber. The results of the tests indicated that adding Sn as the coloring material and filling the porous surface of the aluminium oxide film, results in the aluminium oxide film taking on the properties necessary to be an effective solar selective material. Therefore it can be stated that the surface morphology of a black or diffusely scattering surface is the primary determinant of its complex optical properties. This was the case in all three thicknesses of the tube being tested.

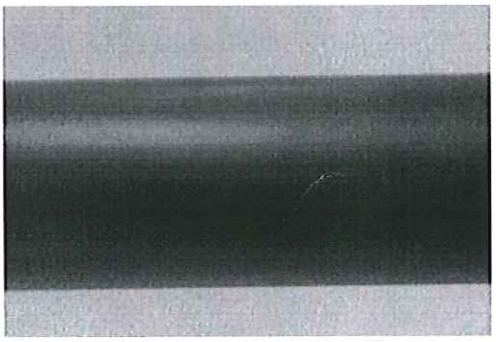

Figure 23 The characteristics of the anodized aluminium in 3 thickness levels

The characteristics of Sn-Al_2O_3 anodized aluminium

The objective of this section is discuss the characterization of the Sn-Al_2O_3 anodized aluminium film.

Five analysis methods can be used to identify the characteristics of anodized aluminium film;

X-ray Diffraction (XRD)

Scanning Electron Microscope (SEM)

Energy Dispersive Spectrometry (EDS)

Ultraviolet-Visible-Near Infrared Spectrometer (UV-VIS-IR)

Laser Flash Analyzer (LFA)

X-ray Diffraction Analysis

Figure 21 shows the XRD pattern of Sn-Al_2O_3 film deposited on the Al substrate, compared with the JCPDS database of Al, Al_2O_3 and Sn with the reference no. 01-1176, 01-1243 and 01-0926. In the diffraction pattern, only the diffraction peaks from the Al substrate and Sn pigment were observed, indicating that the X-ray penetrated through the Al_2O_3 film and reached the Sn pigment and Al substrate. However, Al_2O_3 phase was not detected in the sample of Sn-Al_2O_3 film because the underlying porous Al_2O_3 film seemed to be fully amorphous phase, which accords with the previous results for Mo- Al_2O_3 [60], Pt- Al_2O_3 [61] and Ag- Al_2O_3 [62] solar selective coating.

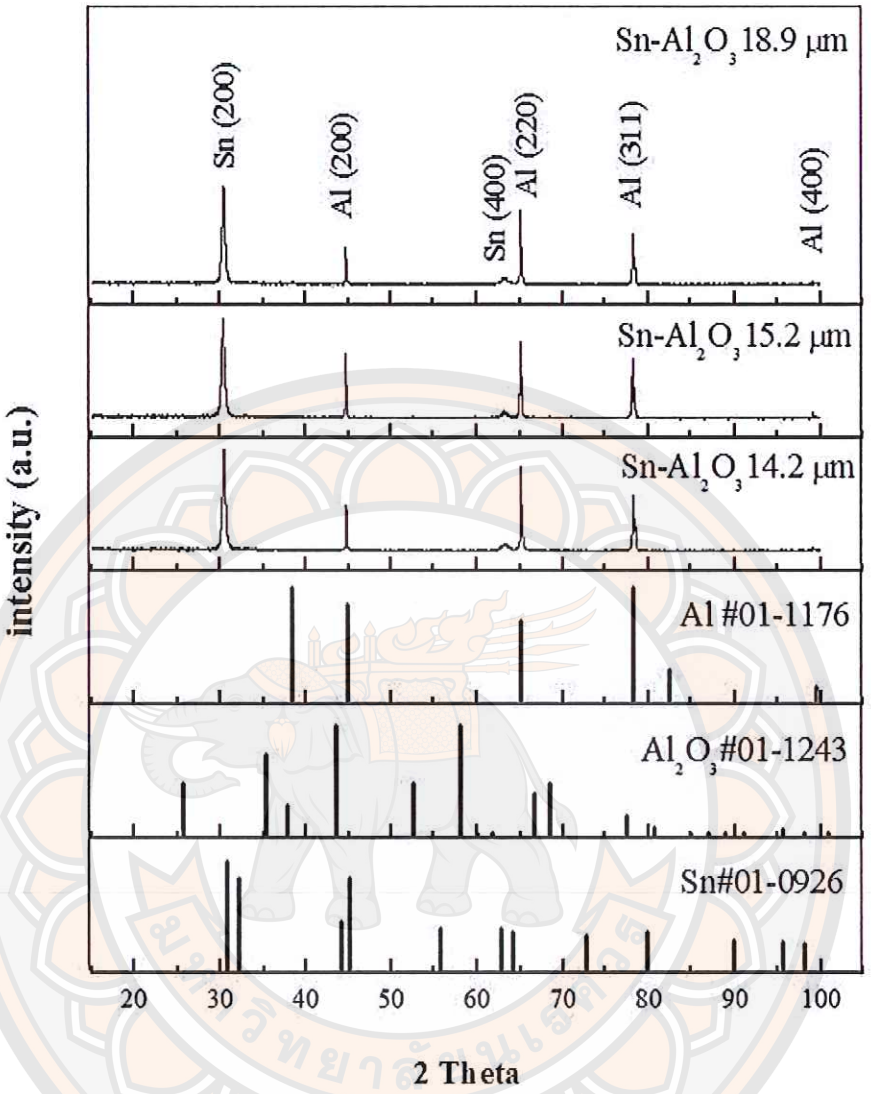

Figure 24 The XRD pattern of Sn-Al_2O_3 solar absorber

Scanning Electron Microscope Analysis

Figures 22(a, b)-24(a, b) present the SEM images of the three thickness levels of the Sn-Al_2O_3 solar absorber prepared by an anodization process. The surface morphology of the Sn-Al_2O_3 solar absorber has a dense and relatively smooth surface over the entire sample (Figure 22(a)-24(a)). As illustrated in Figures 22(b)-24(b), the Al_2O_3 film was formed on the Al substrate with a constant level of thickness over the film. The average thickness is shown in Table 14. It was also observed that the porous Al_2O_3 layer had high adhesion contact with the compact Al_2O_3 barrier and Al substrate, corresponding with the Ni-Al_2O_3 selective absorber [44, 63]. When

characterization of the cross-sectional morphology of Sn-Al_2O_3 solar absorber was done (Figure 22(b)-24(b)), it was found that the porous Al_2O_3 film presents two different contrast regions according to the different phases or atomic numbers with a strong compositional contrast in the sample surface. The light gray region corresponded to the Sn pigment rich area while the dark gray region corresponded to the Al_2O_3 phase. The Sn pigment rich area presents high contrast regions near the Al substrate interface. This is due to the pores of the Al_2O_3 being filled with the Sn pigment during the electrochemical deposition process.

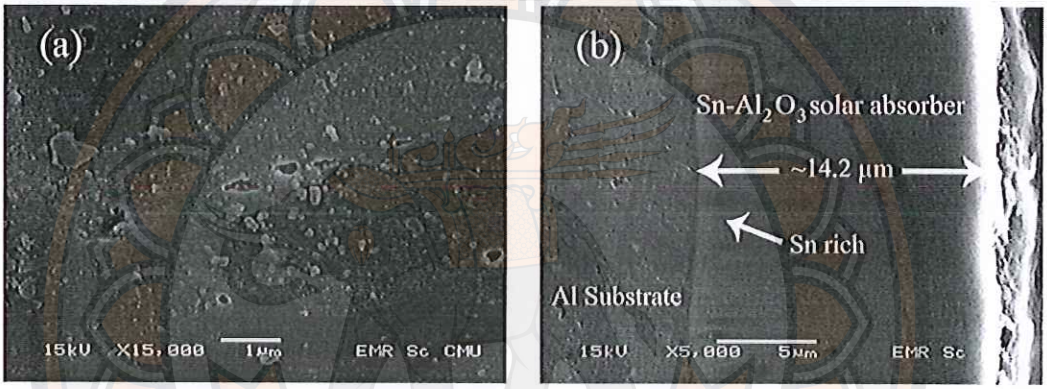

Figure 25 SEM images of the 14.2 μm thickness (a) surface and (b) cross-sectional morphology of Sn-Al_2O_3 solar absorber

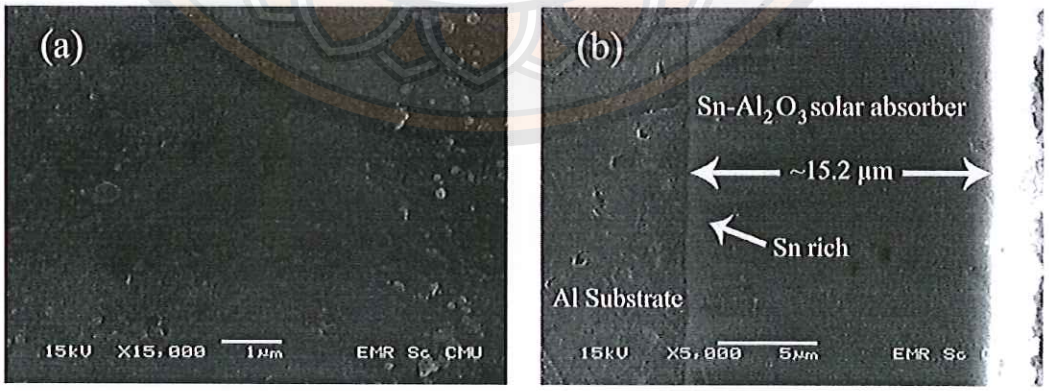

Figure 26 SEM images of the 15.2 μm thickness (a) surface and (b) cross-sectional morphology of Sn-Al_2O_3 solar absorber

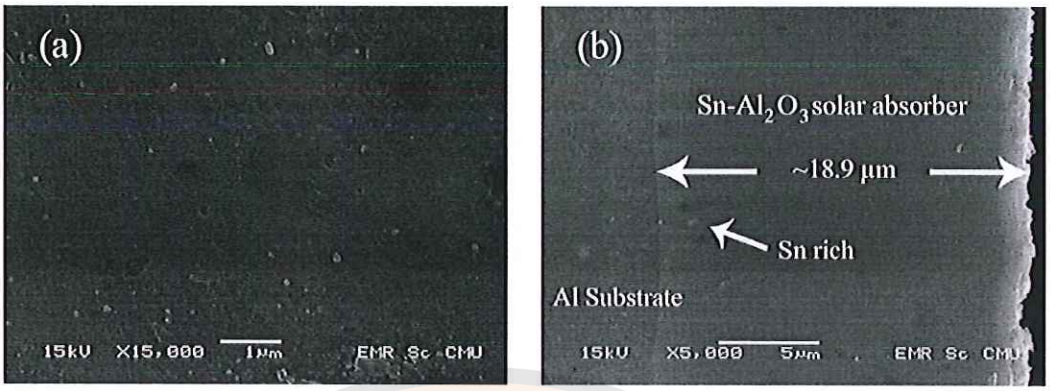

Figure 27 SEM images of the 18.9 μm thickness (a) surface and (b) cross-sectional morphology of Sn-Al_2O_3 solar absorber

Table 14 The average thickness of aluminium oxide film on the aluminium tube surface

Levels of thickness	The average thickness of Aluminium oxide (μm)
A	14.2
B	15.2
C	18.9

Energy Dispersive Spectrometry Analysis

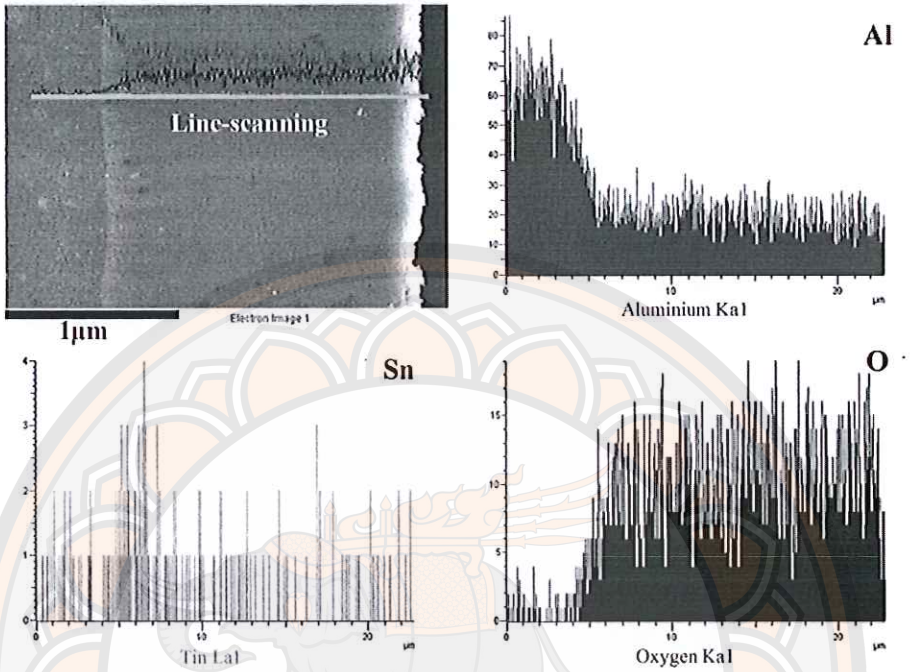

Figure 28 SEM-EDS line scanning profiles of cross-sectional Sn-Al_2O_3 solar absorber

In order to demonstrate the existence of the Sn pigment in the porous Al_2O_3 film, it was characterized by SEM-EDS with the line scan analysis technique. In this technique, the primary electron beam is focused on the surface of the Sn-Al_2O_3 solar absorber and scans in a line across the region of interest. The energy characteristics and number of emitted X-rays of the parent elements in the scan line are found and recorded by the EDS analyzer in the form of the accounting rate for each element (Al, O and Sn). Figure 25 shows the profiles of the distribution of elements in the cross-section of the surface of the Sn-Al_2O_3 solar absorber, which were in good agreement with the XRD pattern of the Sn-Al_2O_3 film. The Sn elements also showed a high count rate at the surface adjacent to the Al substrate indicating that the Sn pigments have a high concentration at the near interface of the Al substrate, corresponding to the Sn pigments that were deposited into the pores of the Al_2O_3 film by electrolysis. These

results also corresponded with the light gray region represented as Sn pigment rich area in Figure 22-24.

In order to confirm that the Sn element was in the Al_2O_3 film, SEM-EDS-mapping analysis was done. Figure 26 shows the results of the elements' distribution (aluminum (Al), tin (Sn) and oxygen (O), respectively). The bright green region indicates the presence of the Al element in the substrate, the red region indicates the Sn element which appears at the interface of the Al substrate and was deposited into the pores of the Al_2O_3 film. The blue region shows the oxygen element which occurred during the electrolysis process. Only the 18.9 μm thickness anodized film is shown. The thickness levels of 14 μm and 15 μm have similar substrate elements.

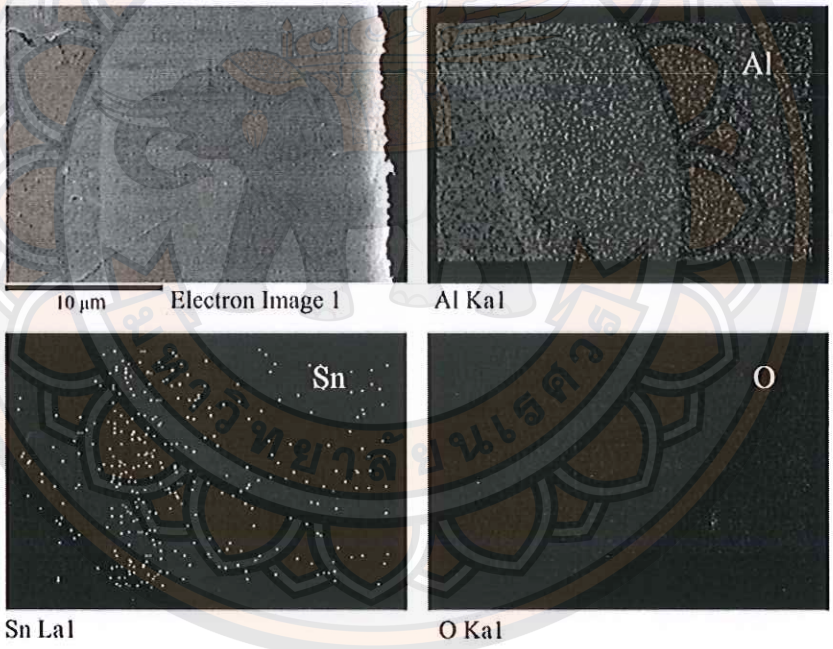

Figure 29 SEM-EDS mapping scanning profiles of cross-sectional Sn-Al_2O_3 solar absorber

Ultraviolet-Visible-Near Infrared Spectrometer analysis

Figure 27-29 show the measured reflectance at each wavelength (R_λ) (Green line) and calculated solar absorptance at each wavelength (α_λ) (Blue line) spectra of the Sn-Al_2O_3 solar absorber, together with the sun spectrum at AM 1.5 in the wavelength interval 300-2500 nm. of anodized aluminium at the thickness of 14.2,

15.2 and 18.9 μm. It can be observed that the R_λ of the sample is slightly increased with the increasing wavelength. Additionally, the R_λ was relatively low in the UV-Visible spectrum region (300-800 nm) while R_λ was high in the near infrared region. This can be explained by the Al_2O_3 layer without the Sn pigments (top layer) reducing the reflection (anti-reflecting layer) between the air and the Sn-pigmented Al_2O_3 layer (solar absorbing layer) [61, 64]. The α_λ of the Sn-Al_2O_3 solar absorber gradually decreased with the increasing wavelength. At all three thickness levels over the whole wavelength interval of the solar spectrum, the calculated R and α of the Sn-Al_2O_3 solar absorber was 0.06-0.07 and 0.93-0.94, respectively.

According to the experimental results, it is found that all the levels of thickness aluminium tubes have the similar absorptance with significant non-different values. This suggests that solar absorptance does not have differences along with the thickness of aluminium oxide films. However, it depends on the amount of Sn filled in the porous of aluminium oxide films. As a result, the solar absorptance of all the levels of thickness is so similar that it can be the same value. It seems that the spectral selectivity of the Sn-Al_2O_3 solar absorber mainly depends on the intrinsic absorption of the Sn pigments and the Al_2O_3 layer without the Sn pigments plays the role of anti-reflection. These results are in good agreement with a theoretical selective solar absorber for a photo-thermal conversion absorber. In addition, the R and α of the Sn-Al_2O_3 solar absorber were close to those of the related metal-Al_2O_3 solar absorbers such as Mo-Al_2O_3, Ni-Al_2O_3, W-Al_2O_3, Ag-Al_2O_3, Pt-Al_2O_3, and AlNi-Al_2O_3 solar absorbers [9, 44, 60, 61, 64, 65, 66] including the commercial solar selective absorber for solar-thermal energy conversion applications [44]. The values are shown in Table 15.

Table 15 The R and α of the Sn-Al_2O_3 solar absorber comparing with previous research

Selective surface	Result
Mo-Al_2O_3	α = 0.88-0.94, ε = 0.04-0.15
Ni-Al_2O_3	α = 0.85-0.97, ε = 0.08-0.21
W-Al_2O_3	α = 0.93, ε = 0.09 (400 °C)

Table 15 (cont.)

Selective surface	Result
Ag-Al_2O_3	$\alpha = 0.93$, $\varepsilon = 0.04\text{-}0.05$ (82 °C)
Pt-Al_2O_3	$\alpha \geq 0.98$, $\varepsilon \leq 0.05$
AlNi-Al_2O_3	$\alpha = 0.93$, $\varepsilon = 0.09$
Sn-Al_2O_3 (14.2 μm)	$\alpha = 0.94$
Sn-Al_2O_3 (15.2 μm)	$\alpha = 0.94$
Sn-Al_2O_3 (18.9 μm)	$\alpha = 0.93$

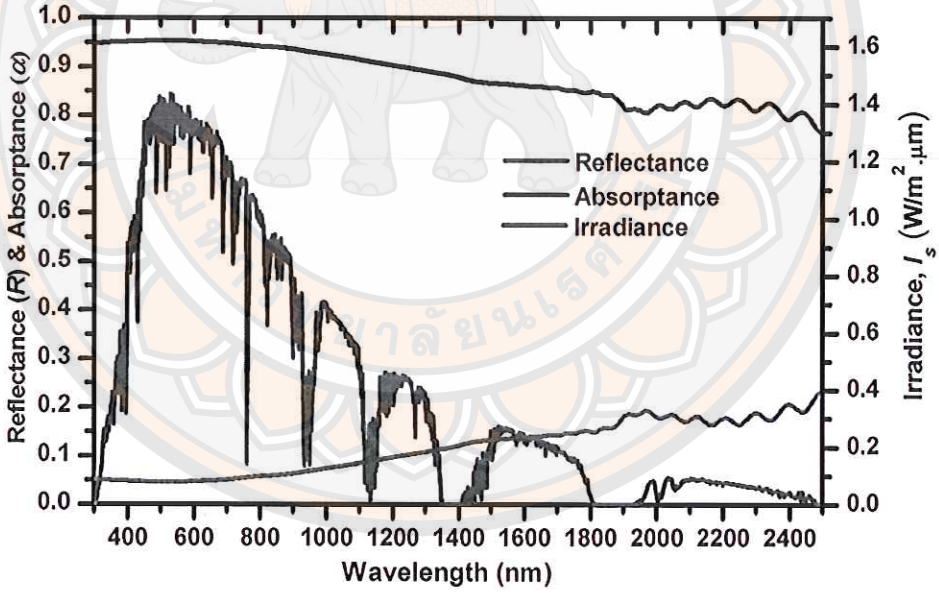

Figure 30 Spectral reflectance (*R*) and solar absorptance (α) curves of Sn-Al_2O_3 solar absorber, comparing with the sun spectrum at AM 1.5 in the wavelength interval 300-2500 nm of the thickness of 14.2 μm

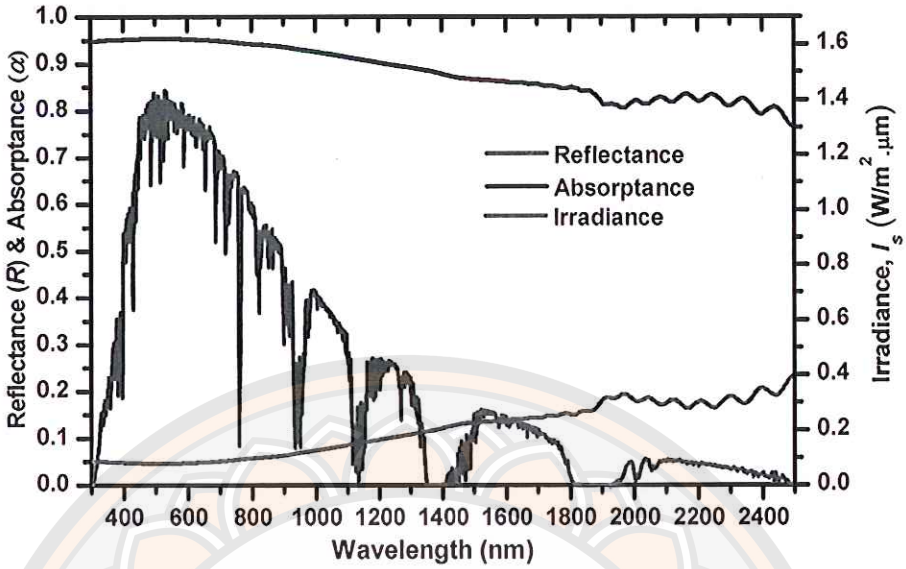

Figure 31 Spectral reflectance (R) and solar absorptance (α) curves of Sn-Al_2O_3 solar absorber, comparing with the sun spectrum at AM 1.5 in the wavelength interval 300-2500 nm of the thickness of 15.2 μm

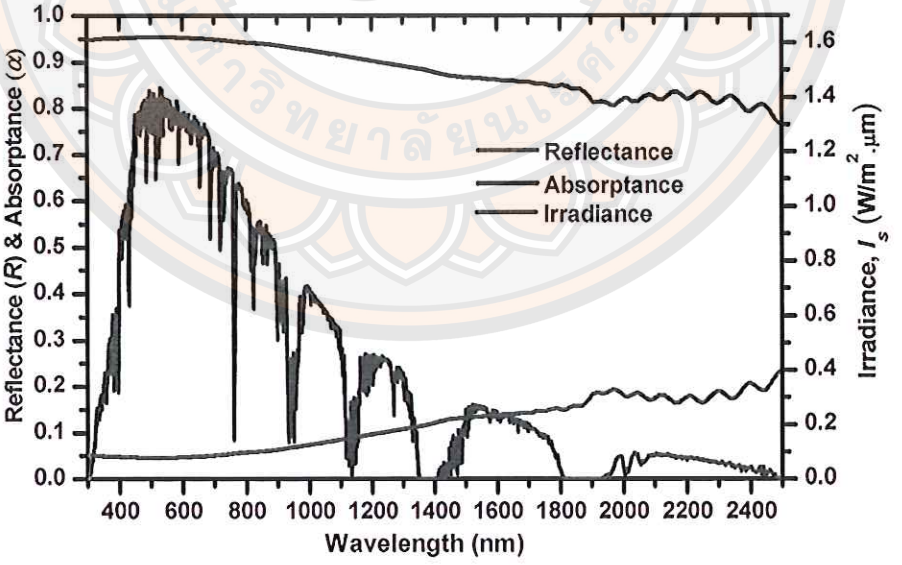

Figure 32 Spectral reflectance (R) and solar absorptance (α) curves of Sn-Al_2O_3 solar absorber, comparing with the sun spectrum at AM 1.5 in the wavelength interval 300-2500 nm of the thickness of 18.9 μm

The comparison of the solar absorptance and reflectance with thickness is shown in Table 16 These were not significantly different at all three thickness levels. This indicates that the solar absorptance does not change corresponding with the thickness of the aluminium oxide but with the amount of tin filling in the porous surface of the aluminium oxide. As a result, the solar absorptance in every level of thickness are similar.

It is, therefore, concluded that the Sn-Al_2O_3 solar absorber prepared by the anodic anodization process is a good candidate for being a solar selective absorber in the field of solar photo-thermal conversion applications.

Table 16 The absorptance and reflectance of Sn-Al_2O_3

Thickness (μm)	Reflectance (1)	Absorptance (1)
14.2	0.06	0.94
15.2	0.06	0.94
18.9	0.07	0.93

Laser Flash Analyzer (LFA)

Heat is transported in solid materials by both lattice vibration waves (phonons) and free electrons. A thermal conductivity is associated with each of these mechanisms, and the total conductivity is the sum of the two contributions, or

$$\kappa = \kappa_l + \kappa_e \qquad (49)$$

Where and represent the lattice vibration and electron thermal conductivities, respectively; usually one or the other predominates. The thermal energy associated with phonons or lattice waves is transported in the direction of their motion. The contribution results from a net movement of phonons from high- to low temperature regions of a body across which a temperature gradient exists. Free or conducting electrons participate in electronic thermal conduction. To the free electrons in a hot region of the specimen is imparted a gain in kinetic energy. They then migrate to colder areas, where some of this kinetic energy is transferred to the atoms themselves (as vibrational energy) as a consequence of collisions with phonons or other

imperfections in the crystal. The relative contribution of to the total thermal conductivity increases with increasing free electron concentrations, since more electrons are available to participate in this heat transference process. In high-purity metals, the electron mechanism of heat transport is much more efficient than the phonon contribution because electrons are not as easily scattered as phonons and have higher velocities. Furthermore, metals are extremely good conductors of heat because relatively large numbers of free electrons exist that participate in thermal conduction. Nonmetallic materials are thermal insulators in as much as they lack large numbers of free electrons. Thus the phonons are primarily responsible for thermal conduction: is much smaller than Again, the phonons are not as effective as free electrons in the transport of heat energy as a result of the very efficient phonon scattering by lattice imperfections. The scattering of lattice vibrations becomes more pronounced with rising temperature; hence, the thermal conductivity of most ceramic materials normally diminishes with increasing temperature, at least at relatively low temperatures [67]

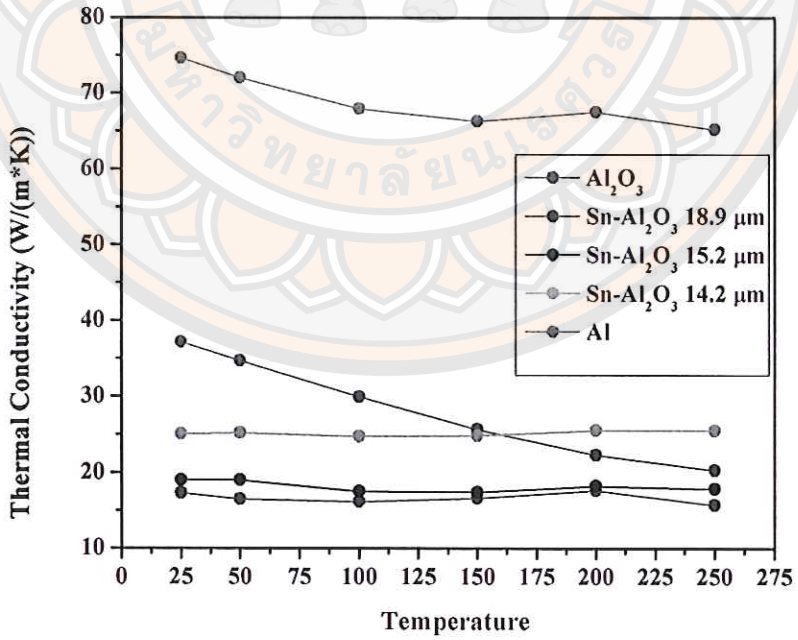

Figure 33 Thermal conductivity of anodized aluminium tube filled with tin ($Sn\text{-}Al_2O_3$) comparing with aluminium (Al) and aluminium oxide (Al_2O_3) [68]

The thermal conductivity of the aluminium, aluminium oxide and Sn-Al_2O_3 show in Figure 30. The results show that the thermal conductivity of Al_2O_3 lower than aluminium metal because Al_2O_3 present ceramic behavior [69, 70, 71, 72, 73]. The thermal conductivity of the Sn-Al_2O_3 is lower than Al_2O_3 at all the temperature period of the measurement, probably, the characteristic of Sn-Al_2O_3 film is the porous film by anodizing and the atom of Sn scattering phonon by lattice imperfection. The thermal conductivity of the Sn-Al_2O_3 decreases with increase the Sn-Al_2O_3 thickness due to the increasing of insulator layer (Al_2O_3).

The design and fabrication of the parabolic trough collector prototype

The prototype parabolic trough collector located in the School of Renewable Energy Technology, Naresuan University operating in tracking mode is used for heating water. The concentrator has a parabolic trough aperture range of 1.80 m and a length of 2 m, while the absorber tube is 2.54×10^{-2} m. outer diameter. The rim angle is 90°. The concentration ratio is 22.784. The parabolic structure is made from steel. The specular reflectivity of the concentrator surface is 0.92. The movement control system of the parabolic trough is an electric motor with gears monitored through a micro controller. The prototype collector uses locally available materials for the reflective sheets, the metal structure, and a manual solar tracker created for the experiment. Being hand constructed for the purpose, there may be errors in the solar focusing to the focus point. However, reduction in the design and construction costs was a factor to be considered. The prototype is shown in the photograph in Figure 31.

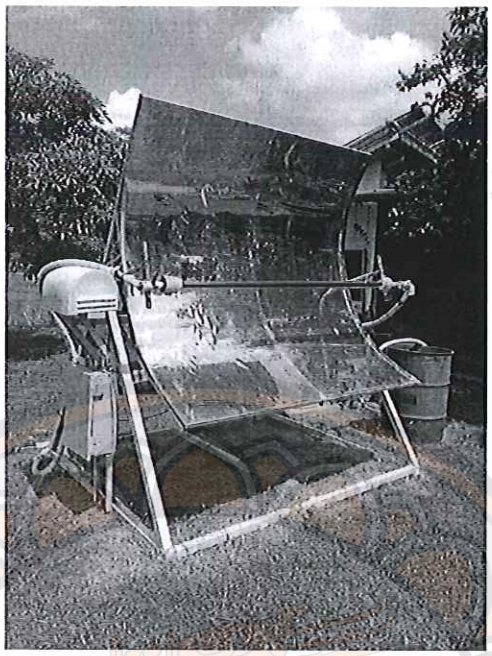

Figure 34 The prototype of the parabolic trough collector using anodized aluminium tube, as the solar receiver

Evaluation of the thermal efficiency of the parabolic trough collector system

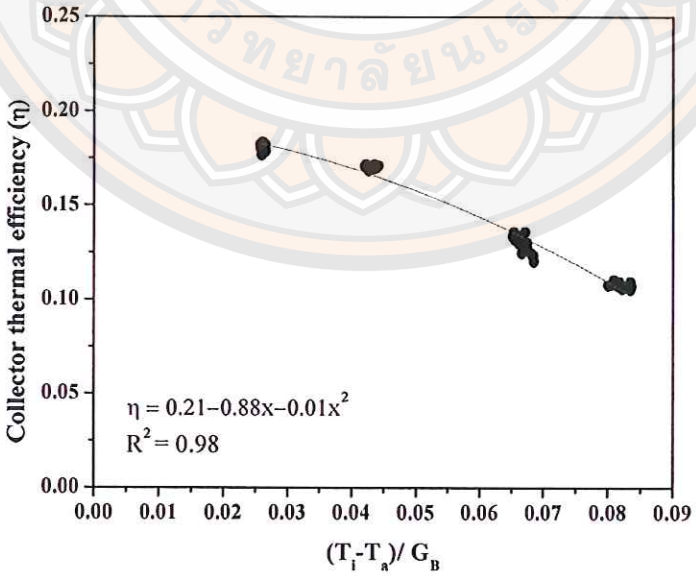

Figure 35 The thermal efficiency of the parabolic trough collector using thickness of 14.2 μm anodized aluminium tube, as the solar receiver

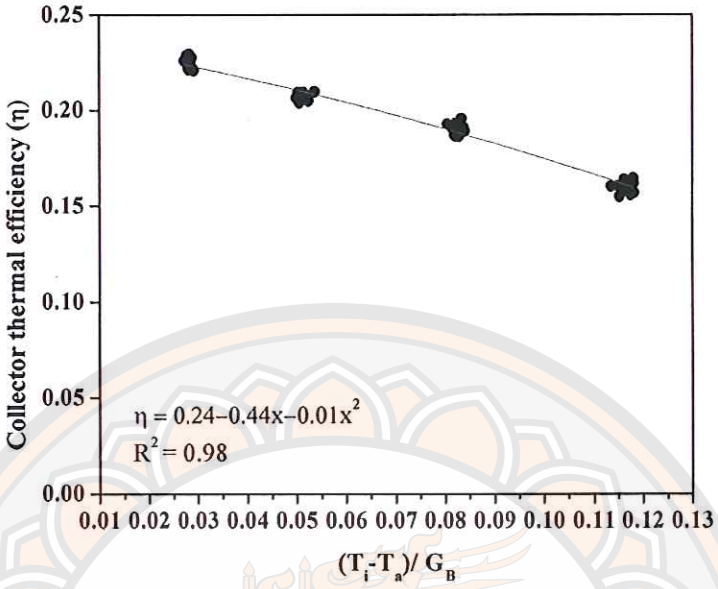

Figure 36 The thermal efficiency of the parabolic trough collector using thickness of 15.2 μm anodized aluminium tube, as the solar receiver

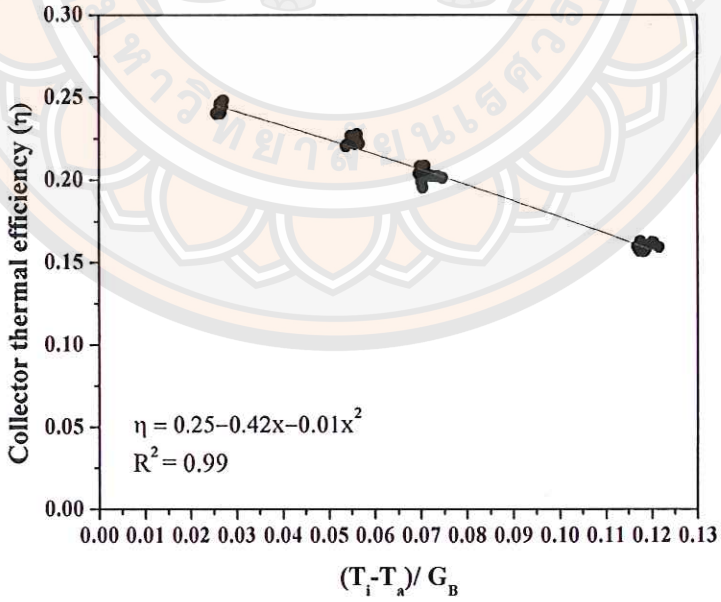

Figure 37 The thermal efficiency of the parabolic trough collector using thickness of 18.9 μm anodized aluminium tube, as the solar receiver

Figure 32-34 shows the thermal efficiency measurements of the parabolic trough collector using the thickness of 14.2, 15.2 and 18.9 μm, 2.0 meter long anodized aluminium tube as the solar receiver. These measurements were calculated by Equation 33, in Chapter 2. The heat loss coefficient U_L is not constant but is a function of the collector inlet and ambient temperatures. By appropriate curve fitting to a quadratic polynomial equation derived from the experimental results and observing the relationship between η and $(T_i - T_a)/G_B$, the equation to calculate thermal efficiency is show in table 17.

Table 17 The relationship between the thickness of anodized aluminium tube and the thermal efficiency equations of the parabolic trough collector model

Thickness (μm)	Thermal efficiency equations	$F_R\eta_0$	c_1/C	$c_2 G_B/C$
14.2	$\eta = 0.21 - 0.88x - 0.01x^2$	0.21	0.88	0.01
15.2	$\eta = 0.24 - 0.44x - 0.01x^2$	0.24	0.44	0.01
18.9	$\eta = 0.25 - 0.42x - 0.01x^2$	0.25	0.42	0.01

When the water input temperature is equal to the environmental temperature, the maximum thermal efficiency values of the solar collector of various thicknesses from the lowest to the highest were 0.21, 0.24 and 0.25 for 14.2, 15.2 and 18.9 μm. film thickness, respectively. Since most of Sn that was filled into the aluminium oxide film was inside the porous of the filmed that attached to the aluminium tube which was concerned with the results of SEM and SEM-EDS techniques tests as mentioned, the characters of aluminium oxide film would effected on better heat transfer when the film was thicker. In addition, the aluminium oxide film that was outside the tin layer had thermal insulation helped in reducing heat loss and solar reflection. This would effect on low reflectance which meant that the heat that was transmitted to aluminium tube was better than being transmitted aluminium oxide film. So, the aluminium tube could transmit the heat to the water better. Previous research reported that the thickness of the composite coating film with low pigment has the property of solar absorptance but causes high emittance (ε) [76, 77, 78, 79, 80, 81]. When compared to

the results obtained in this research. Found that the thickness of the layer of aluminum oxide was added. As a result, the absorptance is not significantly more. It is consistent with the thermal efficiency of the collector is more valuable as an increase in the aluminum oxide film. It can be explained that when the aluminium oxide film is thicker, the thermal efficiency of parabolic trough collector is higher. However, if it is too thick, it might affect the solar radiation.

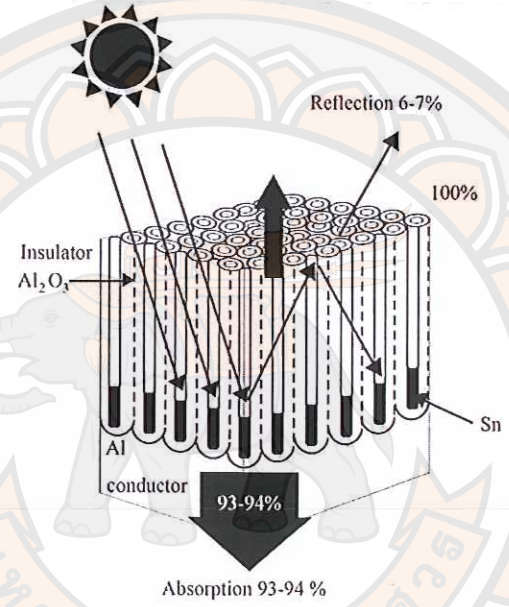

Figure 38 The diagram of thermal conductivity mechanism of anodized aluminium tube

The thermal conductivity experiments using Sn-Al_2O_3 can further explain the heat transfer mechanisms of the absorptance of Sn-Al_2O_3 film on the aluminium tube's surface. When heat occurred on Sn-Al_2O_3 film, the film transferred the heat to the aluminium tube substrate more efficiently than the Al_2O_3 film. This is because the aluminium tube's thermal conductivity is greater than that of the Al_2O_3 film. When thickness of Al_2O_3 film increase. Therefore, the heat at the interface of Sn-Al_2O_3 film and aluminium tube trend to transfer through the aluminium tube greater than Al_2O_3 layer. Some studies have reported in the literature on the effect of surface porosity on reducing the thermal conductivity of solids, especially the surface porosity of Al_2O_3 [74, 75].

Table 18 Comparison of thermal efficiency equations

Literatures		Thermal efficiency equation
Present study	14.2 μm	$\eta = 0.21 - 0.88x - 0.01x^2$
	15.2 μm	$\eta = 0.24 - 0.44x - 0.01x^2$
	18.9 μm	$\eta = 0.25 - 0.42x - 0.01x^2$
Kalogirou, S. [11]		$\eta = 0.62 - 0.18x - 0.14x^2$
Kalogirou, S. [82]		$\eta = 0.638 - 0.387x$
Valan, A.A. and Sornakumar, T. [83]		$\eta = 0.690 - 0.3865x$
Valan, A.A. and Sornakumar, T. [47]		$\eta = 0.69 - 0.39x$
Macro, S. [84]		$\eta = 0.700664 - 0.86590x$
Valenzuela, L., et al. [85]		$\eta = 0.768 - 0.063x$
Xu, L., et al. [86]		$\eta = 0.458 - 0.378x$
Kasaeian, A., et al. [87]		$\eta = 0.6730 - 0.2243x$

Table 18 compares the thermal efficiency with previously reported research [47, 82, 83, 84, 85, 86, 87]. The values calculated in the current study are lower than reported in the previous studies. This indicates heat loss both directly and indirectly to the environment from the surface of parabolic trough collector at all three 3 thickness levels of the anodized aluminium tube. The explanation for this could be that the previous researchers used standard materials purchased from material suppliers, whereas we used specially prepared materials, prepared as previously discussed. It is suggested that the thermal efficiency of the models in this research is relatively low because: 1) the materials e.g. reflects sheet, structure of the parabolic trough collector, and manual solar tracker created for the experiment might cause errors according to the design details effecting the solar focusing to the focus point. However, this design and creation does reduce the production costs, a matter not a matter considered in the previous research, which used sold material or the industry-use materials which are imported and thus expensive; 2) the parameter of the collector system designs are different from the previous research referred to; 3) the length of the solar collector with its tube and rail is only 2 meter which might effect on the thermal conductivity between the solar receiver tube and the fluid with a short period of transfer; 4) the

solar irradiance for the experiment is low between 300-320 W/m^2 while the ASHRAE 93-1986 standard of direct solar intensity must be more than 790 W/m^2; 5) the possibility of random data collection errors from the data logger and other calculations.

As a result, anodized aluminium tube is technically suitable because of its properties of low solar reflectance, high solar absorptance at the wavelength of solar irradiance, and good thermal efficiency. It is therefore considered appropriate for use in the solar collector industry where solar energy is being transformed into heat energy.

An economic assessment of the use of anodized aluminium

The objective of this section is to calculate the total cost of facility ownership and cost per unit of the PCT system. The first step is to calculate the NPV of the PCT system by using data and parameter values from chapter III. The results of the economic analysis are shown in Table 19-21.

Table 19 The LCC and LCOE of the parabolic trough collector using thickness of 14.2 μm anodized aluminium tube as the solar absorber

Year	Initial cost	O&M cost	Salvage value	O&M cost (NPV)	Salvage value (NPV)	Energy production
0	61,260					
1		306.30		282.62		883.86
2		306.30		260.77		883.86
3		306.30		240.61		883.86
4		306.30		222.01		883.86
5		306.30		204.84		883.86
6		306.30		189.01		883.86
7		306.30		174.40		883.86
8		306.30		160.91		883.86
9		306.30		148.47		883.86
10		306.30		136.99		883.86
11		306.30		126.40		883.86

Table 19 (cont.)

Year	Initial cost	O&M cost	Salvage value	O&M cost (NPV)	Salvage value (NPV)	Energy production
12		306.30		116.63		883.86
13		306.30		107.61		883.86
14		306.30		99.29		883.86
15		306.30	6,126	91.62	1,832.36	883.86
Total	61,260			2,562		13,257.97
LCC				61,989.84	Baht	
LCOE				4.676	Baht/kWh	

Table 20 The LCC and LCOE of the parabolic trough collector using thickness of 15.2 μm anodized aluminium tube as the solar absorber

Year	initial cost	O&M cost	Salvage value	O&M cost (NPV)	Salvage value (NPV)	Energy production
0	61,265					
1		306.33		282.64		1090.60
2		306.33		260.79		1090.60
3		306.33		240.63		1090.60
4		306.33		222.03		1090.60
5		306.33		204.86		1090.60
6		306.33		189.02		1090.60
7		306.33		174.41		1090.60
8		306.33		160.93		1090.60
9		306.33		148.49		1090.60
10		306.33		137.01		1090.60
11		306.33		126.41		1090.60
12		306.33		116.64		1090.60
13		306.33		107.62		1090.60
14		306.33		99.30		1090.60
15		306.33	6,127	91.63	1,832.51	1090.60

Table 20 (cont.)

Year	initial cost	O&M cost	Salvage value	O&M cost (NPV)	Salvage value (NPV)	Energy production
Total	61,265			2,562		16359.13
LCC				61,994.90	Baht	
LCOE				3.790	Baht/kWh	

Table 21 The LCC and LCOE of the parabolic trough collector using thickness of 18.9 μm anodized aluminium tube as the solar absorber

Year	initial cost	O&M cost	Salvage value	O&M cost (NPV)	Salvage value (NPV)	Energy production
0	61,265.00					
1		306.33		282.64		1,141.94
2		306.33		260.79		1,141.94
3		306.33		240.63		1,141.94
4		306.33		222.03		1,141.94
5		306.33		204.86		1,141.94
6		306.33		189.02		1,141.94
7		306.33		174.41		1,141.94
8		306.33		160.93		1,141.94
9		306.33		148.49		1,141.94
10		306.33		137.01		1,141.94
11		306.33		126.41		1,141.94
12		306.33		116.64		1,141.94
13		306.33		107.62		1,141.94
14		306.33		99.30		1,141.94
15		306.33	6,126.50	91.63	1,832.51	1,141.94
Total	61,265.00			2,562.41		17,129.21
LCC				61,994.90	Baht	
LCOE				3.619	Baht/kWh	

Table 22 The LCC and LCOE of 3 thicknesses

Thickness (μm)	Life Cycle Cost (Baht)	Levelized Cost of Energy (Baht/kWh)
14.2	61,989.84	4.67
15.2	61,994.90	3.79
18.9	61,994.90	3.61
Solar collector		
11	22,817.45	1.25
12	22,794.34	1.23
16	22,840.00	1.11

The result shows that the LCC of the system was 61,989.84 Baht (14.2 μm), 61,994.90 Baht (15.2 μm) and 61,994.90 Baht (18.9 μm). The LCOE of the system were 4.67 Baht/kWh (14.2 μm), 3.79 Baht/kWh (15.2 μm) and 3.61 Baht/kWh (18.9 μm). Comparing the LCOE to that reported in the previous literature [71], which used these same three thicknesses of anodized aluminium as the solar absorber, the cost per unit were 1.25 Baht/kWh (11 μm), 1.23 Baht/kWh (12 μm) and 1.11 Baht/kWh (16 μm). The cost of LCOE of the PCT system was higher than the LCOE of the ETC because the initial cost of construction of the system was high.

Considering the economic possibilities, anodized aluminium tube can be produced in Thailand and so doesn't need to be imported, resulting in a cheap cost, as well as being an impetus for development of a local industry. Cheaper solar collectors will encourage increased usage of renewable energy from the sun in heat production in many government/national enterprises and various areas of industry; large and many small industries that require a plentiful supply of hot water, such as hotels and hospitals, as well as for domestic use of solar hot water systems, house and building heating and the adaptation of the heat for cooling purposes using solar absorption cooling systems.

CHAPTER V

CONCLUSION

The conclusions and recommendations arising from this research are described in this chapter.

Conclusions

The characteristics of anodized aluminium

The analytical results of the properties of the three levels of thickness of anodized aluminium tubes were that the tubes are dark black color and less shiny, due to the pigment of the tin that filled into the porous surface of the aluminium oxide film layer. The average thickness values were, at 14.2, 15.2 and 18.9 μm. The tin content was higher around the interface area between the film and the aluminium tube. The XRD pattern formats are similar to each other and manifest the same patterns as the standard for aluminium JCPDS phase (Al, JCPD#001-1176) and tin (Sn, JCPDS#001-0926).

The results from the solar reflectance measurements over 250-2,500 nm. wavelengths are that the anodized aluminium tube with the aluminium oxide film layer filled with tin has low reflectance (R) at all three thickness levels. The solar absorptance (α) of all three thickness levels of the anodized aluminium tube is high and non-different (α = 0.93 - 0.94). This suggests that the solar absorptance of the anodized aluminium is similar to commercial solar absorbers. It can therefore be concluded that anodized aluminium with tin filling the porous surface of the aluminium oxide film layer can be applied as the solar absorber.

The design and fabrication of a parabolic trough collector prototype

The design and fabrication of a solar parabolic trough is not a difficult or expensive activity when using locally available materials, as is the case in Thailand. This means that low temperature troughs are an appropriate, indeed ideal, solar thermal device for local use especially in rural areas where they can be fabricated in any village or farm workshop.

The evaluation the thermal efficiency of the parabolic trough collector system

The results of the thermal efficiency measurement of parabolic trough collector with three thickness levels of anodized aluminium tubes as the solar absorber were; when the water input temperature is equal to the environmental temperature, the maximum thermal efficiency values of the solar collector of various thicknesses from the lowest to the highest were 0.21, 0.24 and 0.25 for 14.2, 15.2 and 18.9 μm film thickness, respectively.

At the present time, there is no use in industry of anodized aluminium apart from use in architectural features as door and window frames. The current research has demonstrated that anodized aluminium can be very effectively used as tubing in parabolic trough collectors in the heat ranges appropriate to heating water in the volumes and to the temperatures required in both domestic and small industrial applications. This has, therefore, opened a significant window of opportunity for Thai industry.

An economic assessment of the use of anodized aluminium

The results of the LCC of parabolic trough collector model with three thickness levels of anodized aluminium tubes as the solar absorber were 61,989.84 Baht (14.2 μm), 61,994.90 Baht (15.2 μm) and 61,994.90 Baht (18.9 μm). The LCOE of the system were 4.67 Baht/kWh (14.2 μm), 3.79 Baht/kWh (15.2 μm) and 3.61 Baht/kWh (18.9 μm). For LCC the cost different only for anodized the tube but for LCOE annual energy is different following the thermal efficiency equation.

Considering the economic possibilities, anodized aluminium tube can be produced relatively cheaply in Thailand, especially when compared to imported materials. Local production would give considerable impetus for the development of a local industry in Thailand. The resulting cheaper solar collectors will encourage increased usage of renewable energy from the sun in heat production in many government/national enterprises and various areas of industry; large and many small industries that require a plentiful supply of hot water, such as hotels and hospitals, as well as for domestic use of solar hot water systems, house and building heating and the adaptation of the heat for cooling purposes using.

Recommendations

1. Further research is recommended with a number of experimental projects suggested to test different aspects of the use of solar collectors. These include:

2. To ascertain the thermal efficiency of parabolic solar concentrator models at high temperatures, using anodized aluminium tubing as the receiver tube under direct solar intensity conditions of more than 790 W/m^2.

3. Using anodized aluminium tubes of more than 2 meter in length should be developed in order to achieve more accurate thermal efficiency measurements.

4. Develop a hot water production system using a parabolic trough collector.

5. Further study the effect of Sn content in Al_2O_3 film on thermal efficiency.

REFERENCE

REFERENCE

[1] Energy Situation. (2015). **Department of alternative energy development and efficiency ministry of energy**. Retrieved July 3, 2015, from http://www.dede.go.th/download/state_58/sit_57_58/frontpagjun_58.pdf.

[2] Buck, R., Brauning, T., Denk, T., Pfander, M., Schwarzbozl, P. and Tellez, F. (2002). Solar-hybrid gas turbine-based power tower systems (REFOS). **Trans ASME,** 124, 2-9.

[3] Romero, M., Buck, R. and Pacheco, J.E. (2002). An update on solar central receiver systems, projects, and technologies. **Trans ASME**, 124, 98-108.

[4] Romero, M., Marcos, M.J., Osuna, R. and Fernandez, V. (2000). **Design and implementation plan of a 10 MW solar tower power plant based on volumetric-air technology in Seville (Spain).** N.P.: n.p.

[5] Mancini, T., Heller, P., Butler, B., Osborn, B., Schiel, W., Goldberg, V., et al. (2003). Dish-stirling systems: an overview of development and status. **Solar Energy**, 125, 135-151.

[6] Janjai, S., Laksanaboonsong, J. and Seesaard, T. (2011). Potential application of concentrating solar power systems for the generation of electricity in Thailand. **Applied Energy**, 88, 4960-4967.

[7] Kadirgan, F., Wackelgard, E. and Sohmen, M. (1999). Electrochemical characterization of Al_2O_3-Ni thin film selective surface on aluminum. **Turk Chem**, 23(4), 381-391.

[8] Salmi, J., Bonino, J.P. and Bes, R.S. (2000). Nickel pigmented anodized aluminums solar selective absorbers. **Materials Science**, 35, 1347-1351.

[9] Kennedy, C.E. (2002). **Review of mid-to high-temperature solar selective absorber materials**. N.P.: n.p.

[10] Kalogirou, S.A. (2009). **Solar energy engineering: Process and systems**. United State of America: Academic.

[11] Kalogirou, S.A. (2004). Solar thermal collectors and applications. **Progress in Energy and Combustion Science**, 30, 231-295.

[12] Fernandez-Carcia, A., Zarza, E., Valenzuela, L. and Perez, M. (2010). Parabolic-trough solar collectors and their applications. **Renewable and Sustainable Energy Reviews**, 14, 1695-1721.

[13] German Solar Energy Society (DGS). (2010). **Planning and installing solar thermal systems: A guide for installers, architects and engineers**. UK: Jame and Jame.

[14] Peuser, F.A., Remmers, K.H. and Schnauss, M. (2002). **Solar thermal systems: Successful planning and construction**. UK: Jame and Jame.

[15] Sergeant, N.P., Pincon, O., Agrawal, M. and Peumans, P. (2009). Design of wide-angle solar-selective absorbers using aperiodic metal-dielectric stacks. **Optics Express**, 17(25), 22800-22812.

[16] Duffie, J.A. and Beckman, W.A. (2006). **Solar engineering thermal process** (3rd ed.). United State of America: Johnwiley and Sons.

[17] Kaufman, J.G. (2000). **Introduction to aluminum alloys and tempers.** USA: The Materials Information Society, ASM International.

[18] Li, L. (2000). Formation of ultrafine metal particles and metal oxide precursor on anodized Al by electrolysis deposition. **Materials Science and Technology,** 16(1), 50-54.

[19] Kopeliovich, D. (2013). **Anodizing.** Retrieved December 14, 2013, from http://www.substech.com/dokuwiki/doku.php?id=anodizing

[20] Shaffei, M.F., Abd El-Rehim, S.S., Shaaban, N.A. and Huisen, H.S. (2011). Electrolytic coloring of anodic aluminum for selective solar absorbing films: Use of additives promoting color depth and rate. **Renewable energy**, 23(3-4), 489-495.

[21] Fuller, S.K. and Petersen, S.R. (1995). **Life-cycle costing manual for the federal energy management program.** N.P.: n.p.

[22] Mearig, T., Coffee, N. and Morgan, M. (1999). **Life cycle cost analysis handbook.** Juneau, Alaska: Department of Education and Early Childhood Development Education Support Services Facilities.

[23] Robinson, J. (1996). Plant and equipment acquisitions: A life cycle costing case study. **Facilities**, 14(6), 21-25.

[24] Ashworth, A. (1996). Estimating the life expectancies of building components in life-cycle costing calculations. **Structural Survey**, 14(2), 4-8.

[25] El-Haram M. and Horner, R.M.W. (2002). Practical application of RCM to local authority housing: A pilot study. **Journal of Quality in Maintenance Engineering**, 8, 135-143.

[26] Barringer, H.P. and Weber, D.P. (1996). Life cycle cost tutorial. In **Fifth International Conference on Process Plant Reliability** (p.58). Houston, Texas: n.p.

[27] Jones, J.V. (1994). **Integrated logistic support handbook**. New York: McGraw Hill.

[28] Hibi, S. (1978). **How to measure maintenance performance** (2nd ed.). Japan: Asian Productivity Organization.

[29] Sieglinde, K. and Stephen, R. (1986). **Life cycle costing manual for the Federal energy management program**. N.P.: n.p.

[30] Short, W., Packey, D.J. and Holt, T. (1995). **A manual for economic evaluation of energy efficiency and renewable energy technologies**. N.P.: n.p.

[31] Abbas, A. (2000). Solchrome solar selective coatings -an effective way for solar water heaters globally. **Renewable Energy**, 19(1), 145-154.

[32] Antonaia, A., Castaldo, A., M.L. and Esposito, S. (2010). Stability of W-Al_2O_3 cermet based solar coating for receiver tube operating at high temperature. **Solar Energy materials and Solar Cells**, 94(10), 1604-1611.

[33] Wackelgard, E., Bostrom, T., Mattsson, A., Zhao, S., Crema, L., Bartali, R., et al. (2010). **New development of spectrally selective solar-absorbing coating for low and intermediate temperature applications.** N.P.: n.p.

[34] AlShamaileh, E. (2010). Testing of new solar coating for solar water heating application. **Solar Energy**, 84, 1637-1643.

[35] Culha, O., Celik, E., Ak Azem, N.F., Birlik, I., Toparli, M. and Turk, A. (2008). Microstructural, thermal and mechanical properties of HVOF sprayed Ni–Al-based bond coatings on stainless steel substrate. **Material Processing Technology**, 204, 221-230.

[36] Sampath, S., Jiang, X.Y., Matejicek, J., Prchik, L., Kulkarni, A. and Vaidya, A. (2004). Pole of thermal spray processing method on the microstructure, residual stress and properties of coating: an integrated study for Ni-5 wt% Al bond coats. **Material Science and Engineering**, A364, 216-231.

[37] Deshpande, S., Sampath, S. and Zhang, H. (2006). Mechanisms of oxidation and its role in microstructural evolution of metallic thermal spray coating-case study for Ni-Al. **Surface and Technology**, 200, 5395-5406.

[38] Tharamani, C.N. and Mayanna, S.M. (2007). Low cost black Cu-Ni alloy coating for solar energy applications. **Solar Energy Materials and Solar Cells**, 91(8), 664-669.

[39] Katumba, G., Makiwa, G., Baisitse, T. Olumekor, L., Forbes, A. and Wäckelgård, E. (2008). Solar selective absorber functionality of carbon nanoparticles embedded in SiO_2, ZnO and NiO matrices. **Physica status solidi(c)**, 5(2), 549-551.

[40] Dind, D., Cai, W., Long, M., Wu, H. and Wu, Y. (2010). Optical, structural and thermal characteristics of Cu–$CuAl_2O_4$ hybrids deposited in anodic aluminum oxide as selective solar absorber. **Solar Energy Materials and Solar Cells**, 94(10), 1578-1581.

[41] Wu, L., Gao, J., Liu, Z., Liang, L. Xia, F. and Wu, Y. (2013). Thermal aging characteristics of CrNxOy solar selective absorber coating for flat plate solar thermal collector applications. **Solar Energy Materials and Solar Cells**, 114, 186-191.

[42] Tesfamichael, T. and Wäckelgård E. (1999). Angular solar absorptance of absorbers used in solar thermal collectors. **Applied optics,** 38 (19), 4189-4197.

[43] Tesfamichael, T. and Wäckelgård E. (2000). Angular solar absorptance and incident angle modifier of selective absorbers for solar thermal collectors. **Solar Energy**, 68(4), 335-341.

[44] Wazwaz, A., Salmi, J. and Bes, R. (2010). The effects of nickel-pigmented aluminium oxide selective coating over aluminium alloy on the optical properties and thermal efficiency of the selective absorber prepared by alternate and reverse periodic plating technique. **Energy Conversion and Management**, 51(8), 1679-1683.

[45] Morrison, G.L. (1996). Solar water heaters markets and new developments. **Solar Technology,** 1, 307-316.

[46] Michael, G.B., Eckhard, L.F., Rafael, O.A., Antonio, E.A., Wolfgang, S.C. and Axel, S. (2002). **Euro trough-parabolic trough collector developed for cost efficient solar power generation.** Switzerland: Solar PACES Organization.

[47] Valan, A.A. and Sornakumar, T. (2007). Design manufacture and testing of fiberglass reinforced parabola trough for parabolic trough solar collectors. **Solar Energy,** 81, 1273-1279.

[48] Kumar, K.R. and Reddy, K.S. (2009). Thermal analysis of solar parabolic trough with porous disc receiver. **Applied Energy**, 86, 1804-1812.

[49] Krit, K. and Thanwa, J. (2006). **Economic analysis of project investment on hot water production from integrated solar energy system: Case study of Klang hospital, Rayong province.** Bangkok: Kasetsart University.

[50] Azaroff, L.V. (1974). **X-ray diffraction**. New York: McGraw Hill.

[51] Bragg's Law of Diffraction. (2015). **Electron microscopy.** Retrieved July 3, 2015, from http://www.microscopy.ethz.ch/bragg.htm.

[52] Cullity, B.D. (1978). **Element of x-ray diffraction** (2nd ed.). USA: Addison-Wesley.

[53] Lawes, G. (1987). **Scanning electron microscopy and x-ray microanalysis: Analytical chemistry by open learning**. New York: John Wiley and sons.

[54] Scanning Electron Microscope. (2015). **Purdue University**. Retrieved July 3, 2015, from https://www.purdue.edu/ehps/rem/rs/sem.htm.

[55] Denney, R.C. and Sinclair, R. (1987). **Visible and ultraviolet Spectroscopy: Analytical chemistry by open learning**. New York: John Wiley and sons.

[56] Katumba, G., Olumekor, L., Forbes, A., Makiwa, G., Mwakikunga, B., Lu, J., et al. (2008). Optical, thermal and structural characteristics of carbon nanoparticles embedded in ZnO and NiO as selective solar absorbers. **Solar energy materials and solar cells**, 92(10), 1285-1292.

[57] National Renewable energy Laboratory (NRLE). (2014). **Reference solar spectral irradiance: Air mass 1.5.** Retrieved July 3, 2015, from http://rredc.nrel.gov/solar/spectra/am1.5/.

[58] Lide, D.R. (2009). **CRC handbook of chemistry and physics** (90^{th} ed.). Boca Raton, Florida: CRC.

[59] Parker, W.J., Jenkins, R.J., Butler, C.P. and Abbott, G.L. (1961). Flash method of deter-mining thermal diffusivity, heat capacity, and thermal conductivity. **Journal of Applied Physics**, 32(9), 1679-1685.

[60] Du, X., Wang, C., Wang, T., Zhou, L., Chen, B. and Ru, N. (2008). Microstructure and spectral selectivity of Mo–Al_2O_3 solar selective absorbing coatings after annealing. **Thin Solid Films**, 516, 3971-3977.

[61] Nuru, Z.Y., Arendse, C.K., Nemutudi, R., Nemraoui, O. and Maaza, M. (2012). Pt-Al_2O_3 nanocoatings for high temperature concentrated solar thermal power applications, Physica B. **Condensed Matter**, 407, 1634-1637.

[62] Barshilia, H.C., Kumar, P., Rajam, K.S. and Biswas, A. (2011). Structure and optical properties of Ag–Al2O3 nanocermet solar selective coatings prepared using unbalanced magnetron sputtering. **Solar Energy Materials and Solar Cells**, 95, 1707-1715.

[63] Anderson, Å., Hunderi, O. and Granqvist, C.G. (1980). Nickel pigmented anodic aluminium oxide for selective absorption of solar energy. **Journal of Applied Physics**, 51, 754-764.

[64] Xue, Y., Wang, C., Wang, W., Liu, Y., Wu, Y., Ning, Y., et al. (2013). Spectral properties and thermal stability of solar selective absorbing AlNi–Al_2O_3 cermet coating. **Solar Energy**, 96, 113-118.

[65] Teixeira, V., Sousa, E., Costa, M.F., Nunes, C., Rosa, L., Carvalho, M.J., et al. (2001). Spectrally selective composite coatings of Cr-Cr_2O_3, and Mo-Al_2O_3 for solar energy applications. **Thin Solid Films,** 392, 320-326.

[66] Li, Z., Zhao, J. and Ren, L. (2012). Aqueous solution-chemical derived Ni–Al_2O_3 solar selective absorbing coatings. **Solar Energy Materials and Solar Cells**, 105, 90-95.

[67] Callister, W.D. and David, G.R. (2007). **Materials science and engineering: An introduction.** New York: Wiley.

[68] Hewitt, G.F. (2002). **Heat exchanger design handbook.** London, UK.: Begell House.

[69] Santos, W.N.D. and Taylor, R. (1993). Effect of porosity on the thermal conductivity of alumina. **High Temp - High Pressures**, 25, 89-98.

[70] Youngblood, G.E., Trice, R.W. and Ingel, R.P. (1988). Thermal diffusivity of partially and fully stabilized (yttria) zirconia single crystals. **Journal of the American Ceramic Society**, 71, 3255-3260.

[71] Touloukian, Y.S., Powell, R.W., Ho, C.Y. and Clemens, P.G. (1970). **Thermophysical Properties of Solids**. N.P.: n.p.

[72] Munro, R.G. (1997). Evaluated material properties for a sintered α-alumina. **Journal of the American Ceramic Society**, 80(8), 1919-28.

[73] Barea, R., Belmonte, M., Osendi, M.I. and Miranzo, P. (2003). Thermal conductivity of Al2O3/SiC platelet composites. **Journal of the European Ceramic Society**, 23(11), 1773-1778.

[74] Zivcova, Z., Gregorova, E., Pabst, W., Smith, D., Michot, A. and Poulier, C. (2009). Thermal conductivity of porous alumina ceramics prepared using starch as a poreforming agent. **Journal of the European Ceramic Society**, 29(3), 347-353.

[75] Nait-Ali, B., Haberko, K., Vesteghem, H., Absi, J. and Smith, D. (2007). Preparation and thermal conductivity characterisation of highly porous ceramics: Comparison between experimental results, analytical calculations and numerical simulations. **Journal of the European Ceramic Society**, 27(2), 1345-1350.

[76] Tesfamichael, T. (2000). **Characterization of selective solar absorbers: Experimental and theoretical modeling.** Thesis Ph.D., University Printers, Uppsala, Sweden.

[77] Belghith, M., Arurault, L. and Bes, R.S. (2013). Selective absorber obtained by nickel-pigmented anodized 6060 aluminium surface. **Arabian Journal for Science and Engineering**, 38(4), 751-757.

[78] Niklasson, G.A. and Granqvist, C.G. (1991). **Materials science for solar energy Conversion Systems**. N.P.: n.p.

[79] Buhrman, R.A. and Craighead, H.G. (1980). **Solar Materials Science**. N.P.: n.p.

[80] Uchino, H., Aso, S., Hozumi, S., Tokumasu, H. and Yoshioka, Y. (1979). Selective surfaces of color-anodized aluminum for solar collectors. **National Technology Report**, 25(5), 994-1004.

[81] Wäckelgård, E., Chibuye , T. and Karlsson, B. (1990). **Improved solar optical properties of a nickel pigmented anodized aluminum selective surface.** Oxford, UK.: Pergamon.

[82] Kalogirou, S. (1996). Parabolic trough collector system for low temperature steam generation: Design and performance characteristics. **Applied Energy**, 55(1), 1-19.

[83] Arasu, A.V. and Sornakumar, T. (2005). Design and simulation analysis of a parabolic trough solar collector hot water generation system. **International Energy Journal**, 6(2), 35-47.

[84] Sotte, M. (2002). **Design, test and mathematical modeling of parabolic trough solar collectors.** Thesis Ph.D., Università Politecnica delle, Marche, Italy.

[85] Valenzuela, L., López-Martín, R. and Zarza, E. (2014). Optical and thermal performance of large-size parabolic-trough solar collectors from outdoor experiments: A test method and a case study. **Energy**, 70, 456-464.

[86] Xu, L., Wang, Z., Li, X., Yuan, G., Sun, F., Lei, D., et al. (2014). A comparison of three test methods for determining the thermal performance of parabolic trough solar collectors. **Solar Energy**, 99, 11-27.

[87] Kasaeian, A., Daviran, S., Azarian, R.D. and Rashidi, A. (2015). Performance evaluation and nanofluid using capability study of a solar parabolic trough collector. **Energy Conversion and Management**, 89, 368-375.

APPENDIX

Powder-Diffract-File from JCPDS-ICDD

Name and formula

Reference code:	00-001-1176
PDF index name:	Aluminum
Empirical formula:	Al
Chemical formula:	Al

Crystallographic parameters

Crystal system:	Cubic
Space group:	Fm3m
Space group number:	225
a (Å):	4.0406
b (Å):	4.0406
c (Å):	4.0406
Alpha (Å):	90.0000
Beta (Å):	90.0000
Gamma (Å):	90.0000
Measured density (g/cm^3):	2.69
Volume of cell (10^6 pm^3):	65.97
Z:	4.00
RIR:	-

Status, subfiles and quality

Status:	Marked as deleted by ICDD
Subfiles:	Inorganic
Quality:	Blank (B)

Comments

Deleted by:	Deleted by NBS card.
Color:	White
Melting point:	660

References

Primary reference: Davey., *Phys. Rev.*, **25**, 753, (1925)

Optical data: *Data on Chem. for Cer. Use, Natl. Res. Council Bull. 107*

Unit cell: *The Structure of Crystals, 1st Ed.*

Peak list

No.	h	k	l	d [A]	2Theta[deg]	I [%]
1	1	1	1	2.34000	38.439	100.0
2	2	0	0	2.02000	44.833	90.0
3	2	2	0	1.43000	65.186	80.0
4	3	1	1	1.22000	78.306	100.0
5	2	2	2	1.17000	82.352	50.0
6	4	0	0	1.01000	99.401	40.0
7	3	3	1	0.93000	111.845	70.0
8	4	2	0	0.91000	115.662	70.0
9	4	2	2	0.83000	136.273	50.0
10	5	1	1	0.78000	161.909	60.0
11				0.72000		20.0

Stick Pattern

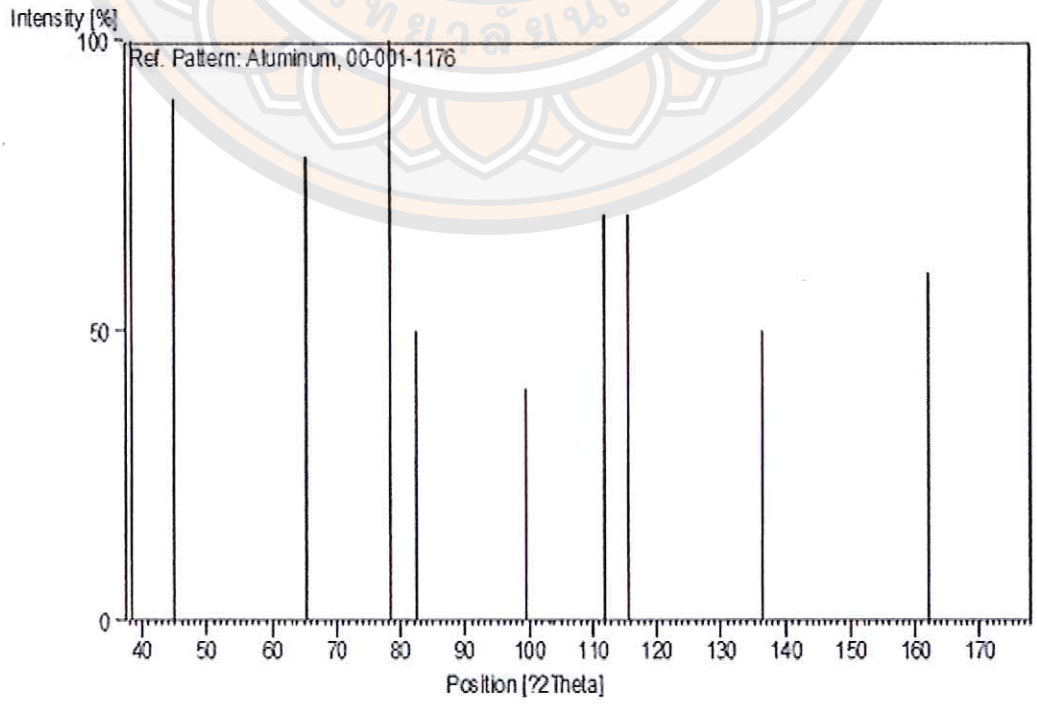

Name and formula

Reference code:	00-001-1243
PDF index name:	Aluminum Oxide
Empirical formula:	Al_2O_3
Chemical formula:	Al_2O_3

Crystallographic parameters

Crystal system:	Rhombohedral
Space group:	R-3c
Space group number:	167
a (Å):	4.7500
b (Å):	4.7500
c (Å):	12.9700
Alpha (Å):	90.0000
Beta (Å):	90.0000
Gamma (Å):	120.0000
Measured density (g/cm^3):	4.02
Volume of cell (10^6 pm^3):	253.43
Z:	2.00
RIR:	-

Status, subfiles and quality

Status:	Marked as deleted by ICDD
Subfiles:	Inorganic
Quality:	Blank (B)

Comments

Deleted by:	Deleted by NBS.
Color:	Various
Optical data:	A=1.7604, B=1.7686, Sign=-
Melting point:	2050
Unit cell:	Rhombohedral cell: a=5.120, a=55.28.

References

Primary reference: Hanawalt et al., *Anal. Chem.*, **10**, 475, (1938)

Unit cell: *Dana's System of Mineralogy, 7th Ed.*

Peak list

No.	h	k	l	d [A]	2Theta[deg]	I [%]
1	0	1	2	3.47000	25.652	50.0
2	1	0	4	2.55000	35.165	75.0
3	1	1	0	2.37000	37.934	30.0
4	1	1	3	2.08000	43.473	100.0
5	0	2	4	1.74000	52.553	50.0
6	1	1	6	1.59000	57.955	100.0
7	2	1	1	1.54000	60.026	5.0
8	0	1	8	1.50000	61.799	5.0
9	2	1	4	1.40000	66.763	40.0
10	3	0	0	1.37000	68.425	50.0
11	1	1	9	1.23000	77.549	20.0
12	2	1	7	1.19000	80.678	10.0
13	1	3	1	1.14000	85.017	5.0
14	1	2	8	1.12000	86.907	5.0
15	0	2	10	1.10000	88.898	5.0
16	0	0	12	1.08000	90.998	5.0
17	2	2	6	1.04000	95.578	8.0
18	0	4	2	1.02000	98.085	5.0
19	2	1	10	1.00000	100.762	5.0

Stick Pattern

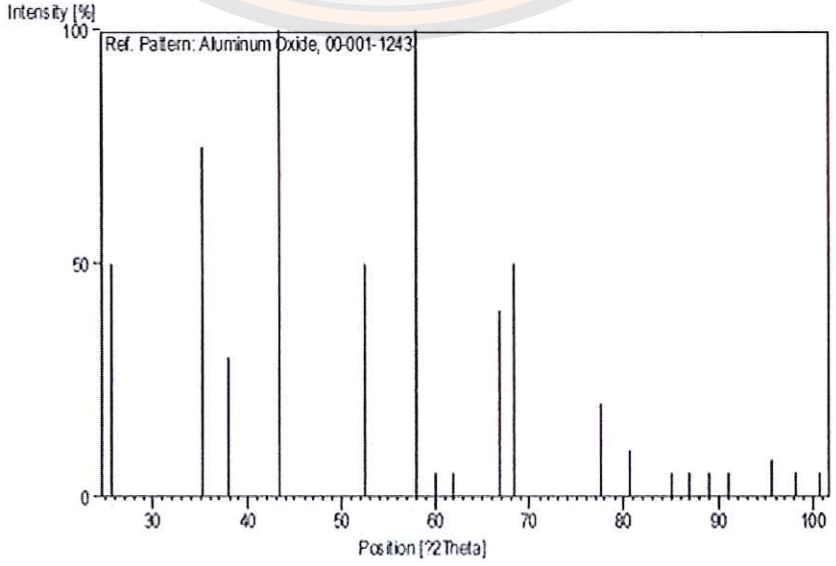

Name and formula

Reference code:	00-001-0926
PDF index name:	Tin
Empirical formula:	Sn
Chemical formula:	Sn

Crystallographic parameters

Crystal system:	Tetragonal
Space group:	I41/amd
Space group number:	141
a (Å):	5.8190
b (Å):	5.8190
c (Å):	3.1753
Alpha (Å):	90.0000
Beta (Å):	90.0000
Gamma (Å):	90.0000
Measured density (g/cm^3):	7.31
Volume of cell (10^6 pm^3):	107.52
Z:	4.00
RIR:	-

Status, subfiles and quality

Status:	Marked as deleted by ICDD
Subfiles:	Inorganic
Quality:	Blank (B)

Comments

Deleted by:	Deleted by NBS card.
Color:	Tin-white
Melting point:	231.8

References

Primary reference: Hanawalt et al., *Anal. Chem.*, **10**, 475, (1938)

Unit cell: *Dana's System of Mineralogy, 7th Ed.*

Peak list

No.	h	k	l	d [A]	2Theta[deg]	I [%]
1	2	0	0	2.91000	30.699	100.0
2	1	0	1	2.79000	32.054	80.0
3	2	2	0	2.05000	44.142	32.0
4	2	1	1	2.01000	45.068	80.0
5	3	0	1	1.65000	55.66	24.0
6	1	1	2	1.48000	62.728	24.0
7	4	0	0	1.45000	64.179	20.0
8	4	2	0	1.30000	72.675	16.0
9	3	1	2	1.20000	79.87	20.0
10	4	3	1	1.09000	89.934	11.0
11	1	0	3	1.04000	95.578	8.0
12	5	2	1	1.02000	98.085	6.0
13	2	1	3	0.98000	103.63	3.0
14	3	0	3	0.93000	111.845	6.0
15	3	2	3	0.89000	119.881	2.0
16	4	1	3	0.85000	129.98	3.0
17	6	4	0	0.81000	143.974	2.0

Stick Pattern

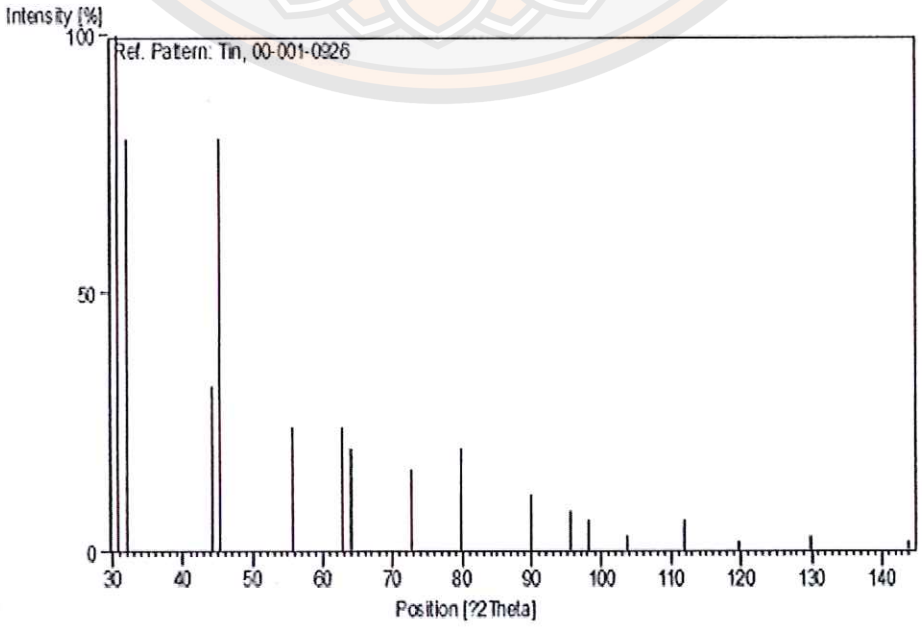

Table 23 The calculation of the solar absorptance of Sn-Al_2O_3 of the thickness of 14.2 μm

Wavelength	Direct circumsolar	I_{sol}	Reflectance	$1-R(\lambda)$	integrate	integrate I_{sol}	Absorptance	Absorptance* I_{sol}
nm	$W^*m^{-2*}nm^{-1}$	W^*m^{-2}	(1)		$I_{sol}*(1-R(\lambda))$		(%)	(%)
λ	I_{sol}	$I_{sol}(\lambda)$	R		$\int_{300}^{2500} I_{sol}(1-R(\lambda))d\lambda$	$\int_{300}^{2500} I_{sol}(\lambda)d\lambda$	α	
300	4.56E-04	1.37E-01	0.0466	0.953				
301	9.19E-04	2.77E-01	0.0466	0.953	0.0656	0.0006	95.5077	2.64E-01
302	1.46E-03	4.40E-01	0.0465	0.953	0.0011	0.0011	95.3400	4.20E-01
303	3.73E-03	1.13E+00	0.0465	0.953	0.0024	0.0025	95.3441	1.08E+00
304	5.10E-03	1.55E+00	0.0452	0.953	0.0042	0.0044	95.3463	1.48E+00
305	8.93E-03	2.72E+00	0.0465	0.953	0.0066	0.0070	95.3476	2.60E+00
306	1.02E-02	3.11E+00	0.0465	0.953	0.0090	0.0095	95.3476	2.96E+00
307	1.52E-02	4.68E+00	0.0465	0.953	0.0121	0.0126	95.3485	4.46E+00
308	2.08E-02	6.39E+00	0.0464	0.954	0.0171	0.0179	95.3508	6.09E+00
309	2.23E-02	6.89E+00	0.0464	0.954	0.0205	0.0215	95.3537	6.57E+00
310	2.78E-02	8.63E+00	0.0463	0.954	0.0238	0.0250	95.3586	8.23E+00

Table 23 (cont.)

Wavelength	Direct circumsolar	I_{sol}	Reflectance	$1-R(\lambda)$	integrate	integrate I_{sol}	Absorptance	Absorptance* I_{sol}
nm	$W^*m^{-2*}nm^{-1}$	W^*m^{-2}	(1)		$I_{sol}*(1-R(\lambda))$		(%)	(%)
λ	I_{sol}	$I_{sol}(\lambda)$	R		$\int_{300}^{2500} I_{sol}(1-R(\lambda))d\lambda$	$\int_{300}^{2500} I_{sol}(\lambda)d\lambda$	α	
311	4.54E-02	1.41E+01	0.0463	0.954	0.0349	0.0366	95.3641	1.35E+01
312	5.09E-02	1.59E+01	0.0462	0.954	0.0349	0.0006	95.3641	1.35E+01
.	.	.	.	.	.	.	.	.
.	.	.	.	.	.	.	.	.
2475	1.64E-02	4.05E+01	0.1567	0.843	0.0693	0.0825	84.0985	3.41E+01
2480	8.00E-03	1.98E+01	0.1515	0.848	0.0693	0.0825	84.0985	3.41E+01
2485	5.58E-03	1.39E+01	0.1471	0.852	0.0514	0.0609	84.4954	1.68E+01
2490	3.50E-03	8.70E+00	0.1434	0.856	0.0288	0.0339	85.0243	1.18E+01
2495	2.86E-03	7.15E+00	0.1402	0.859	0.0193	0.0226	85.4247	7.44E+00
2500	7.03E-03	1.76E+01	0.1378	0.862	0.0136	0.0159	85.7973	6.13E+00
		Total			0.8404	0.8404	0.9418	

Table 24 The calculation of the solar absorptance of Sn-Al_2O_3 of the thickness of 15.2 μm

Wavelength	Direct circumsolar	I_{sol}	Reflectance	$1-R(\lambda)$	integrate	integrate I_{sol}	Absorptance	Absorptance* I_{sol}
nm	$W^*m^{-2*}nm^{-1}$	W^*m^{-2}	(1)		$I_{sol}*(1-R(\lambda))$		(%)	(%)
λ	I_{sol}	$I_{sol}(\lambda)$	R		$\int_{300}^{2500} I_{sol}(1-R(\lambda))d\lambda$	$\int_{300}^{2500} I_{sol}(\lambda)d\lambda$	α	
300	4.56E-04	1.37E-01	0.0510	0.949				
301	9.19E-04	2.77E-01	0.0510	0.949	0.0653	0.0006	95.0674	2.63E-01
302	1.46E-03	4.40E-01	0.0509	0.949	0.0011	0.0011	94.8993	4.18E-01
303	3.73E-03	1.13E+00	0.0509	0.949	0.0024	0.0025	94.9038	1.07E+00
304	5.10E-03	1.55E+00	0.0509	0.949	0.0041	0.0044	94.9059	1.47E+00
305	8.93E-03	2.72E+00	0.0509	0.949	0.0066	0.0070	94.9085	2.59E+00
306	1.02E-02	3.11E+00	0.0508	0.949	0.0090	0.0095	94.9104	2.95E+00
307	1.52E-02	4.68E+00	0.0508	0.949	0.0120	0.0126	94.9121	4.44E+00
308	2.08E-02	6.39E+00	0.0508	0.949	0.0170	0.0179	94.913	6.07E+00
309	2.23E-02	6.89E+00	0.0508	0.949	0.0204	0.0215	94.9166	6.54E+00
310	2.78E-02	8.63E+00	0.0507	0.949	0.0237	0.0250	94.9205	8.19E+00

Table 24 (cont.)

Wavelength	Direct circumsolar	I_{sol}	Reflectance	$1-R(\lambda)$	integrate	integrate I_{sol}	Absorptance	Absorptance* I_{sol}
nm	$W^*m^{-2*}nm^{-1}$	W^*m^{-2}	(1)		$I_{sol}*(1-R(\lambda))$		(%)	(%)
λ	I_{sol}	$I_{sol}(\lambda)$	R		$\int_{300}^{2500} I_{sol}(1-R(\lambda))d\lambda$	$\int_{300}^{2500} I_{sol}(\lambda)d\lambda$	α	
311	4.54E-02	1.41E+01	0.0507	0.949	0.0347	0.0366	95.0674	2.63E-01
312	5.09E-02	1.59E+01	0.0507	0.949	0.0457	0.0006	94.9273	1.51E+01
.	.	.	.	.	.	.	.	.
.	.	.	.	.	.	.	.	.
2475	1.64E-02	4.05E+01	0.1405	0.859	0.0709	0.0825	86.0181	3.48E+01
2480	8.00E-03	1.98E+01	0.1428	0.857	0.0523	0.0825	85.8720	1.70E+01
2485	5.58E-03	1.39E+01	0.1459	0.854	0.0290	0.0609	85.5888	1.19E+01
2490	3.50E-03	8.70E+00	0.1503	0.850	0.0193	0.0339	85.2327	7.42E+00
2495	2.86E-03	7.15E+00	0.1554	0.845	0.0134	0.0226	84.7349	6.06E+00
2500	7.03E-03	1.76E+01	0.1598	0.840	0.0208	0.0159	84.1408	1.48E+01
		Total			0.8411	0.8922	0.9426	

Table 25 The calculation of the solar absorptance of Sn-Al_2O_3 of the thickness of 18.9 μm

Wavelength	Direct circumsolar	I_{sol}	Reflectance	$1-R(\lambda)$	integrate	integrate I_{sol}	Absorptance	Absorptance* I_{sol}
nm	$W^*m^{-2*}nm^{-1}$	W^*m^{-2}	(1)		$I_{sol}*(1-R(\lambda))$		(%)	(%)
λ	I_{sol}	$I_{sol}(\lambda)$	R		$\int_{300}^{2500} I_{sol}(1-R(\lambda))d\lambda$	$\int_{300}^{2500} I_{sol}(\lambda)d\lambda$	α	
300	4.56E-04	1.37E-01	0.0525	0.947				
301	9.19E-04	2.77E-01	0.0524	0.948	0.0006	0.0006	94.9222	2.63E-01
302	1.46E-03	4.40E-01	0.0524	0.948	0.0011	0.0011	94.7562	4.17E-01
303	3.73E-03	1.13E+00	0.0523	0.948	0.0025	0.0025	94.7597	1.07E+00
304	5.10E-03	1.55E+00	0.0523	0.948	0.0044	0.0044	94.7618	1.47E+00
305	8.93E-03	2.72E+00	0.0523	0.948	0.0070	0.0070	94.7660	2.58E+00
306	1.02E-02	3.11E+00	0.0523	0.948	0.0095	0.0095	94.7677	2.94E+00
307	1.52E-02	4.68E+00	0.0522	0.948	0.0126	0.0126	94.7705	4.44E+00
308	2.08E-02	6.39E+00	0.0522	0.948	0.0179	0.0179	94.7749	6.06E+00
309	2.23E-02	6.89E+00	0.0521	0.948	0.0215	0.0215	94.7792	6.53E+00
310	2.78E-02	8.63E+00	0.0520	0.948	0.0250	0.0250	94.7874	8.18E+00

Table 25 (cont.)

Wavelength	Direct circumsolar	I_{sol}	Reflectance	$1-R(\lambda)$	integrate	integrate I_{sol}	Absorptance	Absorptance* I_{sol}
nm	$W^*m^{-2*}nm^{-1}$	W^*m^{-2}	(1)		$I_{sol}*(1-R(\lambda))$		(%)	(%)
λ	I_{sol}	$I_{sol}(\lambda)$	R		$\int_{300}^{2500} I_{sol}(1-R(\lambda))d\lambda$	$\int_{300}^{2500} I_{sol}(\lambda)d\lambda$	α	
311	4.54E-02	1.41E+01	0.0520	0.948	0.0347	0.0366	94.7950	1.34E+01
312	5.09E-02	1.59E+01	0.0519	0.948	0.0456	0.0006	94.8015	1.51E+01
.	.	.	.	.	.	.	.	.
.	.	.	.	.	.	.	.	.
2475	1.64E-02	4.05E+01	0.2173	0.783	0.0648	0.0825	78.5476	3.18E+01
2480	8.00E-03	1.98E+01	0.2221	0.778	0.0475	0.0825	78.1030	1.55E+01
2485	5.58E-03	1.39E+01	0.2265	0.773	0.0263	0.0609	77.5994	1.08E+01
2490	3.50E-03	8.70E+00	0.2302	0.770	0.0175	0.0339	77.1991	6.72E+00
2495	2.86E-03	7.15E+00	0.2325	0.767	0.0122	0.0226	76.8698	5.49E+00
2500	7.03E-03	1.76E+01	0.2321	0.768	0.0189	0.0159	76.7733	1.35E+01
		Total			0.8922	0.8303	0.9305	

Table 26 The thermal efficiency of parabolic trough collector 14.2 µm

$T_{in}(^{\circ}C)$	$T_{out}(^{\circ}C)$	$T_{am}(^{\circ}C)$	$G_B(\mathrm{W/m^2})$	$(T_{in}-T_{am})/\mathrm{G_B}$	η
40.6	41.25	32.78	302.56	0.02584	0.18
40.61	41.24	32.81	300.08	0.02597	0.177
40.64	41.3	32.8	301.05	0.02605	0.182
40.65	41.3	32.88	300.97	0.0258	0.182
40.68	41.32	32.82	300.57	0.02613	0.179
40.68	41.33	32.8	300.51	0.02621	0.182
40.7	41.35	32.8	300.65	0.02627	0.182
40.74	41.4	32.89	300.21	0.02616	0.183
40.74	41.4	32.82	300.98	0.02633	0.182
40.8	41.45	32.84	300.73	0.02645	0.182
40.8	41.44	32.93	300.76	0.02616	0.179
40.8	41.44	32.82	300.47	0.02655	0.178
40.8	41.45	32.82	301.09	0.02651	0.18
40.82	41.47	32.96	300.13	0.02618	0.182
40.82	41.49	32.82	305.1	0.02623	0.183
40.84	41.51	32.89	305.67	0.02602	0.182
50.01	50.73	35.09	354.38	0.04209	0.171
50.17	50.9	35.04	357.92	0.04227	0.171
50.17	50.89	35.07	355.57	0.04247	0.169
50.18	50.9	35.02	352.81	0.04297	0.17
50.19	50.9	35.09	353.86	0.04266	0.168
50.23	50.94	35.06	350.55	0.04325	0.17
50.25	50.96	35.06	348.35	0.04359	0.172
50.25	50.97	35.07	349.51	0.04344	0.171
50.25	50.96	35.05	349.98	0.04343	0.169
50.28	51	35.07	352.93	0.0431	0.17
50.3	51.02	35.08	350.8	0.0434	0.171
50.31	51.02	35.04	351.38	0.04344	0.17
50.45	51.18	35.05	359.79	0.0428	0.17

Table 26 (cont.)

$T_{in}(^{\circ}C)$	$T_{out}(^{\circ}C)$	$T_{am}(^{\circ}C)$	$G_B(\mathrm{W/m^2})$	$(T_{in}-T_{am})/\mathrm{G_B}$	η
50.55	51.28	35.04	359.84	0.0431	0.17
50.56	51.28	35.05	350.81	0.04422	0.171
50.73	51.45	35.08	356.37	0.0439	0.17
58.06	58.6	35.36	344.08	0.06598	0.13
58.07	58.61	35.37	346.06	0.06558	0.132
58.08	58.62	35.34	343.07	0.06628	0.132
58.09	58.65	35.39	348.11	0.06522	0.133
58.14	58.7	35.4	347.57	0.06542	0.136
58.27	58.82	35.38	342.17	0.06689	0.135
58.45	58.98	35.42	347.69	0.06622	0.13
58.46	59.01	35.42	348.66	0.06608	0.131
58.57	59.09	35.39	347.53	0.06671	0.124
58.63	59.2	35.39	346.01	0.06717	0.136
58.7	59.2	35.3	341.67	0.06849	0.123
58.7	59.24	35.41	345.24	0.06746	0.13
58.84	59.35	35.4	342.86	0.06837	0.123
58.85	59.38	35.41	347.22	0.0675	0.127
58.87	59.38	35.34	345.83	0.06803	0.124
58.98	59.48	35.3	345.31	0.06859	0.12
65.03	65.55	32.77	397.59	0.08115	0.109
65.04	65.56	32.73	400.88	0.0806	0.108
65.2	65.73	32.74	400.66	0.08101	0.11
65.21	65.73	32.74	405.33	0.08011	0.107
65.29	65.78	32.76	389.72	0.08348	0.105
65.33	65.83	32.74	389.86	0.08361	0.107
65.34	65.86	32.76	401.95	0.08106	0.108
65.35	65.86	32.72	390.88	0.08348	0.109
65.69	66.22	32.7	405.71	0.08132	0.108
65.8	66.32	32.7	404.47	0.08184	0.107

Table 26 (cont.)

$T_{in}(^{\circ}C)$	$T_{out}(^{\circ}C)$	$T_{am}(^{\circ}C)$	$G_B(\mathrm{W/m^2})$	$(T_{in}-T_{am})/\mathrm{G_B}$	η
65.81	66.34	32.72	404.24	0.08186	0.109
65.85	66.38	32.72	405.42	0.08173	0.108
65.89	66.42	32.79	407.38	0.08126	0.108
65.94	66.47	32.75	407.31	0.08148	0.109
65.95	66.46	32.7	404.05	0.08229	0.106
65.96	66.48	32.77	406.41	0.08167	0.107

Table 27 The thermal efficiency of parabolic trough collector 15.2 µm

$T_{in}(^{\circ}C)$	$T_{out}(^{\circ}C)$	$T_{am}(^{\circ}C)$	$G_B(\mathrm{W/m^2})$	$(T_{in}-T_{am})/\mathrm{G_B}$	η
42.28	43.16	33.15	321.86	0.02837	0.23
42.66	43.53	33.13	327.88	0.02907	0.22
42.24	43.08	33.12	317.18	0.02875	0.22
42.17	43.03	33.11	317.06	0.02857	0.23
42.08	42.96	33.15	321.76	0.02775	0.23
42.23	43.11	33.17	320.69	0.02825	0.23
42.09	42.93	33.12	317.54	0.02825	0.22
42.34	43.21	33.14	323.02	0.02848	0.23
42.53	43.38	33.15	321.58	0.02917	0.22
42.17	43.06	33.18	329.65	0.02727	0.23
42.46	43.34	33.16	331.61	0.02805	0.22
42.38	43.23	33.14	320.14	0.02886	0.22
42.59	43.5	33.17	335.93	0.02804	0.23
42.42	43.3	33.13	323.22	0.02874	0.23
42.42	43.3	33.19	328.59	0.0281	0.22
42.43	43.3	33.17	329.97	0.02805	0.22
49.53	50.34	33.13	328.22	0.04997	0.21
50.04	50.84	33.19	323.54	0.05209	0.21
50.04	50.84	33.19	323.54	0.05209	0.21

Table 27 (cont.)

$T_{in}(^{\circ}C)$	$T_{out}(^{\circ}C)$	$T_{am}(^{\circ}C)$	$G_B(\mathrm{W/m^2})$	$(T_{in}-T_{am})/\mathrm{G_B}$	η
49.57	50.36	33.17	323.91	0.05063	0.2
49.79	50.61	33.19	328.68	0.05051	0.21
50.43	51.24	33.14	322.27	0.05366	0.21
50.43	51.24	33.15	322.27	0.05363	0.21
49.54	50.33	33.16	321.29	0.05098	0.21
49.56	50.38	33.14	325.93	0.05039	0.21
49.56	50.37	33.14	325.93	0.05039	0.21
49.77	50.58	33.18	328.52	0.05049	0.21
49.77	50.58	33.18	328.52	0.05049	0.21
49.92	50.7	33.13	320.47	0.05238	0.2
49.81	50.62	33.18	323.87	0.05134	0.21
49.81	50.62	33.18	323.87	0.05134	0.21
49.67	50.49	33.15	327.87	0.05039	0.21
60.15	60.88	33.39	326.42	0.08198	0.19
60.46	61.19	33.32	322.85	0.08406	0.19
60.24	60.99	33.37	326.77	0.08223	0.19
60.47	61.21	33.35	323.63	0.0838	0.19
60.44	61.19	33.36	325.53	0.08319	0.19
60.45	61.19	33.37	326.17	0.08302	0.19
60.42	61.18	33.36	329.24	0.08219	0.19
60.43	61.19	33.31	325.05	0.08343	0.2
59.73	60.49	33.32	328.01	0.08053	0.19
60.44	61.19	33.38	328.09	0.08248	0.19
60.19	60.93	33.37	322.74	0.0831	0.19
60.14	60.89	33.35	328.7	0.0815	0.19
60.48	61.21	33.35	327.33	0.08288	0.19
60.3	61.03	33.35	325.18	0.08286	0.19
60.01	60.73	33.38	324.16	0.08214	0.19
60.39	61.13	33.35	326.67	0.08277	0.19

Table 27 (cont.)

$T_{in}(^{\circ}C)$	$T_{out}(^{\circ}C)$	$T_{am}(^{\circ}C)$	$G_B(\mathrm{W/m^2})$	$(T_{in}-T_{am})/\mathrm{G_B}$	η
70.14	70.74	32.29	321.89	0.11759	0.16
70.23	70.87	32.24	326.47	0.11637	0.16
69.93	70.56	32.23	328.33	0.11482	0.16
70.55	71.16	32.28	324.48	0.11794	0.16
69.63	70.26	32.31	328.8	0.1135	0.16
70.66	71.3	32.21	326.44	0.1178	0.16
70.09	70.71	32.2	320.69	0.11815	0.16
70.29	70.91	32.24	327	0.11636	0.16
70.45	71.06	32	325.21	0.11823	0.16
70.17	70.78	32.21	329.28	0.11528	0.15
69.93	70.55	32.23	324.01	0.11635	0.16
70.08	70.71	32.25	325.31	0.11628	0.16
70.48	71.11	32.28	328.36	0.11635	0.16
70.14	70.77	32.32	323.7	0.11685	0.16
70.47	71.1	32.25	326.42	0.11709	0.16
70.57	71.21	32.2	324.9	0.1181	0.16

Table 28 The thermal efficiency of parabolic trough collector 18.9 µm

$T_{in}(^{\circ}C)$	$T_{out}(^{\circ}C)$	$T_{am}(^{\circ}C)$	$G_B(\mathrm{W/m^2})$	$(T_{in}-T_{am})/\mathrm{G_B}$	η
40.19	41.12	31.86	316.4	0.02633	0.246
40.22	41.15	31.94	323.93	0.02556	0.24
40.24	41.17	31.87	317.48	0.02636	0.245
40.29	41.2	31.86	316.65	0.02662	0.24
40.29	41.21	31.89	318.66	0.02636	0.241
40.29	41.22	31.8	321.79	0.02638	0.242
40.31	41.25	31.75	317.18	0.02699	0.248
40.37	41.32	31.84	322.85	0.02642	0.246
40.38	41.31	31.82	320.24	0.02673	0.243

Table 28 (cont.)

$T_{in}(^{\circ}C)$	$T_{out}(^{\circ}C)$	$T_{am}(^{\circ}C)$	$G_B(\mathrm{W/m^2})$	$(T_{in}-T_{am})/\mathrm{G_B}$	η
40.41	41.33	31.87	319.5	0.02673	0.241
40.44	41.38	31.84	322.98	0.02663	0.243
40.46	41.41	31.84	326.33	0.02641	0.243
40.46	41.39	31.85	318.46	0.02704	0.244
40.47	41.42	31.84	326.81	0.02641	0.243
40.5	41.44	31.84	323.14	0.0268	0.243
40.64	41.6	31.82	323.81	0.02724	0.248
50	50.89	31.66	331.68	0.05529	0.224
50.06	50.95	31.63	334.88	0.05503	0.222
50.21	51.1	31.6	334.97	0.05556	0.222
50.23	51.12	31.78	333.46	0.05533	0.223
50.23	51.12	31.68	331.73	0.05593	0.223
50.24	51.15	31.67	344.3	0.05394	0.221
50.25	51.14	31.68	330.35	0.05621	0.225
50.25	51.16	31.65	345.34	0.05387	0.22
50.28	51.16	31.66	331.37	0.05619	0.222
50.32	51.21	31.62	335.52	0.05573	0.222
50.33	51.25	31.67	347.38	0.05373	0.22
50.35	51.28	31.61	341.93	0.05482	0.226
50.42	51.3	31.59	331.88	0.05674	0.222
50.49	51.4	31.64	335.93	0.05611	0.226
50.59	51.5	31.81	334.19	0.05619	0.228
50.63	51.55	31.66	342.54	0.05538	0.225
60.18	61.15	31.4	400	0.07195	0.203
60.24	61.24	31.45	412.35	0.06982	0.203
60.32	61.35	31.43	413.74	0.06983	0.208
60.37	61.4	31.44	413.54	0.06996	0.208
60.43	61.4	31.42	400.86	0.07237	0.202
60.55	61.55	31.46	415.05	0.07009	0.201

Table 28 (cont.)

$T_{in}(^{\circ}C)$	$T_{out}(^{\circ}C)$	$T_{am}(^{\circ}C)$	$G_B(\mathrm{W/m^2})$	$(T_{in}-T_{am})/\mathrm{G_B}$	η
60.56	61.55	31.43	413.63	0.07043	0.2
60.65	61.62	31.4	415.22	0.07044	0.195
60.65	61.59	31.47	390.57	0.07471	0.201
60.67	61.68	31.57	414.26	0.07025	0.203
60.68	61.7	31.58	418.64	0.06951	0.204
60.78	61.78	31.57	410.05	0.07124	0.204
60.79	61.79	31.41	419.16	0.0701	0.199
60.8	61.83	31.49	413.18	0.07094	0.208
60.86	61.86	31.43	418.79	0.07027	0.2
60.98	61.95	31.45	400.99	0.07365	0.202
70.22	70.83	32.09	324.74	0.11742	0.157
70.35	70.96	31.93	324.68	0.11832	0.158
70.42	71.04	31.91	319.87	0.12039	0.162
70.42	71.05	31.96	328.88	0.11695	0.159
70.43	71.05	31.84	324.12	0.11907	0.16
70.45	71.06	32	325.1	0.11827	0.157
70.52	71.13	31.89	325.58	0.11864	0.157
70.6	71.22	31.83	328.74	0.11794	0.158
70.65	71.27	31.87	327.46	0.11843	0.158
70.66	71.28	31.86	330	0.11758	0.157
70.71	71.33	31.87	325.84	0.1192	0.159
70.72	71.36	32.02	328.95	0.11764	0.163
70.76	71.38	31.89	324.6	0.11973	0.161
70.78	71.39	31.82	320.39	0.1216	0.159
70.79	71.42	32	327.94	0.1183	0.16
70.87	71.5	31.88	324.68	0.12009	0.162

The parameter of annual energy calculation

$T_a = 30$ $T_i = 40$ $T_o = 70$

$G_B = 350$ $E(kWh/m^2) = 1{,}349$

Table 29 The calculation of annual energy

Thickness (μm)	Thermal efficiency equations	$F_R\eta_0$	c_1/C	$c_2 G_B/C$	η_0	Annual energy yield (kWh/m^2)
14.2	$\eta = 0.21 - 0.88x - 0.01x^2$	0.21	0.88	0.01	0.18	245.51
15.2	$\eta = 0.24 - 0.44x - 0.01x^2$	0.24	0.44	0.01	0.22	302.94
18.9	$\eta = 0.25 - 0.42x - 0.01x^2$	0.25	0.42	0.01	0.23	317.20

Publication

Key Engineering Materials Vols. 675-676 (2016) pp 467-472
© (2016) Trans Tech Publications, Switzerland
doi:10.4028/www.scientific.net/KEM.675-676.467

Submitted: 2015-06-02
Revised: 2015-08-05
Accepted: 2015-08-18

Characterization and Spectral Selectivity of Sn-Al_2O_3 Solar Absorber

Titiporn Chorchong[1, a], Tawat Suriwong[1, b,*], Sukruedee Sukchai[1, c] and Thotsaphon Threrujirapapong[2,d]

[1]School of Renewable Energy Technology, Naresuan University, Phitsanulok, 65000, Thailand

[2]Division of Materials Engineering, Faculty of Engineering, Naresuan University, Phitsanulok, 65000, Thailand

[a]titiporn_ant@hotmail.com, [b,*]tawats@nu.ac.th, [c]Sukruedeen@nu.ac.th, [d]thotsaphont@nu.ac.th

Keywords: Tin-pigmented alumina; Characterization; Solar absorber; Anodization; Absorptance

Abstract.

Tin-pigmented alumina (Sn-Al_2O_3) solar absorber on aluminium substrate was successfully prepared by anodic anodization and further characterized by different methods. The phase, morphology and reflectance (R) of the Sn-Al_2O_3 solar absorber were measured by using X-ray Diffraction (XRD), a Scanning Electron Microscope (SEM) equipped with an energy dispersive X-ray (EDX) analyzer and Ultraviolet-visible-near infrared. The solar absorptance (α) was calculated based on the relationship of the spectral reflectance, $R(\lambda)$, and the solar spectral irradiance of AM 1.5, $I_s(\lambda)$, in the wavelength range of 300-2500 nm. The result was a dark-black surface color on the Sn-Al_2O_3 film. The XRD pattern of the Sn-Al_2O_3 film was indexed as aluminium and tin phases. The chemical composition of the Sn-Al_2O_3 film was tin (Sn), aluminum (Al) and oxygen (O) elements. The average thickness of the produced film was 18.9 µm. The Sn-Al_2O_3 film showed low R (0.09) and high α (0.93) values for the whole 300-2500 nm wavelength range, corresponding to the theoretical properties of the solar absorber. Therefore, it can be concluded that the Sn-Al_2O_3 film on aluminium substrate can be applied as a solar absorber in solar collectors due to the high α, which is similar to commercial solar absorbers.

Introduction

Solar radiation is a free resource and is seen as an important alternative energy source. The solar spectrum can be converted to electricity by photovoltaic means or from thermal energy using appropriate solar technologies. Solar spectral selective solar absorbers are a critical component of solar photo-thermal conversion absorbers, which are able to directly convert solar radiation to thermal energy. Solar selective coatings have been widely studied in order to achieve both a high solar absorptance (α) over the whole solar spectral wavelength of 0.3–2.5 µm and low emittance (ε) at the operating temperature or long wavelength radiation of 2.5–20 µm (IR region) [1, 2]. This is realized by the low reflectance (near zero) of the selective solar absorber in the main solar radiation spectrum and the high reflectance (close to one) in the IR region (> 2.5 µm) [2]. Most of the successful solar selective coatings are metal-dielectric composite coatings or cermet coatings due to their excellent optical properties, high photo-thermal conversion and high thermal stability while operating at a medium-high temperatures [3-5]. Metal-pigmented alumina selective coating is one cermet coating which has been considered to be the most attractive solar selective absorber due to its wide variety of technological applications in thermal solar technology. There are various techniques for the preparation of metal-pigmented alumina selective coatings such as sputtering [2, 3, 6-8], electrochemical deposition (anodization) [9], the aqueous solution-chemical method [10] among others [1]. In addition, anodization on aluminium substrate is a common technique with a low production cost and is extensively used in the aluminium industry for making protective coatings. A large number of metal-pigmented alumina selective coatings, such as Mo-Al_2O_3 [3, 6], Ni-Al_2O_3 [9, 10], W-Al_2O_3 [4], Ag-Al_2O_3 [8], Pt-Al_2O_3 [7], and AlNi-Al_2O_3 [2] have been studied and applied as a solar selective absorber. According to the previous literature, various metals can be pigmented into the pores of alumina. However, tin-pigmented alumina (Sn-Al_2O_3) prepared by anodic anodization

have rarely been reported, and the morphology and solar selective absorber properties of this coating are unknown at present.

In the present study, therefore, we attempted to characterize the phase, morphology and chemical composition of Sn-Al_2O_3 solar absorber prepared by anodic anodization. As well, the spectral selectivity of the prepared Sn-Al_2O_3 solar absorber was investigated and compared with those of the metal-pigmented alumina selective coatings discussed in the literature.

Experimental Approach

A rectangular shaped sheet of aluminium (Al) alloy (99.9%) with the dimensions of 9 cm × 39 cm × 0.05 cm was used as the substrate. The Al substrate was degreased with a commercial cleaning solution, rinsed in deionized (DI) water and then etched by NaOH solution. The Al substrate was then immersed in a sulfuric acid solution to neutralize the surface. This was done under ambient temperature conditions. In the anodization process, the fabrication of the alumina (Al_2O_3) film on the aluminium substrate was done using a sulfuric acid solution (165 g/L) with a 1,000 A direct current and the constant potential ranged from 15 to 17 V at 20±1°C. The anodization time was determined according to the thickness of the Al_2O_3 film to be achieved. In the process of anodic oxidation, the aluminium substrate is the anode (+) electrode, and a lead plate is the cathode (-) electrode. Under suitable conditions, the Al_2O_3 film was formed as a translucent coating on the surface of the Al substrate. The sample was then rinsed in DI water for 10 s. Subsequently, the tin pigmentation of the alumina (Sn-Al_2O_3) was carried out by electrochemical deposition in a coloring tank containing a commercial tin (II) sulfate ($SnSO_4$) solution and buffered to a less acidic state in DI water at 20±1°C. The pigmented Sn content in the pores of the Al_2O_3 film was achieved by various process parameters corresponding to the active surface area of the sample such as voltage and time in the coloring tank. The sample was then rinsed and the porous Al_2O_3 film was sealed with a sealing solution in a hot water tank at 50°C-60°C for 1800 s. As a final step, the sample was cooled down and dried at room temperature. The anodization and tin pigmentation processes were carried out at Bangpoo Coating Co., Ltd., Samutprakarn, Thailand.

The Sn-Al_2O_3 sample was characterized by different methods. The phase, morphology and reflectance (R) of the sample were determined by X-ray diffraction (XRD) using a Philips X'Pert PANalytical X-ray diffractometer with Cu-K_α radiation in the 2θ range of 10-100°, a Scanning Electron Microscope (SEM, JSM-5910 JEOL) operating at 12 kV equipped with energy dispersive X-ray (EDX) analyzer and an Ultraviolet-visible-near infrared spectrophotometer (Shimadzu UV-3101PC) in the wavelength interval of 300-2500 nm. The solar absorptance (α) was calculated from the reflectance spectrum by the following equation [11]:

$$\alpha = \frac{\int_{0.3\mu m}^{2.5\mu m} I_s(\lambda)(1-R(\lambda))d\lambda}{\int_{0.3\mu m}^{2.5\mu m} I_s(\lambda)d\lambda} \quad (1)$$

where $R(\lambda)$ is the measured spectral reflectance of the coating at a specific wavelength in the interval 300-2500 nm, and $I_s(\lambda)$ is the solar spectral irradiance at air mass AM 1.5 [12].

Results and Discussion

Fig. 1 shows the XRD pattern of Sn-Al_2O_3 solar absorber deposited on the Al substrate, compared with the JCPDS database of Al, Al_2O_3 and Sn with the reference no. 01-1176, 01-1243 and 01-0926, respectively. In the diffraction pattern, only the diffraction peaks from the Al substrate and Sn pigment were observed, indicating that the X-ray penetrated through the Al_2O_3 film and reached the Sn pigment and Al substrate. However, Al_2O_3 phase was not detected in this sample because the

porous Al_2O_3 film seemed to be fully amorphous phase, which accords with to the previous results for Mo-Al_2O_3 [6], Pt-Al_2O_3 [7] and Ag-Al_2O_3 [8] solar selective coating. Furthermore, the crystallite size of the Sn pigment in the pores of the Al_2O_3 film was calculated using the XRD data and Scherrer's equation [13].

$$D = \frac{\kappa\lambda}{\beta\cos\theta} \tag{2}$$

κ is the shape factor which usually takes a value of 0.9 (spherical crystallites), λ is the wavelength of Cu-Kα radiation (0.15406 nm), and β and θ are the full width at half maximum (FWHM) and Bragg's angle of the (200) peak of Sn, respectively. The calculated crystallite size of the Sn pigment in the sample was 22.7 nm.

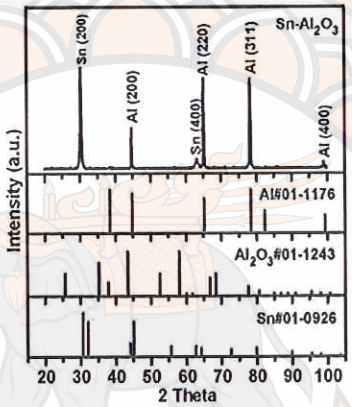

Fig. 1. XRD pattern of Sn-Al_2O_3 solar absorber, comparing to the diffraction lines of the reference: Al (red), Al_2O_3 (blue) and Sn (green).

Fig. 2 presents the SEM images of the Sn-Al_2O_3 solar absorber prepared by the anodic anodization process. The surface morphology of the Sn-Al_2O_3 solar absorber was relatively smooth with a dense surface over the entire sample (Fig. 2(a)). As can be observed in Fig. 2(b), the Al_2O_3 film was formed on the Al substrate with an average thickness of ~18.9 μm. In addition, the porous Al_2O_3 layer had high adhesion contact with the compact Al_2O_3 barrier and Al substrate, corresponding with the Ni-AlO_3 selective absorber previously described [9, 14]. The characterization of the cross-sectional morphology of the Sn-Al_2O_3 solar absorber (Fig. 2(b)) shows that the porous Al_2O_3 film presents two different contrast regions with strong compositional contrast in the sample surface due to the atomic numbers of the different phases. The light gray region corresponded to the Sn pigment rich area while the dark gray region corresponded to the Al_2O_3 phase. The Sn pigment rich area presents as a high contrast region near the Al substrate interface. This is due to the pores of the Al_2O_3 being filled with Sn pigment during the electrochemical deposition process.

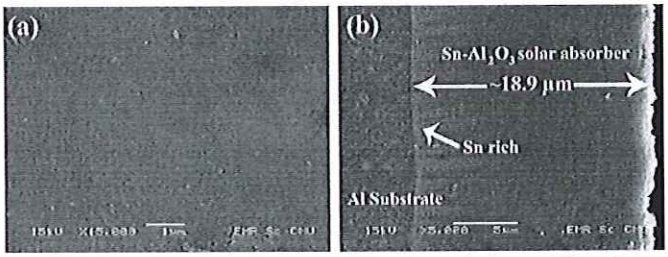

Fig. 2. SEM images of (a) surface and (b) cross-sectional morphology of Sn-Al_2O_3 solar absorber.

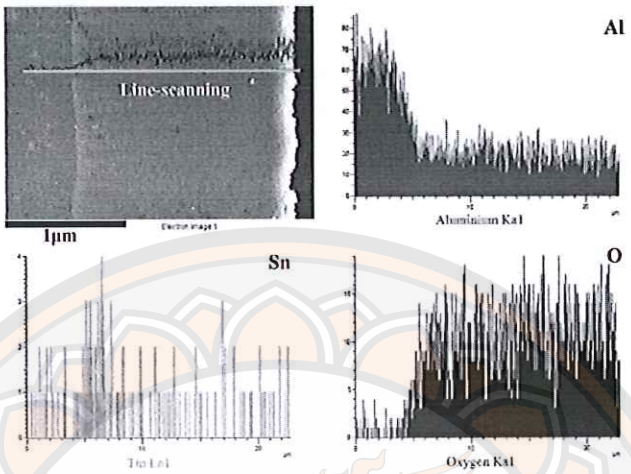

Fig. 3. SEM-EDX line scanning profiles of cross-sectional Sn-Al_2O_3 solar absorber.

In order to confirm the existence of the Sn pigment in the porous Al_2O_3 film, it was characterized by SEM-EDX with line scan analysis technique. In this technique the primary electron beam is focused and scanned in a line across the region of interest on the surface of the Sn-Al_2O_3 solar absorber. The energy characteristics and number of emitted X-rays of the parent elements in the scan line were detected and recorded by the EDX analyzer in the form of the count rate for each element (Al, O and Sn). Fig. 3 shows the elemental distribution profiles in the cross-section of the surface of the Sn-Al_2O_3 solar absorber . It is obvious that the Sn-Al_2O_3 solar absorber consists of Sn, Al and O, as well as the main chemical compositions; Al and O, in the Al_2O_3 film. This result is in good agreement with the XRD pattern of the Sn-Al_2O_3 film. Furthermore, the Sn elements showed a high count rate at the surface adjacent to the Al substrate indicating that the Sn pigments have a high concentration at the near interface of the Al substrate, corresponding to the Sn pigments that were deposited in the pores of the Al_2O_3 film by electrolysis. These results also correspond with the light gray region represented as Sn pigment rich area in Fig. 2.

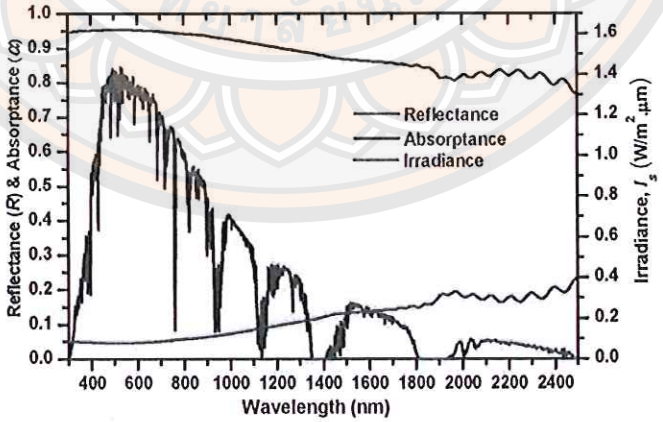

Fig. 4. Spectral reflectance (R) and solar absorptance (α) curves of Sn-Al_2O_3 solar absorber, comparing with the sun spectrum at AM 1.5 in the wavelength range of 300-2500 nm.

Fig. 4 presents the measured reflectance (R) and calculated solar absorptance (α) spectra of Sn-Al_2O_3 solar absorber, together with the sun spectrum at AM 1.5 in the wavelength range of 300-2500 nm. It can be observed that the R of the sample is slightly increased with the increasing wavelength. Additionally, the R was relatively low in the UV-Visible spectrum region (300-800 nm) while R was rather high in the near infrared region. This can be explained by the Al_2O_3 layer without the Sn pigments (top layer) reducing the reflection (anti-reflecting layer) between the air and the Sn-pigmented Al_2O_3 layer (solar absorbing layer) [1, 7]. The α of the Sn-Al_2O_3 solar absorber gradually decreased with the increasing wavelength. Over the whole wavelength interval of the solar spectrum, the R and α of the Sn-Al_2O_3 solar absorber were 0.09 and 0.93, respectively. It seems that the spectral selectivity of the Sn-Al_2O_3 solar absorber mainly depends on the intrinsic absorption of the Sn pigments and the Al_2O_3 layer without the Sn pigments plays the role of anti-reflection. These results are in good agreement with a theoretical selective solar absorber for photo-thermal conversion absorber. In addition, the R and α of the Sn-Al_2O_3 solar absorber were close to those of the related metal-Al_2O_3 solar absorbers such as Mo-Al_2O_3, Ni-Al_2O_3, W-Al_2O_3, Ag-Al_2O_3, Pt-Al_2O_3, and AlNi-Al_2O_3 solar absorbers [1-3, 6, 7, 9, 10], including the commercial solar selective absorber for solar-thermal energy conversion applications [1]. It is, therefore, concluded that the Sn-Al_2O_3 solar absorber prepared by the anodic anodization process is a good candidate for being a solar selective absorber in the field of solar photo-thermal conversion applications.

Summary

The Sn-pigmented Al_2O_3 solar absorber on the aluminium substrate was successfully prepared by anodic anodization. The surface color of the Sn-Al_2O_3 film was dark-black color. The XRD pattern of the Sn-Al_2O_3 film was indexed as aluminium and tin phases while Al_2O_3 phase was not detected in this sample because the porous Al_2O_3 film was a fully amorphous phase. The surface morphology of the Sn-Al_2O_3 solar absorber was relatively smooth and the surface was dense over the entire sample. The Al_2O_3 film was formed on the Al substrate with an average thickness of ~18.9 μm. In addition, the Sn pigments were present in high concentration at the area close to the Al substrate in the pores of the Al_2O_3 film, as shown by its pigmentation. The Sn-pigmented Al_2O_3 solar absorber exhibited very low reflectance (R) of ~ 0.09 and hence high solar absorptance (α) of ~ 0.93 in the whole solar spectral wavelength interval (300-2500 nm). The spectral selectivity of the Sn-Al_2O_3 solar absorber mainly depends on the intrinsic absorption of the Sn pigments. The Al_2O_3 layer without the Sn pigments plays the role of anti-reflection. According to the results, the Sn-pigmented Al_2O_3 solar absorbers are attractive candidates for use in solar photo-thermal conversion applications because of their excellent spectral selectivity.

Acknowledgements

We are grateful to the National Research Council of Thailand (NRCT), and Naresuan University, Thailand for providing financial support (Grant no. R2557B042), including the Graduate School of Naresuan University, Thailand for general funding. Many thanks to Mr. Roy Morien of the Naresuan University Language Centre for his editing assistance and advice on English expression in this document.

References

[1] C.E. Kennedy, Review of Mid- to High-Temperature Solar Selective Absorber Materials National Renewable Energy Laboratory (NREL), (2002) 1-52.

[2] Y. Xue, C. Wang, W. Wang, Y. Liu, Y. Wu, Y. Ning, Y. Sun, Spectral properties and thermal stability of solar selective absorbing AlNi–Al_2O_3 cermet coating, Sol. Energy, 96 (2013) 113-118.

[3] V. Teixeira, E. Sousa, M.F. Costa, C. Nunes, L. Rosa, M.J. Carvalho, M. Collares-Pereira, E. Roman, J. Gago, Spectrally selective composite coatings of Cr–Cr_2O_3 and Mo–Al_2O_3 for solar energy applications, Thin Solid Films, 392 (2001) 320-326.

[4] A. Antonaia, A. Castaldo, M.L. Addonizio, S. Esposito, Stability of W-Al_2O_3 cermet based solar coating for receiver tube operating at high temperature, Sol. Energy Mater. Sol. Cells, 94 (2010) 1604-1611.
[5] D. Ding, W. Cai, M. Long, H. Wu, Y. Wu, Optical, structural and thermal characteristics of Cu–$CuAl_2O_4$ hybrids deposited in anodic aluminum oxide as selective solar absorber, Sol. Energy Mater. Sol. Cells, 94 (2010) 1578-1581.
[6] D. Xinkang, W. Cong, W. Tianmin, Z. Long, C. Buliang, R. Ning, Microstructure and spectral selectivity of Mo–Al_2O_3 solar selective absorbing coatings after annealing, Thin Solid Films, 516 (2008) 3971-3977.
[7] Z.Y. Nuru, C.J. Arendse, R. Nemutudi, O. Nemraoui, M. Maaza, Pt–Al_2O_3 nanocoatings for high temperature concentrated solar thermal power applications, Physica B: Condensed Matter, 407 (2012) 1634-1637.
[8] H.C. Barshilia, P. Kumar, K.S. Rajam, A. Biswas, Structure and optical properties of Ag–Al_2O_3 nanocermet solar selective coatings prepared using unbalanced magnetron sputtering, Sol. Energy Mater. Sol. Cells, 95 (2011) 1707-1715.
[9] A. Wazwaz, J. Salmi, R. Bes, The effects of nickel-pigmented aluminium oxide selective coating over aluminium alloy on the optical properties and thermal efficiency of the selective absorber prepared by alternate and reverse periodic plating technique, Energy Convers. Manage., 51 (2010) 1679-1683.
[10] Z. Li, J. Zhao, L. Ren, Aqueous solution-chemical derived Ni–Al_2O_3 solar selective absorbing coatings, Sol. Energy Mater. Sol. Cells, 105 (2012) 90-95.
[11] G. Katumba, L. Olumekor, A. Forbes, G. Makiwa, B. Mwakikunga, J. Lu, E. Wäckelgård, Optical, thermal and structural characteristics of carbon nanoparticles embedded in ZnO and NiO as selective solar absorbers, Sol. Energy Mater. Sol. Cells, 92 (2008) 1285-1292.
[12] C.A. Gueymard, The sun's total and spectral irradiance for solar energy applications and solar radiation models, Sol. Energy, 76 (2004) 423-453.
[13] T. Suriwong, S. Thongtem, T. Thongtem, Solid-state synthesis of cubic ZnTe nanocrystals using a microwave plasma, Mater. Lett., 63 (2009) 2103-2106.
[14] Å. Andersson, O. Hunderi, C.G. Granqvist, Nickel pigmented anodic aluminum oxide for selective absorption of solar energy, J. Appl. Phys., 51 (1980) 754-764.